



## PALADYN v1.0, a comprehensive land surface-vegetation-carbon cycle model of intermediate complexity

Matteo Willeit and Andrey Ganopolski

Potsdam Institute for Climate Impact Research (PIK), Potsdam, Germany

*Correspondence to:* Matteo Willeit (willeit@pik-potsdam.de)

**Abstract.** PALADYN is presented, a new comprehensive and computationally efficient land surface–vegetation–carbon cycle model designed to be used in Earth system models of intermediate complexity for long-term simulations and paleoclimate studies.

The model treats in a consistent manner the interaction between atmosphere, terrestrial vegetation  
5 and soil through the fluxes of energy, water and carbon. Energy, water and carbon are conserved.  
The model explicitly treats permafrost, both in physical processes and as important carbon pool.  
The model distinguishes 9 surface types of which 5 are different vegetation types, bare soil, land  
ice, lake and ocean shelf. Including the ocean shelf allows to treat continuous changes in sea level  
and shelf area associated with glacial cycles. Over each surface type the model solves the surface  
10 energy balance and computes the fluxes of sensible, latent and ground heat and upward shortwave  
and longwave radiation. It includes a single snow layer.

Vegetation and bare soil share a single soil column. The soil is vertically discretized into 5 layers  
where prognostic equations for temperature, water and carbon are consistently solved. Phase changes  
of water in the soil are explicitly considered. A surface hydrology module computes precipitation  
15 interception by vegetation, surface runoff and soil infiltration. The soil water equation is based on  
Darcy's law. Given soil water content, the wetland fraction is computed based on a topographic  
index. The temperature profile is also computed in the upper part of ice sheets and in the ocean shelf  
soil.

Photosynthesis is computed using a light use efficiency model. Carbon assimilation by vegetation  
20 is coupled to the transpiration of water through stomatal conductance. The model includes a dynamic  
vegetation module with 5 plant functional types competing for the gridcell share with their respective  
net primary productivity.



The model distinguishes between mineral soil carbon, peat carbon, buried carbon and shelf carbon. Each soil carbon 'type' has its own soil carbon pools generally represented by a litter, a fast and a  
25 slow carbon pool in each soil layer. Carbon can be redistributed between the layers by vertical diffusion. For the vegetated macro surface type, decomposition is a function of soil temperature and soil moisture. Carbon in permanently frozen layers is assigned a long turnover time which effectively locks carbon in permafrost. Carbon buried below ice sheets and on flooded ocean shelves is treated differently. The model also includes a dynamic peat module.

30 PALADYN includes carbon isotopes  $^{13}\text{C}$  and  $^{14}\text{C}$ , which are tracked through all carbon pools. Isotopic discrimination is modelled only during photosynthesis.

A simple methane module is implemented to represent methane emissions from anaerobic carbon decomposition in wetlands (including peatlands) and flooded ocean shelf.

The model description is accompanied by a thorough model evaluation in offline mode for the  
35 present day and the historical period.

## 1 Introduction

Land surface models (LSMs) represent an essential component of Earth system models of different complexity. Currently LSMs simulate the interaction between atmosphere, vegetation, land surface and upper soil through the fluxes of energy, water and carbon. Modern LSMs are the result of a  
40 gradual convergence of initially separate modeling approaches: climate, carbon cycle and vegetation dynamics models (e.g. Pitman, 2003; Sellers et al., 1997).

In the earlier climate models very simple land surface schemes with bucket hydrology and without explicit vegetation representation were used (Manabe, 1969). The 2nd generation LSMs (Sellers et al., 1997) simulated soil temperature and moisture in several layers and the water and energy  
45 exchange between the land surface and the atmosphere were mediated by vegetation represented as a big leaf (e.g. Deardorff, 1978), BATS (Dickinson et al., 1986) and SiB (Sellers et al., 1986)). This step was required because biological processes play a major role in controlling evapotranspiration. In 2nd generation LSMs the behaviour of leaf stomata, which controls the rate of transpiration of water from plants, was represented based on empirical relations with climate (e.g. Jarvis, 1976).  
50 The 3rd generation of LSMs included additionally a mechanistic representation of photosynthesis (Farquhar et al.; Collatz et al., 1991) which could then directly be related to stomatal conductance used to compute transpiration (Ball et al., 1987; Leuning, 1995).

Terrestrial biogeochemical models followed a separate line of development. These models were designed to simulate the exchanges of carbon between the atmosphere and terrestrial ecosystems for  
55 a given climate and geographic vegetation distribution (e.g. Raich et al., 1991; Melillo et al., 1993; Running and Coughlan, 1988; Running and Gower, 1991; Foley, 1994).



Equilibrium biogeography models were developed alongside terrestrial carbon cycle models to simulate the global vegetation distribution for given climatic conditions (Woodward, 1987; Prentice et al., 1992; Haxeltine and Prentice, 1996b; Neilson, 1995). However, equilibrium models do not  
60 simulate the processes of plant growth, competition and mortality that govern the dynamics of vegetation changes. Global dynamic vegetation models have been developed for this purpose (Haxeltine and Prentice, 1996b; Sitch et al., 2003; Cox, 2001; Friend et al., 1997; Foley et al., 1996; Woodward et al., 1998; Brovkin et al., 1997).

Since it was shown that climate-vegetation feedbacks may be important, the first attempts to incorporate interactive vegetation into climate models were made (Henderson-Sellers, 1993; Claussen, 1994). While during the 1990s and 2000s climate models and then Earth system models (ESMs) based on coupled general circulation models (GCMs) remained too expensive to perform long-term simulations, a new class of models - Earth system models of intermediate complexity (EMICS, Claussen et al. (2002)) - emerged. The EMIC CLIMBER-2 (Petoukhov et al., 2000; Ganopolski  
70 et al., 2001) was one of the first Earth system models which included both terrestrial carbon cycle and vegetation dynamics based on VECODE (Brovkin et al., 1997, 2002) and has been also used to estimate the strength of the climate-vegetation feedback (Willeit et al., 2014b) and the carbon cycle feedback (Willeit et al., 2014a). Later, similar and more comprehensive vegetation models were incorporated in both complex and intermediate complexity ESMs (e.g. Cox, 2001; Oleson et al., 2004;  
75 Krinner et al., 2005; Sato et al., 2007; Reick et al., 2013).

A limitation of previous land surface modeling approaches is that different model components are not necessarily consistent because initially they were developed as stand-alone models. Additionally, initially LSMs have been developed with the intention to capture the processes which are important for climate change projections on the time scales of centuries, thus missing processes which might  
80 play an important role on longer time scales. This was fully justified by the fact that complex ESMs were and are still too computationally expensive to be used on much longer time scales, such as for simulations of glacial cycles. Only recently some existing models have been adapted to include slower processes, for example peat carbon dynamics (Wania et al., 2009; Kleinen et al., 2012; Spahni et al., 2013; Stocker et al., 2014). However, the simulation of processes with long time scales, such  
85 as peat carbon accumulation or inert permafrost carbon dynamics, require necessarily a transient modelling approach, which is made feasible only by a fast model.

Here we present a new land surface model primarily designed for paleoclimate applications, and therefore named PAleo LAnd DYnamics model (PALADYN), although also applicable to many other types of studies, including multi-ensemble future projections. The model has been designed  
90 to represent the land processes which are thought to be important both on short and very long time scales. The physical and biochemical processes are consistently coupled with each other. The model is intended to be used in the next generation of the CLIMBER EMIC and to substitute VECODE. CLIMBER employs a statistical dynamical atmosphere model. This type of model does not explicitly



simulate weather and therefore PALADYN is designed to simulate climatological mean seasonal  
95 cycle. Typical application of such model is simulations of Earth system dynamics on astronomical  
and geological time scales. This is why particular attention is given to the selection of the proper  
complexity of the different processes which are represented in order to capture the main feedbacks  
in the system but at the same time maintain the model computationally efficient. We expect that  
PALADYN can also be used in other EMICs since most of them still employ rather simplistic LSMs.

## 100 2 Model overview

PALADYN is designed to operate on coarse resolution required for long-term simulations. Here we  
test the model on a  $5 \times 5^\circ$  horizontal resolution.

In each grid cell the model distinguishes 9 surface types (5 vegetation types, bare soil, ice sheets,  
lakes and ocean shelf) (Fig. 1a). All surface type fractions can change over time. The fraction of  
105 vegetation types and bare soil is computed by the dynamic vegetation module. The model is also able  
to handle changes in the fraction of ice sheet and ocean shelf, when given as input. This is necessary  
to simulate glacial cycles. So far lakes are implemented in the model only as a placeholder.

Over each surface type, except ocean shelf, the model solves the surface energy balance and com-  
putes the fluxes of sensible, latent and ground heat and upward shortwave and longwave radiation.

110 Vegetation and bare soil share a single soil column (Fig. 1b) where temperature, moisture and  
carbon are discretized in 5 vertical layers reaching down to a depth of 3.9 m. The top soil layer is  
20 cm thick. A single snow layer with prognostic temperature and density is included in the model on  
top of the soil column. A 1d-heat diffusion equation is solved to compute snow and soil temperature  
with the ground heat flux as top boundary condition. Snowmelt and phase changes of water in the soil  
115 are explicitly considered. A surface hydrology module computes rainfall intercepted by vegetation,  
surface runoff and infiltration. Infiltration provides the top boundary condition for the solution of  
soil water equation based on Darcy's law. Given soil water content the wetland fraction is computed  
following a simplified TOPMODEL approach (Niu et al., 2005).

For the ice sheet fraction, the temperature of the snow layer and of the top 3.9 m of ice below is  
120 computed in the same way as for the soil, but phase changes in the ice are inhibited. The temperature  
of the soil below the shelf water is needed to calculate the decomposition rate of shelf carbon. It is  
computed from a 1-d diffusion equation with the shelf water temperature prescribed as top boundary  
condition and assuming that the soil is saturated with liquid and/or frozen water. Phase changes are  
accounted for.

125 Photosynthesis is computed following Sitch et al. (2003); Haxeltine and Prentice (1996a, b). Car-  
bon assimilation by vegetation is coupled to the transpiration of water vapor through stomatal con-  
ductance. PALADYN includes a dynamic vegetation module based on TRIFFID (Cox, 2001) with 5  
plant functional types competing for the gridcell share with their respective net primary production.



PALADYN includes a representation of soil carbon processes, including slow processes that are  
 130 thought to be relevant over multimillennial time scales associated with glacial-interglacial transitions  
 when the appearance and disappearance of continental ice sheets, changes in sea level and land area  
 can potentially strongly affect the land carbon cycle. PALADYN therefore includes processes with  
 a long time scale, such as accumulation of carbon in peatlands, inert carbon locked in perennially  
 frozen ground and carbon buried below ice sheets. It also accounts for changes in land area due to  
 135 sea level variations and isostatic adjustment of the lithosphere to the ice sheet loading. During periods  
 of low sea level the model allows vegetation to grow on exposed ocean shelves. When sea level is  
 rising the exposed shelf becomes flooded and the vegetation dies.

The soil of the vegetated grid cell part, below the ice sheet and below the shelf water has its own  
 carbon pools (Fig. 1c) represented in general by a litter, a fast and a slow carbon pool in each soil  
 140 layer. Carbon can be redistributed between the layers by vertical diffusion. For the vegetated part,  
 decomposition of organic matter is a function of soil temperature and soil moisture. Carbon in per-  
 manently frozen layers is assigned a long turnover time which effectively locks carbon in permafrost.  
 Carbon buried below ice sheets and carbon on the flooded ocean shelf are treated separately.

A representation of peatland dynamics is also included in PALADYN. In inundated areas, peat is  
 145 formed by accumulating carbon at the surface in the seasonally anoxically decomposing acrotelm.  
 When the acrotelm carbon exceeds a critical value, carbon is transferred to the catotelm below the  
 water table.

PALADYN also includes carbon isotopes  $^{13}\text{C}$  and  $^{14}\text{C}$ , which are tracked through all carbon pools.  
 Isotopic discrimination is modelled only during photosynthesis.

150 A simple methane module is implemented to represent methane emissions from anaerobic carbon  
 decomposition in wetlands (including peatlands) and flooded ocean shelf.

The processes represented in PALADYN are illustrated in Fig. 2 and Fig. 3.

All physical model components and photosynthesis are integrated with an implicit timestepping  
 scheme with a time step of one day. Dynamic vegetation and soil carbon processes are integrated  
 155 with an implicit timestepping scheme with a time step of one month.

The model is written in FORTRAN90 and uses the NCIO package (Robinson and Perrette, 2015)  
 to handle input and output of data.

This paper describes the model representation of processes over ice free land. Processes related to  
 changes in land-ice-ocean mask, buried and ocean shelf carbon will be described in a forthcoming  
 160 paper.

### 3 Surface energy balance and fluxes

The surface energy balance equation at the land surface is written as:

$$(1 - \alpha)SW^{\downarrow} + \epsilon LW^{\downarrow} - LW^{\uparrow} - H - LE - G = 0, \quad (1)$$



where  $\alpha$  is surface albedo,  $SW^\downarrow$  is the incoming shortwave radiation,  $\epsilon$  is the surface emissivity  
 165 for longwave radiation,  $LW^\downarrow$  and  $LW^\uparrow$  are the incoming and outgoing longwave radiation at the  
 surface,  $H$  is the sensible heat flux,  $LE$  is the latent heat flux and  $G$  the ground heat flux. Equation (1)  
 is then solved for the skin temperature,  $T_*$ , using the formulations for the energy fluxes described  
 next. All symbols are defined in Table 1.

The surface emitted longwave radiation is given by the Stefan-Boltzmann law with a surface type  
 170 dependent emissivity  $\epsilon$  to account for the fact that the surface is not a perfect black body:

$$LW^\uparrow = \epsilon \sigma T_*^4. \quad (2)$$

The sensible heat flux is computed from the temperature gradient between the surface and a refer-  
 ence height above the surface and an aerodynamic resistance,  $r_a$  (section 3.3), using the bulk  
 aerodynamic formula:

$$175 \quad H = \frac{\rho_a C_p}{r_a} (T_* - T_a), \quad (3)$$

where  $\rho_a$  is air density,  $C_p$  is the specific heat of air,  $r_a$  is the aerodynamic resistance and  $T_a$  is the  
 temperature of the air at a reference level  $z_{\text{ref}}$ .

Similarly, the latent heat flux over unvegetated surfaces is expressed in terms of the specific hu-  
 midity gradient between the surface and a reference atmospheric level with the addition of a factor  
 180  $\beta_s$  (section 3.4) representing a possible limitation in the moisture supply:

$$LE = L \frac{\rho_a}{r_a} \beta_s (q_{\text{sat}}(T_*) - q_a). \quad (4)$$

$L$  is the latent heat of vaporisation,  $q_{\text{sat}}$  is the specific humidity at saturation and  $q_a$  is the specific  
 humidity of air. Over vegetation the latent heat flux consists of contributions from transpiration of  
 water vapour through leaf stomata during photosynthesis, soil/snow evaporation and sublimation  
 185 from below the canopy and evaporation of rainfall intercepted by the canopy:

$$LE = L \frac{\rho_a}{r_a + r_s} (q_{\text{sat}}(T_*) - q_a) + L \frac{\rho_a}{r_a + r_{a,\text{can}}} \beta_s (q_{\text{sat}}(T_{s,1}) - q_a) + LE_{\text{can}}. \quad (5)$$

$r_{a,\text{can}}$  is the aerodynamic resistance between the soil surface and the vegetation canopy (section 3.3)  
 and  $r_s$  is the canopy resistance to water vapor flux through the leaf stomata as described in detail  
 in section 3.4).  $T_{s,1}$  is the temperature of the top soil layer, or the snow layer temperature if snow  
 190 is present. Canopy evaporation and sublimation,  $E_{\text{can}}$ , is computed using the skin temperature from  
 the previous time step as described in section 5.1.

The ground heat flux is represented by conduction of heat between the skin and the center of the  
 snow layer or top soil layer:

$$G = 2\lambda_{s,1} \frac{T_* - T_{s,1}}{\Delta z_1}. \quad (6)$$

195  $\lambda_{s,1}$  is the heat conductivity and  $\Delta z_1$  is the thickness of the snow layer or top soil layer.



The prognostic terms in  $T_*$  in the formulation of the surface energy fluxes are then linearized using Taylor series expansion assuming that the temperature at the new time step,  $T_{*,n+1} = T_{*,n} + \Delta T$  with  $\Delta T_* \ll T_*$ :

$$T_{*,n+1}^4 = T_{*,n}^4 + 4T_{*,n}^3(T_{*,n+1} - T_{*,n}), \quad (7)$$

200

$$q_{\text{sat}}(T_{*,n+1}) = q_{\text{sat}}(T_*) + \left. \frac{dq_{\text{sat}}}{dT_*} \right|_{T_*=T_{*,n}} (T_{*,n+1} - T_{*,n}). \quad (8)$$

Equation (1) can then be solved explicitly for the skin temperature at the new time step,  $T_{*,n+1}$ , separately for each surface type.

If snow is present and the skin temperature is above freezing the surface energy fluxes are diagnosed first with the skin temperature greater than  $0^\circ\text{C}$  and then with skin temperature set to  $0^\circ\text{C}$ . The difference between the sum of the energy fluxes is then used to melt part of the snow layer.

Given the new skin temperatures, the ground heat flux  $G$  and its derivative with respect to top soil or snow temperature ( $\partial G / \partial T_{s,1}$ ) are diagnosed and used as input for the 1d soil heat diffusion equation. After the top-soil/snow temperature has been updated as described in section 4, it is used to compute the total ground heat flux  $G_{\text{new}} = G + \partial G / \partial T_{s,1} \Delta T_{s,1}$ . Skin temperature is then updated using  $G_{\text{new}}$  and all remaining surface energy and water fluxes are diagnosed.

In the next sections the surface parameters needed for the solution of the surface energy balance equation are described.

### 3.1 Surface albedo

PALADYN distinguishes between direct and diffuse albedo in the visible and infrared spectral bands. For ice sheets and bare soil the surface albedo is computed as a weighted mean of snowfree ( $\alpha_{\text{snfree}}$ ) and snow ( $\alpha_{\text{sn}}$ ) albedoes:

$$\alpha = f_{\text{sn}} \alpha_{\text{sn}} + (1 - f_{\text{sn}}) \alpha_{\text{snfree}}, \quad \text{bare soil, ice sheets.} \quad (9)$$

The soil albedo in the visible and near infrared band are prescribed from (Dazlich and Los, 2009). The fraction considered to be snow covered depends on snow height ( $h_{\text{sn}}$ ) and snowfree roughness length ( $z_0^{\text{snfree}}$ ) of the surface (Section 3.3) following Oleson et al. (2004):

$$f_{\text{sn}} = \frac{h_{\text{sn}}}{h_{\text{sn}} + 10z_0^{\text{snfree}}}. \quad (10)$$

The albedo of grass and shrubs is computed by additionally separating the snowfree albedo into bare soil and canopy albedo through a sky view factor  $f_{\text{sv}}$ :

$$\alpha = f_{\text{sn}} \alpha_{\text{sn}} + (1 - f_{\text{sn}})(1 - f_{\text{sv}}) \alpha_{\text{snfree}}^{\text{can}} + (1 - f_{\text{sn}}) f_{\text{sv}} \alpha_{\text{soil}}, \quad \text{grass, shrubs.} \quad (11)$$



The sky view factor is a function of the leaf area index ( $L_{ai}$ ), the stem area index ( $S_{ai}$ ) and an extinction coefficient  $k_{ext}$  (Table 2) (e.g. Otto et al., 2011):

$$f_{sv} = \exp[-k_{ext}(L_{ai} + S_{ai})]. \quad (12)$$

The forest albedo is computed as a weighted mean of canopy albedo ( $\alpha_{can}$ ) and albedo of the  
 230 ground below the canopy ( $\alpha_g$ ):

$$\alpha = f_{sv}\alpha_g + (1 - f_{sv})\alpha_{can}, \quad \text{forest.} \quad (13)$$

The direct beam sky view factor for forest includes a daily radiation weighed solar zenith angle ( $\mu$ ) dependence following Campbell and Norman (1989):

$$f_{sv}^{dir} = \exp\left[-k_{ext} \frac{(L_{ai} + S_{ai})}{\cos\mu}\right]. \quad (14)$$

235 The sky view factor for diffuse radiation is derived by fitting the relation given by Versegly et al. (1993) and is taken to be:

$$f_{sv}^{dif} = \exp\left[-k_{ext} \frac{(L_{ai} + S_{ai})}{\cos 45^\circ}\right]. \quad (15)$$

The albedo of the ground below the canopy,  $\alpha_g$ , is computed as in Eq. (9).  $\alpha_{can}$  varies between snowfree canopy albedo and snow-covered canopy albedo depending on the canopy fraction covered  
 240 by snow:

$$\alpha_{can} = f_{sn}^{can}\alpha_{sn}^{can} + (1 - f_{sn}^{can})\alpha_{snfree}^{can}. \quad (16)$$

The canopy fraction covered by snow,  $f_{sn}^{can}$ , is described in Section 5.1. For  $\alpha_{snfree}^{can}$  the PFT specific values derived from MODIS data in Houldcroft et al. (2009) for the TRIFFID PFTs are used and  $\alpha_{sn}^{can}$  values are taken from Moody et al. (2007) based on MODIS data (Table 5).

245 Snow albedo is parameterized as a function of the solar zenith angle and a snow ageing factor. The diffuse albedo of freshly fallen snow is set to 0.95 in the visible band and to 0.65 in the near infrared band. The actual albedo of snow for diffuse radiation depends on a snow age factor  $f_{age}$ :

$$\alpha_{sn}^{vis,dif} = \alpha_{sn,fresh}^{vis,dif} - 0.05f_{age}, \quad (17)$$

$$\alpha_{sn}^{nir,dif} = \alpha_{sn,fresh}^{nir,dif} - 0.25f_{age}. \quad (18)$$

250 The snow age factor is intended to represent the effect of snow grain size increase on albedo (Warren and Wiscombe, 1980). For simplicity and to account for the fact that a statistical dynamical atmosphere does not resolve single snowfall events but rather returns a smoothly varying daily snowfall rate,  $f_{age}$  is parameterized as a function of skin temperature and snowfall rate as described in Appendix A. If the skin temperature is at melting point, the snow albedo is further reduced by 0.2 to  
 255 account for the formation of melt ponds.





The direct beam snow albedo is then computed as (Dickinson et al., 1986):

$$\alpha_{\text{sn}}^{\text{dir}} = \alpha_{\text{sn}}^{\text{dif}} + 0.4f_{\mu}(1 - \alpha_{\text{sn}}^{\text{dif}}), \quad (19)$$

where the solar zenith angle factor is slightly modified from Dickinson et al. (1986) to correct for the bias highlighted by Gardner and Sharp (2010):

$$260 \quad f_{\mu} = 0.5 \left( \frac{3}{1 + 2\cos\mu} - 1 \right). \quad (20)$$

### 3.2 Surface emissivity

The broadband emissivity ( $\epsilon$ ) used to compute the net longwave radiation at the surface is a surface-type dependent parameter. It is taken to be equal to 0.96 for all vegetation types, 0.9 for bare soil, 0.99 for snow-covered ground and 0.99 for ice (Jin and Liang, 2006; Walters et al., 2014).

### 265 3.3 Aerodynamic resistances

The aerodynamic resistance,  $r_a$ , is computed for each surface type accounting for atmospheric stability through a bulk Richardson number following BATS (Dickinson et al., 1986). The drag coefficients for neutral stratification are obtained from boundary-layer theory:

$$C_{\text{DN}}^{\text{m}} = \left[ \kappa \ln \left( \frac{z_{\text{ref}} - d}{z_{\text{m}}} \right) \right]^2, \quad \text{drag coefficient for momentum} \quad (21)$$

$$270 \quad C_{\text{DN}}^{\text{h}} = \kappa^2 \ln \left( \frac{z_{\text{ref}} - d}{z_{\text{m}}} \right) \ln \left( \frac{z_{\text{ref}} - d}{z_{\text{h}}} \right), \quad \text{drag coefficient for heat and water.} \quad (22)$$

$z_{\text{ref}}$  is a reference height above the surface and  $d$  is the zero-plane displacement, the height above the ground at which zero wind speed is achieved, and depends on the surface type.  $z_{\text{m}}$  is the roughness length for momentum and is computed as the weighted mean of the roughness length of snow ( $z_0^{\text{sn}}$ ) and the roughness length of the snow-free surface ( $z_0^{\text{snfree}}$ ):

$$275 \quad z_{\text{m}} = f_{\text{sn}} z_0^{\text{sn}} + (1 - f_{\text{sn}}) z_0^{\text{snfree}}. \quad (23)$$

A logarithmic averaging would be more appropriate here (Zeng and Wang, 2007), but for computational efficiency a simple linear weighting is preferred. This simplification does not significantly affect the model results. The snow covered fraction is given by Eq. (10) for all surface types. For vegetated surfaces,  $z_0^{\text{snfree}}$  is given by a weighted mean of vegetation ( $z_0^{\text{v}}$ ) and bare soil ( $z_0^{\text{b}}$ ) rough-

280 ness:

$$z_0^{\text{snfree}} = V z_0^{\text{v}} + (1 - V) z_0^{\text{b}}. \quad (24)$$

where the weight  $V$  depends on the vegetation state:

$$V = \frac{L_{\text{ai}} + S_{\text{ai}}}{(L_{\text{ai}} + S_{\text{ai}})_{\text{crit}}}, \quad (25)$$



and is limited to be lower than 1. The critical value of  $(L_{ai} + S_{ai})_{crit}$  is set to 2. Zeng and Wang  
 285 (2007) showed that model results are not very sensitive to the formulation of  $V$ .  $z_0^v$  is taken as 1/10  
 of the vegetation height and the displacement  $d = 0.7Vh_v$ . Vegetation height  $h_v$  varies over time for  
 each PFT and differs between PFTs. For bare soil, snow and ice  $d = 0$  and the values of  $z_0$  are given  
 in Table 2.

In general the roughness length for heat and water vapor differs from the roughness length for  
 290 momentum and is defined by (Garratt, 1994; Milly and Shmakin, 2002):

$$\ln\left(\frac{z_m}{z_h}\right) = 2. \quad (26)$$

$z_h$  is therefore almost an order of magnitude smaller than  $z_m$ .

Although the surface energy balance equation in PALADYN is solved with a daily time step,  
 which implies that the diurnal cycle in atmospheric stability can not be resolved by the model,  
 295 the inclusion of a simple Richardson number dependence based on daily mean temperatures in the  
 computation of the drag coefficients significantly improves the simulated surface energy fluxes when  
 the stratification is unstable. The bulk Richardson number is calculated as (Dickinson et al., 1986):

$$R_i = gz_{ref} \frac{(1 - T_*/T_a)}{V_a^2 + 1}, \quad (27)$$

where  $g$  is the acceleration due to gravity and  $V_a$  is the wind speed at the reference level  $z_{ref}$ . The  
 300 drag coefficients for the unstable case ( $R_i < 0$ ) are then adjusted to account for atmospheric stability:

$$C_D^{m/h} = C_{DN}^{m/h} \left(1 + 24.5\sqrt{-C_{DN}^{m/h} R_i}\right) \quad R_i < 0. \quad (28)$$

Finally, the aerodynamic resistance for sensible and latent heat flux is given by:

$$r_a = \frac{1}{C_D^h V_a} \quad (29)$$

The aerodynamic resistance for the transfer of heat and water between the ground and the canopy  
 305 is parameterized partly following Zeng et al. (2005):

$$r_{a,can} = \frac{1}{C_{can} u_*}. \quad (30)$$

$u_* = V_a C_D^h \sqrt{C_D^h}$  is the friction velocity and represents the wind speed incident on the leaves. The  
 drag coefficient  $C_{can}$  is given by:

$$C_{can} = WC_{bare} + (1 - W)C_{dense}. \quad (31)$$

310 The weight  $W$  depends on the leaf and stem area index,  $W = e^{-(L_{ai} + S_{ai})}$ .  $C_{can}$  varies between  
 $C_{dense}$  for dense canopy and  $C_{bare}$  when  $W$  tends to zero. The values of  $C_{dense}$  and  $C_{bare}$  are given  
 in Table 2.



### 3.4 Surface resistance to water vapor fluxes

Additionally to the aerodynamic resistances, the flux of water vapor from the ground or canopy is  
315 subject to additional resistances. For evaporation from bare soil this surface resistance is represented  
in terms of a  $\beta_s$ -factor. Different parameterisations of  $\beta_s$  have been proposed to be used in global cli-  
mate models (e.g. Mahfouf and Noilhan, 1991). The model, in particular the geographic distribution  
and extent of modelled bare soil, is strongly dependent on the formulation of the  $\beta_s$  factor. Thus var-  
ious surface resistance formulations for bare soil evaporation are implemented in PALADYN with  
320 the default  $\beta_s$  depending on top-soil moisture ( $\theta_1$ ) and field capacity ( $\theta_{fc}$ ) following Lee and Pielke  
(1992):

$$\beta_s = \begin{cases} \frac{1}{4} \left[ 1 - \cos \left( \pi \frac{\theta_1}{\theta_{fc}} \right) \right]^2 & \theta_1 < \theta_{fc} \\ 1 & \theta_1 \geq \theta_{fc}. \end{cases} \quad (32)$$

The resistance for transpiration of water through the leaf stomata is coupled to the uptake of  
carbon during photosynthesis and is simply the inverse of the canopy conductance calculated by the  
325 photosynthesis module (section 6.1) after conversion to units of  $\text{m s}^{-1}$ :

$$r_s = \frac{1}{g_{\text{can}}}. \quad (33)$$

Evaporation and sublimation from the canopy and sublimation from snow and ice are assumed to  
occur without surface resistance ( $r_s = 0$  and  $\beta_s = 1$ ).

## 4 Snow and soil temperature

330 The heat transfer in the snow-soil column is represented by a one-dimensional heat diffusion equa-  
tion:

$$c \frac{\partial T_s}{\partial t} = \frac{\partial}{\partial z} \left[ \lambda \frac{\partial T_s}{\partial z} \right]. \quad (34)$$

Equation 34 assumes that the lateral heat transport and vertical heat transport other than by conduc-  
tion are small and can be neglected. Other models include for example the vertical heat advection by  
335 the water penetrating into the soil (e.g. Cox et al., 1999). Equation 34 also assumes that there are no  
heat sources inside the soil column. Heat generated by organic matter decomposition is an example  
of internally generated heat (e.g. Khvorostyanov et al., 2008). In Eq. 34  $c$  is the volumetric heat  
capacity and  $\lambda$  is the thermal conductivity of soil/snow. Equation 34 is solved with the ground heat  
flux as top boundary condition and zero heat flux at the bottom of the soil column. Eventually the  
340 deep permafrost model of Willeit and Ganopolski (2015) is going to be coupled to PALADYN with  
the geothermal heat flux as bottom boundary condition. The numerical solution of Eq. 34 follows  
the fully implicit formulation in Oleson et al. (2013). The snow/soil temperature profile is calculated  
first without phase change and then readjusted for phase change following Oleson et al. (2013). If



the new temperature of snow or of a soil layer containing frozen water is greater than 0 °C the excess  
 345 energy is used to melt snow or frozen soil water. If all snow is melting during one time step and  
 excess energy is remaining, this energy is added to the top soil layer. If soil temperature drops below  
 0 °C soil water starts to freeze. Observations show that liquid water exists in the soil at temperatures  
 well below 0 °C because of adsorption forces, capillarity and ground heterogeneity (e.g. Williams  
 and Smith, 1989) and the presence of solutes (e.g. Watanabe and Mizoguchi, 2002). To allow liquid  
 350 water to coexist with ice below 0 °C, a freezing point depression is included in the model and the  
 maximum liquid water content for soil temperatures  $T_s$  below  $T_0 = 273.15\text{K}$  is formulated as (e.g.  
 Cox et al., 1999; Niu and Yang, 2006; Ekici et al., 2014):

$$w_w^{\max} = \Delta z \rho_w \theta_{\text{sat}} \left[ \frac{L_f (T_s - T_0)}{g T_s \psi_{\text{sat}}} \right]^{-1/b}, \quad (35)$$

where  $\Delta z$  is the layer thickness,  $\rho_w$  the density of water,  $\theta_{\text{sat}}$  the porosity of the soil,  $L_f$  the  
 355 latent heat of fusion of water,  $\psi_{\text{sat}}$  is the matric potential at saturation and  $b$  the Clapp-Hornberger  
 parameter (Section 5.4).

#### 4.1 Snow and soil thermal properties

Snow plays a crucial role in insulating the ground below from the cold air temperatures. A realistic  
 parameterisation of snow thermal properties is therefore fundamental to simulate frozen soil dynam-  
 ics. In particular, PALADYN is very sensitive to the parameterisation of snow thermal conductivity.  
 360 Hence, several snow thermal conductivity formulations that are all dependent on snow density are  
 included in the model (Yen, 1981; Jordan, 1991; Riche and Schneebeli, 2013). The default snow  
 thermal conductivity is from (Riche and Schneebeli, 2013):

$$\lambda_{\text{sn}} = \lambda_a - 1.06 \times 10^{-5} \rho_{\text{sn}} + 3 \times 10^{-6} \rho_{\text{sn}}^2. \quad (36)$$

365  $\lambda_a$  is the air thermal conductivity and the snow density  $\rho_{\text{sn}}$  is described in detail in Section 5.2.

The volumetric heat capacity of snow depends on snow density and specific heat capacity of ice  
 ( $C_i$ ):

$$c_{\text{sn}} = C_i \rho_{\text{sn}}. \quad (37)$$

Soil heat capacity is a volume weighted mean of dry soil and liquid and frozen water:

$$370 \quad c = (1 - \theta_{\text{sat}}) c_s + \theta_w \rho_w C_w + \theta_i \rho_i C_i, \quad (38)$$

where  $c_s$  is the volumetric heat capacity of dry soil (Table 3),  $\theta_w$  and  $\theta_i$  are the volumetric soil liquid  
 and frozen water contents, respectively,  $C_w$  is the specific heat capacity of water and  $\rho_i$  is the density  
 of ice.

Soil heat conductivity is a combination of heat conductivity of water, ice and dry soil following  
 375 Farouki (1981):

$$\lambda = K \lambda_{\text{sat}} + (1 - K) \lambda_{\text{dry}}, \quad (39)$$



with

$$\lambda_{\text{sat}} = \lambda_s^{1-\theta_{\text{sat}}} \lambda_w^{\frac{\theta_w}{\theta}} \theta_{\text{sat}} \lambda_i^{\frac{\theta_i}{\theta}} \theta_{\text{sat}}, \quad (40)$$

where  $\theta$  is the total (liquid plus frozen) volumetric soil water content. The original logarithmic  
 380 formulation of the Kersten number ( $K$ ) is approximated by a linear function of relative soil moisture:

$$K = \begin{cases} \frac{1}{1-0.35} \left( \frac{\theta}{\theta_{\text{sat}}} - 0.35 \right) & T_s \geq 0^\circ\text{C} \\ \frac{\theta}{\theta_{\text{sat}}} & T_s < 0^\circ\text{C} \end{cases}. \quad (41)$$

$K$  is limited to be between 0 and 1.  $\lambda_w$  and  $\lambda_i$  are the thermal conductivities of water and ice,  
 respectively.  $\lambda_s$  and  $\lambda_{\text{dry}}$  are globally uniform soil parameters (Table 3). Alternatively the values can  
 385 be chosen to be dependent on soil texture and soil organic carbon content following as described in  
 Appendix B. The inclusion of variable  $\lambda_s$  and  $\lambda_{\text{dry}}$  does not fundamentally affect the main model  
 results, hence for computational efficiency the parameters are taken to be uniform in space and  
 constant in time by default.

## 5 Hydrology

### 390 5.1 Canopy water

Re-evaporation of canopy intercepted water contributes significantly to the total water flux from the  
 surface to the atmosphere (e.g. Dirmeyer et al., 2006). Therefore, PALADYN includes a represen-  
 tation of rain and snow intercepted by vegetation. Rain is assumed to be intercepted only by trees  
 while snow is intercepted by all PFTs. The prognostic equations for canopy liquid water ( $w_{\text{can}}^w$ ) and  
 395 snow ( $w_{\text{can}}^s$ ) are similar and written in terms of canopy interception, canopy evaporation/sublimation  
 and a canopy water removal term as:

$$\frac{dw_{\text{can}}^{w/s}}{dt} = I_{\text{can}}^{w/s} - E_{\text{can}}^{w/s} - \frac{w_{\text{can}}^{w/s}}{\tau_{w/s}}. \quad (42)$$

Canopy interception and evaporation are given by:

$$I_{\text{can}}^{w/s} = \alpha_{\text{int}}^{w/s} P_{r/s} (1 - \exp[-k_{\text{ext}}(L_{\text{ai}} + S_{\text{ai}})]), \quad (43)$$

$$400 \quad E_{\text{can}}^{w/s} = \frac{\rho_a}{r_a} (q_{\text{sat}}(T_*) - q_a) f_{\text{can}}^{w/s}. \quad (44)$$

$P_r$  is the rain rate and  $P_s$  the snowfall rate.  $\alpha_{\text{int}}^w$  and  $\alpha_{\text{int}}^s$  are interception factors (Table 2). The wet  
 canopy fraction  $f_{\text{can}}^w$  and the snow covered canopy fraction  $f_{\text{can}}^s$  are assumed to increase linearly  
 with  $w_{\text{can}}^w$  and  $w_{\text{can}}^s$ , respectively, up to a maximum water and snow amount that the canopy can  
 hold,  $w_{\text{can}}^{\text{max}} = 0.2(L_{\text{ai}} + S_{\text{ai}})$  (e.g. Verseghy et al., 1993).  $\tau_w$  and  $\tau_s$  are the water and snow canopy  
 405 removal time scales, respectively (Table 2). Negative canopy evaporation, that is dew deposition, is



inhibited. If skin temperature is greater than  $0^{\circ}\text{C}$ , all snow is removed from the canopy and added to the snow layer on the ground. Finally  $E_{\text{can}} = E_{\text{can}}^{\text{w}} + E_{\text{can}}^{\text{s}}$  is diagnosed and used in the solution of the surface energy balance equation (Eq. (1)). The rate of rain and snow reaching the ground is then derived as:

$$410 \quad P_{\text{r/s,g}} = P_{\text{r/s}} - E_{\text{can}}^{\text{w/s}} - \frac{dw_{\text{can}}^{\text{w/s}}}{dt}. \quad (45)$$

The area weighted  $P_{\text{r/s,g}}$  over the vegetated and bare soil surface tiles are then used as input to the surface hydrology module.

## 5.2 Snow

The snow water equivalent evolution of the single snow layer is determined by the snowfall rate  $P_{\text{s,g}}$ ,  
 415 the snowmelt rate  $M_{\text{s}}$  and sublimation  $E_{\text{s}}$ :

$$\frac{dw_{\text{sn}}}{dt} = P_{\text{s,g}} - M_{\text{s}} - E_{\text{s}}. \quad (46)$$

To prevent an indefinite accumulation of snow,  $w_{\text{sn}}$  is limited to be below  $w_{\text{sn,crit}} = 1000 \text{ kg m}^{-2}$  and the snow excess is added to 'frozen water runoff'.

The density of snow is important because it determines the thickness of snow and hence influences  
 420 surface albedo and surface roughness and because it controls the thermal properties of snow (Section 4.1). The parameterisation of snow density is based partly on Anderson (1976); Pitman et al. (1991). The density of freshly fallen snow is temperature dependent following Anderson (1976):

$$\rho_{\text{sn,fresh}} = \rho_{\text{sn,min}} + 1.7(T_{\text{a}} - T_0 + 15)^{1.5} \quad T_0 - 15 < T_{\text{a}} < T_0 + 2. \quad (47)$$

$\rho_{\text{sn,min}}$  is the minimum snow density (Table 2). The effect of self-loading on snow compaction is  
 425 taken into account using the relation proposed by Kojima (1967) as implemented in Pitman et al. (1991) and the prognostic equation for snow density accounting also for the density of freshly fallen snow is written as (Pitman et al., 1991):

$$\frac{d\rho_{\text{sn}}}{dt} = \frac{0.5g\rho_{\text{sn}}w_{\text{sn}}}{\eta} + P_{\text{s,g}} \frac{\rho_{\text{sn,fresh}} - \rho_{\text{sn}}}{w_{\text{sn}}}, \quad (48)$$

where  $\eta$  is the viscosity depending both on the load and temperature:

$$430 \quad \eta = \eta_0 \exp[k_{\text{T}}(T_0 - T_{\text{s}}) + k_{\rho}\rho_{\text{sn}}]. \quad (49)$$

The values of the parameters  $\eta_0$ ,  $k_{\text{T}}$  and  $k_{\rho}$  are given in Table 2. The effects of snow metamorphism and snow melting on snow density are neglected. Snow thickness is then computed as:

$$h_{\text{sn}} = \frac{w_{\text{sn}}}{\rho_{\text{sn}}}. \quad (50)$$



### 5.3 Surface runoff and infiltration

435 Subgrid scale surface hydrology is represented using a TOPMODEL approach (Beven and Kirkby,  
 1979) as implemented in Niu et al. (2005). The fraction of a grid cell that is assumed to be at  
 saturation,  $f_{\text{sat}}$ , is determined by the grid cell mean water table position ( $z_{\nabla}$ ) and the spatially  
 varying maximum saturated fraction  $f_{\text{sat}}^{\text{max}}$  computed by Stocker et al. (2014) from the compound  
 topographic index (CTI) derived from the high resolution ETOPO1 topography as (Niu et al., 2005):

440

$$f_{\text{sat}} = f_{\text{sat}}^{\text{max}} e^{-f_{\nabla} z_{\nabla}}. \quad (51)$$

$f_{\nabla}$  is a parameter whose value is given in Table 2. If the surface is snowfree the wetland fraction is  
 set equal to the saturated fraction ( $f_{\text{wet}} = f_{\text{sat}}$ ), while it is set to zero otherwise. The grid cell mean  
 water table depth is estimated directly from the volumetric water content in the soil column, the peat

445 fraction ( $f_{\text{peat}}$ ) and the water table in peat ( $z_{\nabla}^{\text{peat}}$ ) as:

$$z_{\nabla} = (1 - f_{\text{peat}}) \left( h_{\text{soil}} - \sum_l \frac{\theta_l}{\theta_{\text{sat},l}} \Delta z_l \right) + f_{\text{peat}} z_{\nabla}^{\text{peat}}. \quad (52)$$

$h_{\text{soil}}$  is the soil column depth and the sum is over all soil layers. The peat water table is assumed  
 to follow the grid cell mean seasonal water table variations but with an amplitude limited to the  
 acrotelm thickness (Section 6.3.1). The maximum soil infiltration rate is then computed from the

450 saturated hydraulic conductivity of the top soil layer ( $k_{\text{sat},1}$ ) assuming that infiltration can occur  
 only in the unsaturated part of the grid cell:

$$q_{\text{inf}}^{\text{max}} = k_{\text{sat},1} (1 - f_{\text{sat}}). \quad (53)$$

Surface runoff is then calculated assuming that all liquid water that reaches the surface is routed  
 directly to runoff over the saturated fraction of the grid cell and considering that the maximum

455 infiltration rate can not be exceeded:

$$R_w = f_{\text{sat}} (P_{r,g} + M_s) + (1 - f_{\text{sat}}) \cdot \max(0, P_{r,g} + M_s - q_{\text{inf}}^{\text{max}}). \quad (54)$$

The actual soil infiltration rate is then computed as:

$$q_{\text{inf}} = P_{r,g} + M_s - R_w. \quad (55)$$

### 5.4 Soil hydrology

460 Water in the soil is assumed to be limited to flow in the vertical direction. Making use of the con-  
 servation of mass, the change in volumetric water content over time is then given by the vertical  
 divergence of the water flux and a sink term from soil water extraction by evapotranspiration ( $e$ ):

$$\rho_w \Delta z_l \frac{d\theta_{w,l}}{dt} = q_{l-1} - q_l - e_l, \quad (56)$$



where  $l$  is the soil layer index. This equation is solved with infiltration ( $q_{inf}$ ) as top boundary con-  
 465 dition and a free drainage bottom boundary condition, i.e. the water flux at the bottom of the soil  
 column ( $q_{drain}$ ) is set equal to the bottom hydraulic conductivity. The soil water flux  $q$  is expressed  
 by Darcy's law:

$$q = k \frac{\partial(\psi - z)}{\partial z}, \quad (57)$$

where  $k$  is the hydraulic conductivity and  $\psi$  is the matric potential.  $z$  is the vertical coordinate and  
 470 is positive downwards from the surface. The numerical solution of Eq. (56) follows the formulation  
 in Oleson et al. (2013).

The hydraulic conductivity and the matric potential are soil hydraulic properties dependent on soil  
 texture and volumetric soil water following Clapp and Hornberger (1978):

$$\psi = \psi_{sat} \left( \frac{\theta_w}{\theta_{sat}} \right)^{-b} \quad (58)$$

$$475 \quad k = k_{sat} \left( \frac{\theta_w}{\theta_{sat}} \right)^{2b+3}. \quad (59)$$

Similarly to the discussion on soil thermal parameters in Section 4.1, hydraulic conductivity and  
 matric potential at saturation,  $k_{sat}$  and  $\psi_{sat}$ , and the Clapp and Hornberger parameter  $b$  are set to  
 global uniform values by default (Table 3). However, a soil texture and soil organic matter content  
 dependent formulation of  $k_{sat}$ ,  $\psi_{sat}$  and  $b$  is also available (Appendix B).

## 480 6 Biogeochemistry and vegetation dynamics

### 6.1 Photosynthesis

Daily photosynthesis is modelled following the general light use efficiency model described in Hax-  
 eltine and Prentice (1996a, b) as implemented in the LPJ dynamic vegetation model (Sitch et al.,  
 2003), with some modifications. Compared to other models it has the advantage that it computes  
 485 daily integrated photosynthesis without the need to explicitly resolve the diurnal cycle and therefore  
 saves computing time. It also makes it convenient to be coupled to the physical PALADYN compo-  
 nents, which are also integrated with a daily time step. Daily gross photosynthesis is computed from  
 a light limited ( $J_E$ ) and a Rubisco limited rate ( $J_C$ ) as:

$$490 \quad A_g = \frac{J_E + J_C - \sqrt{(J_E + J_C)^2 - 4\theta_r J_E J_C}}{2\theta_r} \beta_\theta. \quad (60)$$

$$J_E = c_1 \cdot APAR, \quad (61)$$

$$J_C = c_2 \cdot V_m. \quad (62)$$

$\theta_r$  is a shape parameter and  $APAR$  is the absorbed photosynthetically active radiation computed as:

$$495 \quad APAR = 0.5 SW^\downarrow \alpha_a (1 - e^{-k_{ext} L_{ai}}) \Delta t (1 - \alpha_{leaf}) c_q. \quad (63)$$





Half of the downwelling shortwave radiation is assumed to be in the photosynthetically active wavelength range,  $\alpha_a$  accounts for reductions in PAR utilisation efficiencies in natural ecosystems, the factor  $1 - e^{-k_{\text{ext}}L_{\text{ai}}}$  scales to the canopy,  $\alpha_{\text{leaf}}$  is the leaf albedo in the PAR range,  $\Delta t$  is the length of day in seconds and  $c_q$  is a conversion factor from  $\text{J m}^{-2}$  to  $\text{mol m}^{-2}$ . Parameter values are given  
 500 in Table 4 and more details on the formulation of  $c_1$  and  $c_2$  and the maximum daily rate of net photosynthesis  $V_m$  are given in Appendix C.

Leaf respiration,  $R_d$ , is scaled to  $V_m$  as:

$$R_d = a_{C3/4} V_m \beta_\theta, \quad (64)$$

and daily net assimilation is then calculated as:

$$505 \quad A_n = A_g - R_d. \quad (65)$$

Daytime net assimilation can then be computed by adding nighttime respiration:

$$A_{\text{nd}} = A_n + \left(1 - \frac{d_h}{24}\right) R_d. \quad (66)$$

$\beta_\theta$  is a soil moisture limiting factor:

$$\beta_\theta = \sum_l \frac{\theta_{w,l} - \theta_{\text{wp}}}{\theta_{\text{fc}} - \theta_{\text{wp}}} r_l, \quad (67)$$

510  $\theta_{\text{wp}}$  and  $\theta_{\text{fc}}$  are the soil moisture values at wilting point and field capacity, respectively.  $r_l$  is the fraction of roots in layer  $l$  (section 6.2.2). If the soil temperature of layer  $l$  is below  $-2^\circ\text{C}$  the corresponding term in Eq. (67) is set to 0.

$c_1$  and  $c_2$  depend on the intercellular partial pressure of  $\text{CO}_2$  ( $p_i$ ), which is proportional to the atmospheric  $\text{CO}_2$  concentration ( $p_a$ ):

$$515 \quad p_i = \lambda_c p_a. \quad (68)$$

In LPJ  $\lambda_c$  is computed iteratively from potential and actual evapotranspiration (Sitch et al., 2003). To reduce the computation cost and in light of recent developments, in PALADYN  $\lambda_c$  is derived from the optimal stomatal conductance model (Medlyn et al., 2011), which predicts that stomatal conductance for water vapour  $g_{\text{can}}$  is given by:

$$520 \quad g_{\text{can}} = g_{\text{min}} + \left(1 + \frac{g_1}{\sqrt{VPD}}\right) \frac{A_{\text{nd}}}{c_a}. \quad (69)$$

$VPD$  is the vapor pressure deficit between leaf surface and ambient air. Since  $\text{CO}_2$  has to diffuse through the stomata into the leaf interior before being fixed by photosynthesis and at the same time water vapour diffuses through the stomata from the leaf interior to the canopy air,  $g_{\text{can}}$  and  $A_{\text{nd}}$  are also related by:

$$525 \quad g_{\text{can}} = g_{\text{min}} + 1.6 \frac{A_{\text{nd}}}{c_a - c_i}. \quad (70)$$



$g_{\min}$  is a minimum stomatal conductance (Table 5) and  $c_a$  and  $c_i$  are the atmospheric and intercellular  $\text{CO}_2$  mole fractions. From Eqs. (69) and (70)  $\lambda_c$  can simply be derived (e.g. Medlyn et al., 2011):

$$\lambda_c = 1 - \frac{1.6}{1 + g_1/\sqrt{VPD}}. \quad (71)$$

To a first approximation, the values of  $g_1$  are taken to be constant PFT specific parameters (Table 5) based on the data reported in Lin et al. (2015). As will be shown in section 6.5, based on a simple model, the ratio of  $c_i$  and  $c_a$  is also the main parameter determining the carbon isotopic discrimination during photosynthesis. Therefore the PFT specific discrimination is used as an additional constraint on  $g_1$  values.

Finally, maintenance respiration and growth respiration are computed and net primary production ( $NPP$ ) is derived as in Sitch et al. (2003).

## 6.2 Vegetation dynamics

There are a number of existing dynamic global vegetation models spanning a large range of different approaches of varying complexity. The appropriate model complexity for PALADYN, balancing low computational expenses and a realistic representation of continental-scale vegetation dynamics, is represented by the top-down modelling approach of the TRIFFID dynamic global vegetation model (Cox, 2001; Clark et al., 2011). Another main advantage of this type of model is that it does not require interannual climate variability, which can not be provided by a statistical-dynamical atmosphere model like CLIMBER. The PALADYN dynamic vegetation scheme is therefore based on TRIFFID. The model distinguishes five plant functional types: broadleaved trees, needleleaved trees, C3 and C4 grass and shrubs. Vegetation carbon  $C_v$  and fractional area coverage  $\nu$  of each PFT  $i$  are described by a coupled system of first order differential equations based on the Lotka-Volterra approach for modelling competition between species:

$$\frac{dC_{v,i}}{dt} = (1 - \lambda_{NPP,i})NPP_i - \Lambda_{loc,i}, \quad (72)$$

$$\frac{d\nu_i}{dt} = \frac{\lambda_{NPP,i}NPP_i}{C_{v,i}}\nu_{i,*} \left( 1 - \sum_j c_{ij}\nu_j \right) - \gamma_{\nu,i}\nu_{i,*}. \quad (73)$$

$\nu_{i,*} = \max(\nu_i, \nu_{\text{seed}})$ , where  $\nu_{\text{seed}}$  is a small seeding fraction used to ensure that a PFT is always seeded (Table 6).  $\lambda_{NPP}$  is a factor determining the partitioning of  $NPP$  between increase of vegetation carbon of the existing vegetated area (Eq. (72)) and spreading of the given PFT (Eq. (73)) and is given by:

$$\lambda_{NPP} = \begin{cases} 0 & L_{ai,b} < L_{ai}^{\min} \\ \frac{L_{ai,b} - L_{ai}^{\min}}{L_{ai}^{\max} - L_{ai}^{\min}} & L_{ai}^{\min} \leq L_{ai,b} \leq L_{ai}^{\max} \\ 1 & L_{ai,b} > L_{ai}^{\max}. \end{cases} \quad (74)$$



555  $L_{ai,b}$  is the 'balanced' leaf area index that would be reached if the plant was in full leaf and  $L_{ai}^{\min}$  and  $L_{ai}^{\max}$  are PFT specific parameters (Table 5).  $\Lambda_{loc}$  is the local litterfall rate:

$$\Lambda_{loc} = \Lambda_l + \gamma_r C_{v,r} + \gamma_s C_{v,s}. \quad (75)$$

Litterfall from leaf turnover is given by  $\Lambda_l = \gamma_l C_{v,l}$  for evergreen plants and is computed from the phenological status (section 6.2.1) for deciduous plants. The  $\gamma_s$  are PFT dependent turnover rates of  
 560 leaf, root and stem carbon (Table 5). Vegetation carbon  $C_v$  is directly related to the balanced leaf area index through the relations of leaf ( $C_{v,l}$ ), root ( $C_{v,r}$ ) and stem ( $C_{v,s}$ ) carbon to  $L_{ai,b}$ :

$$C_{v,l} = \frac{L_{ai,b}}{SLA}, \quad (76)$$

$$C_{v,r} = \mathcal{L}, \quad (77)$$

$$C_{v,s} = a_{wl} L_{ai,b}^{5/3}. \quad (78)$$

565  $C_v = C_{v,l} + C_{v,r} + C_{v,s}. \quad (79)$

$SLA$  is the specific leaf area and is PFT dependent following Kattge et al. (2011) (Table 5).  $a_{wl}$  is a PFT specific allometric coefficient (Table 5). The competition coefficients,  $c_{ij}$ , represent the impact of vegetation type  $j$  on the vegetation type of interest  $i$ . TRIFFID is based on a tree-shrub-grass dominance hierarchy with dominant types  $i$  limiting the expansion of sub-dominant types  $j$  ( $c_{ji} = 1$ ),  
 570 but not vice-versa ( $c_{ij} = 0$ ). While in TRIFFID the tree types and grass types co-compete with competition coefficients dependent on their relative heights, in PALADYN they compete only based on their  $NPP$  ( $c_{ij} = 0.5$  and  $c_{ji} = 0.5$ ). Additionally, in PALADYN we implemented a dependence of the competition coefficients on bioclimatic limits, i.e. the coldest month temperature ( $T_{cmon}^{\min/\max}$ ) and growing degree days ( $gdd_{\min}$ ) as given in Table 5. In a given grid cell, PFTs outside of the  
 575 bioclimatic limits are not competitive and will be dominated by other PFTs, regardless of the tree-shrub-grass dominance.

The last term in Eq. (73) represents vegetation disturbance. In TRIFFID, the disturbance rate  $\gamma_v$  is taken to be a constant PFT specific parameter. In reality, on a global scale, disturbance is mainly caused by fire, which shows a strong dependence on climatic conditions and fuel availability (e.g.  
 580 Thonicke et al., 2010). We therefore introduce a simple parameterisation for fire disturbance based on top-soil moisture and aboveground biomass loosely following Reick et al. (2013) and Arora and Boer (2005):

$$\gamma_v = \gamma_{v,\min} + \frac{1}{\tau_{fire}} \max\left(0, \frac{\theta_{crit} - \theta_1}{\theta_{crit}}\right) \max\left(0, \min\left(1, \frac{C_{v,ag} - C_{v,low}}{C_{v,high} - C_{v,low}}\right)\right). \quad (80)$$

$\gamma_{v,\min}$  is a minimum constant disturbance rate intended to represent disturbances other than fire  
 585 (e.g. windthrow (Reick et al., 2013) and insect outbreaks, among others (e.g. Dale et al., 2001)) (Table 6).  $\tau_{fire}$  is a characteristic fire return time scale,  $\theta_{crit}$  is the critical soil moisture below which fires can occur and  $C_{v,low}$  and  $C_{v,high}$  are values of aboveground biomass ( $C_{v,ag}$ ) that define the fuel availability limitation function. All parameter values are listed in Table 6.



Vegetation height is computed from stem carbon following Cox (2001):

$$590 \quad h_v = \frac{C_{v,s}}{0.01 \cdot a_{ws}} \left( \frac{a_{wl}}{C_{v,s}} \right)^{3/5}. \quad (81)$$

$a_{ws}$  is the ratio of total to respiring stem carbon (Table 5). The stem area index,  $S_{ai}$ , is taken to be 1/10 of  $L_{ai,b}$ .

The dynamic vegetation model has a monthly time step.

### 6.2.1 Phenology

595 The phenology of the PFTs is controlled by the coldest month temperature following Sitch et al. (2003). If the coldest month temperature falls below a PFT specific value  $T_{cmon}^{phen}$  (Table 5), then the PFT in the gridcell is assumed to be deciduous and  $L_{ai}$  is computed from:

$$L_{ai} = \phi L_{ai,b}. \quad (82)$$

$\phi$  increases linearly with the growing degree days ( $gdd$ ) above a PFT specific base temperature  $T_{base}^{gdd}$ ,

600 at a PFT specific rate determined by  $gdd_{crit}$ :

$$\phi = \frac{gdd}{gdd_{crit}}. \quad (83)$$

After  $\phi$  reaches its maximum value of 1 it remains constant until the air temperature drops below  $T_{base}^{gdd}$ . Then leaf senescence starts when the temperature drops below  $T_{base}^{gdd}$  and continues until all leaves are lost to litter at 5 °C below  $T_{base}^{gdd}$ . Raingreen phenology is not represented in the model.

605 Needleleaf trees are assumed to always be evergreen, because given the low PFT specific leaf area (Table 5), they would not be competitive in very cold regions if they were deciduous.

### 6.2.2 Root distribution

The vertical distribution of roots in the soil plays an important role in land surface models. It determines the water that is accessible to the plants and hence controls the exchange of water between  
 610 the surface and the atmosphere. Water availability affects also plant productivity and consequently plays an important role in the competition between plant functional types. It also controls the vertical distribution of root litter input to the soil which is an important factor determining vertical soil carbon distribution. In PALADYN we adopt the root distribution scheme proposed by Zeng (2001). The root fraction in each soil layer ( $r_l$ ) is derived from the cumulative root fraction:

$$615 \quad r(z) = 1 - 0.5 \left( e^{-d_{r,1}z} + e^{-d_{r,2}z} \right). \quad (84)$$

$d_{r,1}$  and  $d_{r,2}$  are PFT specific parameters (Table 5).

### 6.3 Soil carbon

Traditionally, in terrestrial biosphere models soil carbon has been represented in terms of vertically-integrated pools. Only recently vertically discretized soil carbon has started to be included in these



620 models (e.g. Koven et al., 2009; Schaphoff et al., 2013). Vertically integrated models are unable  
 to represent soil carbon dynamics in permafrost areas, where only part of the carbon stored in the  
 soil column is affected by the seasonal thawing of the upper soil. Large quantities of carbon are  
 stored in the permanently frozen soils around the Arctic (Tarnocai et al., 2009; Hugelius et al., 2014;  
 Schuur et al., 2015) and to model the dynamics of this carbon stock it is necessary to include carbon  
 625 separately in different soil layers. A proper representation of the permafrost carbon pool is important  
 especially for carbon cycle modelling over long time scales.

Therefore, PALADYN has carbon distributed over the different soil layers where temperature and  
 soil water are also computed. Additionally, each grid cell distinguishes between soil carbon in four  
 different soil columns: mineral soil carbon and peat carbon below the vegetated surface tile, buried  
 630 carbon below ice sheets and shelf carbon below the water on the ocean shelf (Fig. 1c). Each layer  
 generally contains three carbon pools with different decomposability (Fig. 3). For unfrozen mineral  
 soil carbon the three pools are organized into litter, fast and slow carbon following (Sitch et al.,  
 2003). This structure is modified for peatlands, perennially frozen soils and buried carbon.

The generic prognostic equations for litter, fast and slow soil carbon pools are written as:

$$635 \quad \frac{\partial C_{\text{lit}}(z)}{\partial t} = \Lambda(z) - k_{\text{lit}}(z)C_{\text{lit}}(z) + \frac{\partial}{\partial z} \left( D(z) \frac{\partial C_{\text{lit}}}{\partial z} \right) \quad (85)$$

$$\frac{\partial C_{\text{fast}}(z)}{\partial t} = (1 - f_{\text{lit}}^{\text{resp}})f_{\text{lit} \rightarrow \text{fast}}k_{\text{lit}}(z)C_{\text{lit}}(z) - k_{\text{fast}}(z)C_{\text{fast}}(z) + \frac{\partial}{\partial z} \left( D(z) \frac{\partial C_{\text{fast}}}{\partial z} \right) \quad (86)$$

$$\frac{\partial C_{\text{slow}}(z)}{\partial t} = (1 - f_{\text{lit}}^{\text{resp}})f_{\text{lit} \rightarrow \text{slow}}k_{\text{lit}}(z)C_{\text{lit}}(z) - k_{\text{slow}}(z)C_{\text{slow}}(z) + \frac{\partial}{\partial z} \left( D(z) \frac{\partial C_{\text{slow}}}{\partial z} \right). \quad (87)$$

Litter carbon is increased by litterfall  $\Lambda(z)$ . A fraction  $f_{\text{lit}}^{\text{resp}}$  of the decomposed litter carbon goes  
 directly into the atmosphere, while the rest goes partly into the fast carbon pool ( $f_{\text{lit} \rightarrow \text{fast}}$ ) and partly  
 640 into the slow carbon pool ( $f_{\text{lit} \rightarrow \text{slow}}$ ) (Table 7). Each carbon pool decomposes at a specific rate  
 $k$ , which depends on soil temperature and soil moisture. The vertical redistribution of soil carbon  
 between soil layers is represented as a diffusive process with diffusivity  $D(z)$ .

Over the vegetated grid cell part, the local litter, the litter originating from competition between  
 the PFTs and the litter from large scale disturbances are aggregated to give an average litterfall  
 645 ( $\Lambda_{\text{veg}}(z)$ ) as in (Cox, 2001). Litter from the roots is added to the different soil layers depending on  
 the root fraction in each layer, while litter from leaves and stem is added to the top soil layer.

When ice sheets are expanding into vegetated areas, a fraction  $f_{\text{veg} \rightarrow \text{bur}}$  of the vegetation carbon  
 is assumed to be directly buried below the ice and the remaining is added to the litter pools of the  
 vegetated part:

$$650 \quad \Lambda_{\text{bur}}(z) = f_{\text{veg} \rightarrow \text{bur}} \overline{C_v}(z) \Delta f_{\text{ice}} \quad (88)$$

$$\Lambda_{\text{veg}}(z) = (1 - f_{\text{veg} \rightarrow \text{bur}}) \overline{C_v}(z) \Delta f_{\text{ice}}. \quad (89)$$



$\overline{C}_v(z)$  is the mean vegetation carbon content of the vegetated grid cell part in the different soil layers. For the purpose of litter computation the aboveground vegetation carbon is considered to be part of the top soil layer.  $\Delta f_{ice}$  is the increase of ice sheet fraction in the grid cell.

655 When sea level is rising and shelf areas become flooded, the flooded vegetation is assumed to die instantaneously and vegetation carbon is added directly to the shelf litter pool:

$$\Lambda_{shelf}(z) = \overline{C}_v(z) \Delta f_{shelf}, \quad (90)$$

where  $\Delta f_{shelf}$  is the increase in shelf fraction.

Vertical carbon diffusivity in unfrozen mineral soils is assumed to be determined by bioturbation  
 660 and  $D(z) = D_{bio}$  following Braakhekke et al. (2011) (Table 7). In permafrost areas the diffusivity represents cryoturbation in the active layer.  $D(z)$  is set to a constant value in the active layer and is assumed to linearly decrease below it to a value of zero at a multiple ( $n_{al}$ ) of the active layer thickness  $z_{al}$  (Koven et al., 2009):

$$D(z) = \begin{cases} D_{cryo} & z \leq z_{al} \\ D_{cryo} \left(1 - \frac{z - z_{al}}{(n_{al} - 1)z_{al}}\right) & z_{al} < z \leq n_{al}z_{al}. \end{cases} \quad (91)$$

665 The value of  $D_{cryo}$  is given in Table 7.

The decomposition rates for mineral soil carbon depend on temperature, liquid water content in the soil layers and inundated fraction of the grid cell:

$$k_x^{min}(z) = (1 - f_{inun})k_{x,10}f_T(z)f_\theta(z) + f_{inun}k_{x,10}f_T(z)f_{\theta,sat}(z), \quad (92)$$

for  $x = lit, fast, slow$ . The inundated grid cell fraction is the wetland fraction with the peatland frac-  
 670 tion removed,  $f_{inun} = f_{wet} - f_{peat}$ .  $k_{lit,10}$ ,  $k_{fast,10}$  and  $k_{slow,10}$  are the litter, fast and slow carbon decomposition rates at 10 °C and field capacity and are given in Table 7. The temperature dependence follows a modified Arrhenius equation (Lloyd and Taylor, 1994):

$$f_T(z) = \exp \left[ 308.56 \left( \frac{1}{56.02} - \frac{1}{46.02 + T(z) - T_0} \right) \right]. \quad (93)$$

The soil moisture dependence is taken from Porporato et al. (2003) and gives a linear increase of the  
 675 decomposition rate up to field capacity and a hyperbolic decrease above field capacity:

$$f_\theta(z) = \begin{cases} \frac{\theta_w(z)}{\theta_{fc}} & \theta_w(z) \leq \theta_{fc} \\ \frac{\theta_{fc}}{\theta_w(z)} & \theta_w(z) > \theta_{fc}. \end{cases} \quad (94)$$

The soil moisture dependence factor for inundated land,  $f_{\theta,sat}$ , is simply the value of  $f_\theta$  at saturation.

PALADYN allows for the possibility to effectively treat the carbon in frozen soils as inert. If inert  
 680 permafrost carbon is switched on, the decomposition rates in Eq. 92 are additionally weighted by a frozen soil factor,  $f_{inert}$ :

$$k_x^{min}(z) = (1 - f_{inert}(z))k_x^{min}(z) + f_{inert}(z)k_{inert}, \quad (95)$$



for  $x = \text{lit, fast, slow}$ . All carbon is assumed to be inert if the fraction of frozen water in a layer exceeds  $f_{\text{frz,crit}}$ :

$$f_{\text{inert}}(z) = \min\left(1, \frac{1}{f_{\text{frz,crit}}} \frac{\theta_i}{\theta_i + \theta_w}\right). \quad (96)$$

685 Therefore in soil layers where at least a fraction  $f_{\text{frz,crit}}$  of water is frozen all year round, carbon is effectively decomposing at the very low rate  $k_{\text{inert}}$ .

More details on the parameterisation of carbon dynamics below ice sheets and on the ocean shelf and of permafrost carbon will be given in a future paper dedicated to processes active on glacial-interglacial cycles time scales.

### 690 6.3.1 Peatlands

Peat carbon is treated slightly differently from the other carbon pools. We follow the approach of Kleinen et al. (2012) and distinguish between a surface litter layer and an acrotelm layer where carbon is decomposed partly under oxic and partly under anoxic conditions, depending on the position of the water table. Both litter and acrotelm are assumed to be contained in the top soil layer. In the  
 695 layers below, the catotelm, decomposition occurs without oxygen all year round. The prognostic equations for peat litter, acrotelm and catotelm carbon are:

$$\frac{\partial C_{\text{lit}}^{\text{peat}}}{\partial t} = \Lambda_{\text{peat}} - k_{\text{lit}}^{\text{peat}} C_{\text{lit}}^{\text{peat}} \quad (97)$$

$$\frac{\partial C_{\text{acro}}}{\partial t} = (1 - f_{\text{lit}}^{\text{resp}}) k_{\text{lit}}^{\text{peat}} C_{\text{lit}}^{\text{peat}} - k_{\text{acro} \rightarrow \text{cato}} C_{\text{acro}} - k_{\text{acro}} C_{\text{acro}} \quad (98)$$

$$\frac{\partial C_{\text{cato}}(z)}{\partial t} = k_{\text{acro} \rightarrow \text{cato}} C_{\text{acro}} - k_{\text{cato}}(z) C_{\text{cato}}(z). \quad (99)$$

700 The transfer from acrotelm to catotelm carbon occurs only once a critical acrotelm carbon content  $C_{\text{acro,crit}} = 5 \text{ kgC m}^{-2}$  is reached, as suggested by (Wania et al., 2009). Typical acrotelm carbon densities are around  $20 \text{ kgC m}^{-3}$ , so this threshold roughly corresponds to assuming that transfer to the catotelm starts when the acrotelm reaches a thickness of 25 cm, which is a typical value of observed acrotelm thickness. When this threshold is exceeded, acrotelm carbon is transferred to the  
 705 catotelm in the second soil layer. Peat is assumed to grow thicker by accumulating carbon on top and therefore in the model the catotelm is shifted to lower soil layers once the catotelm carbon density  $C_{\text{cato,crit}}$  has been exceeded in a given layer. For the same reason the vertical diffusivity of peat carbon is set to 0. Litterfall over peatlands is assumed to be the same as over mineral soil, but to be added to the top soil layer only:  $\Lambda_{\text{peat}} = \sum_z \Lambda_{\text{veg}}(z)$ . The decomposition rates for litter, acrotelm  
 710 and catotelm are given by:

$$k_{\text{lit}}^{\text{peat}} = k_{\text{lit},10} f_{\text{T}}(1) (f_{\text{oxic}} + (1 - f_{\text{oxic}}) f_{\theta,\text{peat}}) \quad (100)$$

$$k_{\text{acro}} = k_{\text{acro},10} f_{\text{T}}(1) (f_{\text{oxic}} + (1 - f_{\text{oxic}}) f_{\theta,\text{peat}}) \quad (101)$$

$$k_{\text{cato}}(z) = k_{\text{cato},10} f_{\text{T}}(z) f_{\theta,\text{peat}}. \quad (102)$$



Since peatland soil temperature is not separately computed by the model, the temperature factor is  
 715 calculated using the grid cell mean temperature.  $f_{\theta, \text{peat}}$  is taken to be equal to 0.3 as in Wania et al.  
 (2009); Koven et al. (2013). The values of the reference decomposition rates are given in Table 7.  
 The fraction of litter and acrotelm that is respiring in oxic conditions,  $f_{\text{oxic}}$ , is determined from the  
 mean grid cell water table depth  $z_{\nabla}$  and the minimum monthly water table position  $z_{\nabla}^{\text{min}}$  assuming  
 that the seasonal water table variations in the peatland fraction follow the grid cell mean water table  
 720 and that the amplitude of water table variations in peatland is reduced compared to the grid cell mean  
 and limited to the acrotelm thickness:

$$f_{\text{oxic}} = \frac{\min(z_{\text{acro}}, \max(0, z_{\nabla} - z_{\nabla}^{\text{min}}))}{z_{\text{acro}}} \quad (103)$$

Peatland expansion and contraction is modelled partly following Stocker et al. (2014). The grid  
 cell fraction that is wetland for at least 3 months of the year is considered to be potential peatland  
 725 area  $f_{\text{peat}}^{\text{pot}}$ . The actual peatland area  $f_{\text{peat}}$  is simulated as:

$$f_{\text{peat}, n+1} = \begin{cases} \min((1+r)f_{\text{peat}, n}, f_{\text{peat}}^{\text{pot}}) & \frac{dC_{\text{peat}}}{dt} \geq \left. \frac{dC_{\text{peat}}}{dt} \right|_{\text{crit}} \quad \text{or} \quad C_{\text{peat}} \geq C_{\text{peat}}^{\text{crit}} \\ \max((1-r)f_{\text{peat}, n}, f_{\text{peat}}^{\text{min}}) & \frac{dC_{\text{peat}}}{dt} < \left. \frac{dC_{\text{peat}}}{dt} \right|_{\text{crit}} \quad \text{and} \quad C_{\text{peat}} < C_{\text{peat}}^{\text{crit}} \end{cases} \quad (104)$$

Peat is expanding if the annual mean rate of carbon uptake ( $dC_{\text{peat}}/dt$ ) is greater than a critical  
 value  $dC_{\text{peat}}/dt|_{\text{crit}}$  or if peat carbon exceeds a value  $C_{\text{peat}}^{\text{crit}}$ , otherwise peatland area is shrinking.  
 To account for inertia in lateral peatland expansion and contraction, the relative areal change rate is  
 730 limited to 1 % yr<sup>-1</sup> ( $r = 0.01 \text{ yr}^{-1}$ ). When the peat area is changing, carbon is simply redistributed  
 between mineral soil and peat carbon pools layer-by-layer with the following rules:  $C_{\text{lit}}^{\text{peat}} \leftrightarrow C_{\text{lit}}$ ,  
 $C_{\text{acro}} \leftrightarrow C_{\text{fast}}$  and  $C_{\text{cato}} \leftrightarrow C_{\text{slow}}$ .

#### 6.4 Methane emissions

Methane emissions are simulated as a constant fraction of heterotrophic respiration when respiration  
 735 occurs under anaerobic conditions, as is the case in wetlands, peatlands and flooded ocean shelves.  
 The fraction of carbon that is respired as methane,  $f_{\text{CH}_4:\text{C}}$ , is different for wetlands, peatlands and  
 ocean shelf (Table 7).

#### 6.5 Carbon isotopes: <sup>13</sup>C and <sup>14</sup>C

The stable carbon isotope <sup>13</sup>C and radiocarbon <sup>14</sup>C are tracked in PALADYN through all carbon pools  
 740 in vegetation and soil. Discrimination is simulated only during photosynthesis and follows the model  
 outlined in Lloyd and Farquhar (1994). The discrimination factor  $\Delta$  for C3 and C4 photosynthesis  
 is given by:

$$\Delta = \begin{cases} 4.4 \frac{c_a - c_i}{c_a} + 27 \frac{c_i}{c_a} & \text{C3} \\ 4.4 \frac{c_a - c_i}{c_a} + (-5.7 + 20 \cdot 0.35) \frac{c_i}{c_a} & \text{C4.} \end{cases} \quad (105)$$





Radiocarbon decay is ignored in the vegetation carbon pools because of their fast turnover time  
745 relative to the  $^{14}\text{C}$  decay rate. In all soil carbon pools radiocarbon has a half life of 5730 years.

## 7 Model spinup

Some of the processes related to vegetation and soil carbon dynamics have very long intrinsic time  
scales and therefore long simulations of at least 10000 years would be required to get the system into  
an equilibrium state with prescribed boundary conditions. Even though this is in principle feasible  
750 with PALADYN, it is in fact impractical for test and tuning purposes. Therefore the possibility to  
run the vegetation and carbon cycle modules with an artificially high internal integration time step  
of 1000 or more years is implemented in PALADYN. This is possible due to the fully implicit  
formulation of the model components. In this equilibrium spinup mode the vegetation and carbon  
cycle modules are called only at the end of each simulation year but using annually cumulated NPP  
755 and litterfall and annual mean decomposition rates for soil carbon. Using the equilibrium spinup  
mode brings the model close to equilibrium already after around 100 years of simulation. 100 years  
is also the spinup time required to bring the physical state of the land model, particularly permafrost  
related processes, into equilibrium with climate. The equilibrium spinup mode can however not be  
applied to processes which are intrinsically out of equilibrium such as peatlands and inert permafrost  
760 carbon. To get the present state of these pools a transient simulation over at least one glacial cycle is  
required.

## 8 Evaluation

In this section the performance of PALADYN for present day is presented and discussed. The model  
is designed for large scale applications and therefore the model evaluation is done at a global scale,  
765 although in principle it would be possible to run the model in a single column mode forced with  
site level observations. For the model evaluation an offline transient simulation from 1901 to 2010  
is performed. In offline mode PALADYN needs several monthly climate fields as input as listed in  
Table 9. In addition the annual atmospheric  $\text{CO}_2$  concentration has to be provided. For the historical  
simulation of the past century the WATCH climate forcing (Weedon et al., 2011, 2014) based on  
770 ERA-40 (Uppala et al., 2005) and ERA-Interim reanalysis (Dee et al., 2011) combined with GPCP  
precipitation (Schneider et al., 2014) is used.  $\text{CO}_2$  is prescribed from Bereiter et al. (2015) combined  
with Manua Loa data (Keeling et al., 1976). Before running the transient experiment, the model is  
spun up for 100 years as described in section 7 with the mean 1901-1930 climate as forcing and the  
1901  $\text{CO}_2$  concentration of 295 ppm. To get a rough estimate of peatland area and carbon, during  
775 this equilibrium spinup phase, the peatland module is enabled to allow peatlands to establish. To  
allow the fast carbon processes to equilibrate, the model is subsequently run for additional 400 years  
with the dynamic vegetation and soil carbon modules called with a monthly timestep. Finally, the



model is run in transient mode for the historical period forced with annually varying climate and CO<sub>2</sub> concentrations. Peatland area is kept constant during this phase.

780 Depending on the time interval covered by the different observational data products, the model climatology over the given time period is computed and used to evaluate the different model components, as described next.

### 8.1 Physical processes

The modelled net radiation absorbed at the surface is in good agreement with reanalysis data both  
785 for the seasonal cycle and the annual mean (Fig. 4). With the downwelling shortwave and longwave radiation used as forcing, the net surface radiation is determined by the modelled surface emissivity and albedo. The surface albedo for winter and summer is well simulated in the model (Fig. 5).

A correct partitioning of the absorbed radiation between sensible, latent and ground heat flux is of fundamental importance for a land model. The modelled sensible heat flux compares well with  
790 ERA-Interim reanalysis data except for the tropics, where it is systematically overestimated and for the subtropics, where it is underestimated in the model (Fig. 6). Evapotranspiration, and therefore the latent heat flux, tends to be overestimated by the model everywhere except for the tropics when compared to estimates from Mueller et al. (2013) (Fig. 7). However, it is in good agreement with ERA-Interim. This is to be expected because evapotranspiration strongly depends on surface air  
795 conditions which are used to force the model, which are based on ERA-Interim. The discrepancy between model and (model-based) estimates from (Mueller et al., 2013) might therefore reflect a deficiency in the forcing rather than in the model.

Evapotranspiration is the sum of transpiration from vegetation, surface evaporation and canopy interception and re-evaporation. The partitioning of total evapotranspiration between the different  
800 components is shown in Fig. 8. Transpiration is dominant in the tropics and generally in densely vegetated areas. A significant amount of precipitation is directly re-evaporated back to the atmosphere from plant canopies, particularly in the tropics. Surface evaporation is the only process acting in desert regions. Globally, transpiration, surface evaporation and canopy evaporation account for around 50, 30 and 20 % of total evapotranspiration, respectively. This compares favorably with  
805 Dirmeyer et al. (2006), who estimated total global evapotranspiration to be partitioned in 48% from transpiration, 36% from soil evaporation, and 16% from canopy interception and re-evaporation using an ensemble of land surface models.

As a consequence of the overestimation of evapotranspiration, simulated runoff is underestimated, particularly over northern hemisphere mid-latitudes (Fig. 9). Compared to data from Fekete et al.  
810 (2002) the modelled NH runoff from melting snow in spring tends to be less concentrated to May and June and more gradually distributed over the whole summer season. Global annual runoff is 35 Pg yr<sup>-1</sup>.



Modelled DJF and JJA soil moisture shows generally a good agreement with estimates from satellite data (Liu et al., 2012; Wagner et al., 2012) in the tropics, while the model tends to simulate a  
815 dryer top soil in high northern latitudes (Fig. 10). However, it has to be mentioned that the satellite data are representative for the soil moisture of the top few cm of soil, while the top model soil layer is 20 cm thick.

The mean annual simulated wetland area is 3.2 mln km<sup>2</sup>. Maximum monthly wetland extent is generally well captured by the model, particularly over high northern latitudes (Fig. 11). Compared to  
820 the multi-satellite product from GIEMS (Prigent et al., 2007; Papa et al., 2010) the model simulates larger wetland areas in tropical forest areas. The modelled seasonal variation in global wetland area is in very good agreement with GIEMS (Fig. 12).

The NH spring evolution of snow mass is compared to the GlobSnow dataset (Takala et al., 2011; Luojus et al., 2013) in Fig. 13. The spatial distribution of snow is well captured by the model.  
825 However, the model tends to melt snow slightly too late in spring, as highlighted also by the seasonal evolution of the total NH snow mass (Fig. 14). The interannual variability of spring snow over the NH is also largely in agreement with the GlobSnow data, suggesting that the model has a reasonably good sensitivity (Fig. 15).

Modelled permafrost area is 16.5 mln km<sup>2</sup>, which compares well with observations (Table 8).  
830 The permafrost extent over Siberia and Northern Canada is generally well simulated by the model (Fig. 16). Also the active layer thickness over the Yakutia region is consistent with the data from Beer et al. (2013) (Fig. 16).

## 8.2 Biogeochemistry

The modelled annual mean gross primary productivity is compared to estimates from Jung et al.  
835 (2009); Beer et al. (2010); Jung et al. (2011) in Fig. 17. Model and data are generally in good agreement, except over the Amazon where the model underestimates GPP. However, experiments using different climate forcings show a much better agreement between modelled and observed GPP over the Amazon basin (not shown). The simulated global annual GPP of 126 PgC yr<sup>-1</sup> is within the range of current estimates (Table 8).

840 The net global land carbon flux over the time period 1959-2010 is shown in Fig. 18. The model is able to reproduce some of the interannual variability in the net land carbon uptake, indicating that the sensitivities of net primary production and soil respiration to interannual climate variations are reasonably well represented in the model.

The modelled potential vegetation distribution for the present day is shown in Fig. 19, where  
845 it is compared to potential vegetation estimates from Ramankutty and Foley (1999). In general the model has the tendency to overestimate the areas covered by broadleaf trees in the tropics. The boreal needleleaf forest is well reproduced by the model, as are the grass and shrub coverages. Desert area is overestimated over Australia.



Global modelled vegetation carbon is 500 PgC, comparable to observations (Table 8). The geographic distribution of vegetation carbon content is in good agreement with data from Gibbs (2006) (Fig. 20).

The annual mean flux weighted discrimination is shown in Fig. 21. Mean discrimination for each plant functional type is also compared with observations from Kaplan et al. (2002) in Fig. 22. The model consistently tends to overestimate the discrimination for all PFTs.

Top meter soil carbon from the HSWD dataset (FAO/IIASA/ISRIC/ISSCAS/JRC, 2012) is well reproduced by the model, although the model underestimates carbon in peatland areas of the NH (Fig. 23). Top meter soil carbon is also compared to the NCSCD soil carbon dataset for the permafrost region (Hugelius et al., 2013b, a; Tarnocai et al., 2009) in Fig. 24.

Northern permafrost areas store large amounts of carbon at depths greater than 1 m. The NCSCD soil carbon dataset contains estimates of soil carbon down to a depth of 3 m in the permafrost regions. As expected, the model in the setup used in the presented simulations can not reproduce the large amounts of carbon stored in perennally frozen ground below 1 m because the inert permafrost carbon pool is not included (not shown). To get the carbon accumulation in permafrost a transient simulation over at least the last glacial cycle would be required. This is beyond the scope of this work, but will be discussed in a future paper. Similarly to the discussion on permafrost carbon, a proper estimate of peatland area and carbon content would also require a long transient simulation. However, an attempt has been made to estimate the peatland area and carbon using the equilibrium spinup described above. The estimated peatland area from this idealized approach is compared to NCSCD data (Hugelius et al., 2013b, a; Tarnocai et al., 2009) in Fig. 25.

Total modelled natural methane emissions for the present day are  $175 \text{ TgCH}_4 \text{ yr}^{-1}$ . From these,  $105 \text{ TgCH}_4 \text{ yr}^{-1}$  are from the tropics and  $70 \text{ TgCH}_4 \text{ yr}^{-1}$  from the extratropics. This values compare well with recent estimates of natural methane emissions (Table 8). The spatial distribution of annual methane emissions is shown in Fig. 26.

## 9 Conclusions

The PALADYN model presented here represents a new tool to model the land processes which are relevant for climate and the carbon cycle on time scales from years to millions of years.

PALADYN serves as a land surface scheme, soil model, dynamic vegetation model and land carbon cycle model. It also includes a representation of peatlands and soil carbon pools in frozen ground. Compared to other land surface models it has the great advantage that all components are consistently coupled.

PALADYN furthermore includes a representation of the processes related to changes in land-ice-shelf area, making it suitable for simulations over timescales where sea level and ice sheet areas can



not be considered as fixed boundary conditions. PALADYN is therefore designed to be included in Earth system models of intermediate complexity.

885 On a single CPU the model in its standard configuration (daily time step, 5x5 degree horizontal resolution and 5 soil layers) integrates one year in about 1 second (or equivalently about 100,000 model years per day), allowing to simulate e.g. one glacial cycle in one day. It is therefore indicated for paleoclimate applications or to perform large ensembles of simulations to explore uncertainties and sensitivities.

890 PALADYN in its offline version has been shown to perform well at reproducing a number of key characteristics of the present day land surface, soil, vegetation and land carbon cycle and is therefore ready to be included in Earth system models in a coupled setup.

## 10 Code availability

The model code is available on request from the authors.

### 895 Appendix A: Snow age factor

The snow age factor,  $f_{\text{age}}$ , is parameterized as a function of skin temperature and snowfall rate  $P_s$  as:

$$f_{\text{age}} = 1 - \frac{\ln\left(1 + f_{\text{age}}^T \frac{P_{s,c}}{P_s}\right)}{f_{\text{age}}^T \frac{P_{s,c}}{P_s}}, \quad (\text{A1})$$

$$f_{\text{age}}^T = e^{0.05(T_* - T_0)} + e^{(T_* - T_0)}. \quad (\text{A2})$$

900 The dependence of  $f_{\text{age}}$  on temperature and snowfall rate with  $P_{s,c} = 2 \times 10^{-5} \text{ kg m}^{-2} \text{ s}^{-1}$  is shown in Fig. A1.

### Appendix B: Soil thermal and hydraulic properties

Organic matter alters soil thermal and hydraulic properties substantially, in particular because of the much higher porosity of organic soils compared to mineral soils. The importance of accounting for organic matter in land-surface models has been discussed in e.g. Rinke et al. (2008); Lawrence and Slater (2008); Koven et al. (2009); Ekici et al. (2014); Chadburn et al. (2015). In PALADYN, the fraction of soil that is considered to be organic for the determination of the thermal and hydraulic soil properties is computed in each soil layer from the total carbon density following Lawrence and Slater (2008):

$$910 \quad f_{\text{org}} = \min\left(1, \frac{C_{\text{lit}} + C_{\text{fast}} + C_{\text{slow}}}{\rho_{\text{org}}^{\text{max}}}\right). \quad (\text{B1})$$

$\rho_{\text{org}}^{\text{max}} = 50 \text{ kgC m}^{-3}$  is the maximum soil carbon density, equivalent to a typical carbon density of peat.

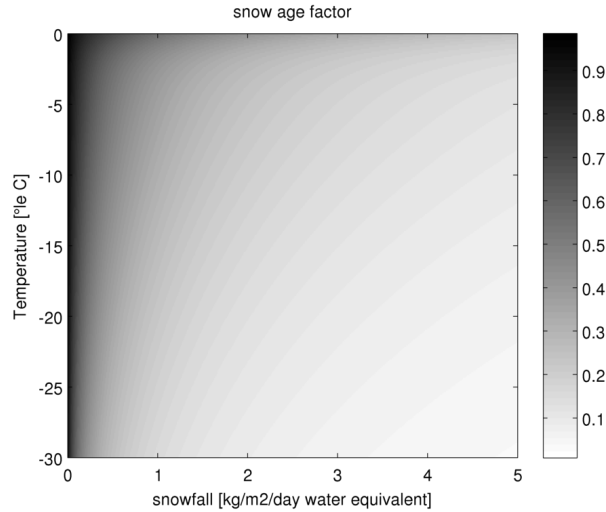


**Figure A1.** Snow age factor as a function of skin temperature and snowfall rate.

Soil thermal and hydraulic properties are simply taken to be a linear combination of mineral and organic values based on  $f_{\text{org}}$ . This linear combination is applied to porosity ( $\theta_{\text{sat}}$ ), dry thermal conductivity ( $\lambda_{\text{dry}}$ ), solid soil thermal conductivity ( $\lambda_{\text{s}}$ ), saturated hydraulic conductivity ( $k_{\text{sat}}$ ), saturation matric potential ( $\psi_{\text{sat}}$ ) and  $b$  parameter.

Mineral soil properties are computed from sand and clay fractions following Lawrence and Slater (2008), based on (Cosby et al., 1984; Farouki, 1981; Clapp and Hornberger, 1978). Sand and clay fractions are taken from either FAO/IIASA/ISRIC/ISSCAS/JRC (2012) or from Shangguan et al. (2014), with the former set as default. Sand and clay fractions are considered to be vertically uniform in each grid cell and constant in time.

Organic soil properties are also taken from Lawrence and Slater (2008), partly based on Letts et al. (2000); Farouki (1981).

### Appendix C: Photosynthesis

The maximum daily rate of net photosynthesis  $V_{\text{m}}$  is given by:

$$V_{\text{m}} = \frac{1}{a_{\text{C3/4}}} \frac{c_1}{c_2} [(2\theta_{\text{r}} - 1)s - (2\theta_{\text{r}}s - c_2)\sigma_{\text{m}}] APAR. \quad (\text{C1})$$

$$\sigma_{\text{m}} = \sqrt{1 - \frac{c_2 - s}{c_2 - \theta_{\text{r}} \cdot s}}, \quad (\text{C2})$$

where:

$$s = \frac{24}{d_{\text{h}}} a_{\text{C3/4}} \quad (\text{C3})$$



and  $d_h$  is the daylength in hours computed from orbital parameters.

All PALADYN PFTs follow the C3 photosynthetic pathway, except C4 grasses which follow the C4 pathway. For C3 plants  $c_1$  and  $c_2$  are given by:

$$c_1 = \alpha_{C3} f_{\text{temp}} C_{\text{mass}} \frac{p_i - \Gamma_{\star}}{p_i + \Gamma_{\star}}, \quad (\text{C4})$$

$$935 \quad c_2 = \frac{p_i - \Gamma_{\star}}{p_i + K_c(1 + [\text{O}_2]/K_o)}. \quad (\text{C5})$$

$\Gamma_{\star}$  is the  $\text{CO}_2$  compensation point:

$$\Gamma_{\star} = \frac{[\text{O}_2]}{2\tau}. \quad (\text{C6})$$

$K_c$ ,  $K_o$  and  $\tau$  are kinetic parameters whose temperature dependence is modeled using a Q10 relationship (Haxeltine and Prentice, 1996a).  $f_{\text{temp}}$  is a PFT specific temperature inhibition function  
940 (Sitch et al., 2003).

For C4 plants the same equations are used but with  $c_1$  and  $c_2$  given by:

$$c_1 = \alpha_{C4} f_{\text{temp}}, \quad (\text{C7})$$

$$c_2 = 1. \quad (\text{C8})$$

#### Appendix D: Aggregation of potential vegetation

945 In order to compare the modelled with the potential vegetation distribution of Ramankutty and Foley (1999), the potential vegetation needs to be aggregated to the plant functional types represented in PALADYN. We partly follow Blyth et al. (2011) and map vegetation classes of Ramankutty and Foley (1999) to the PALADYN PFTs as described in Table D1. The grass class in Table D1 is divided into C3 and C4 grasses based on the modelled grass type in each grid cell.



**Table D1.** Mapping of Ramankutty and Foley (1999) potential vegetation classes to PALADYN PFTs.

	BL	NL	grass	Shrubs	Bare soil
Tropical evergreen	0.9	0.0	0.0	0.0	0.1
Tropical deciduous	0.8	0.0	0.1	0.0	0.1
Temperate broadleaved evergreen	0.9	0.0	0.0	0.0	0.1
Temperate needleleaved evergreen	0.0	0.9	0.0	0.0	0.1
Temperate deciduous	0.9	0.0	0.0	0.0	0.1
Boreal evergreen	0.0	0.9	0.0	0.0	0.1
Boreal deciduous	0.0	0.8	0.1	0.0	0.1
Mixed evergreen/deciduous	0.1	0.7	0.0	0.1	0.1
Savanna	0.3	0.0	0.6	0.0	0.1
Grassland/steppe	0.0	0.0	0.9	0.0	0.1
Dense shrub	0.0	0.0	0.1	0.8	0.1
Open shrub	0.0	0.0	0.2	0.5	0.3
Tundra	0.0	0.0	0.35	0.35	0.3





950 *Acknowledgements.* The authors would like to thank Victor Brovkin and Daniela Dalmonech for discussions and Catherine Pringent for providing the GIEMS dataset. M. Willeit acknowledges support by the German Science Foundation DFG grant GA 1202/2-1.



## References

- Anderson, E.: A point energy and mass balance model of a snow cover, Tech. rep., 1976.
- 955 Arora, V. K. and Boer, G. J.: Fire as an interactive component of dynamic vegetation models, *Journal of Geophysical Research*, 110, 1–20, doi:10.1029/2005JG000042, 2005.
- Ball, J. T., Woodrow, I. E., and Berry, J. A.: A Model Predicting Stomatal Conductance and its Contribution to the Control of Photosynthesis under Different Environmental Conditions, in: *Progress in Photosynthesis Research*, pp. 221–224, doi:10.1007/978-94-017-0519-6\_48, 1987.
- 960 Baumgartner, A. and Reichel, E.: *Die Weltwasserbilanz: Niederschlag, Verdunstung u. Abfluss über Land u. Meer sowie auf d. Erde im Jahresdurchschnitt*, Elsevier Scientific Pub.Company, 1975.
- Beer, C., Reichstein, M., Tomelleri, E., Ciais, P., Jung, M., Carvalhais, N., Rödenbeck, C., Arain, M. A., Baldocchi, D., Bonan, G. B., Bondeau, A., Cescatti, A., Lasslop, G., Lindroth, A., Lomas, M., Luysaert, S., Margolis, H., Oleson, K. W., Rouspard, O., Veenendaal, E., Viovy, N., Williams, C., Woodward, F. I., and  
965 Papale, D.: Terrestrial gross carbon dioxide uptake: global distribution and covariation with climate., *Science* (New York, N.Y.), 329, 834–8, doi:10.1126/science.1184984, 2010.
- Beer, C., Fedorov, A. N., and Torgovkin, Y.: Permafrost temperature and active-layer thickness of Yakutia with 0.5-degree spatial resolution for model evaluation, *Earth System Science Data*, 5, 305–310, doi:10.5194/essd-5-305-2013, 2013.
- 970 Bereiter, B., Eggleston, S., Schmitt, J., Nehrbass-Ahles, C., Stocker, T. F., Fischer, H., Kipfstuhl, S., and Chappellaz, J.: Revision of the EPICA Dome C CO<sub>2</sub> record from 800 to 600 kyr before present, *Geophysical Research Letters*, 42, 542–549, doi:10.1002/2014GL061957, 2015.
- Beven, K. J. and Kirkby, M. J.: A physically based, variable contributing area model of basin hydrology / Un modèle à base physique de zone d'appel variable de l'hydrologie du bassin versant, *Hydrological Sciences  
975 Bulletin*, 24, 43–69, doi:10.1080/02626667909491834, 1979.
- Bloom, A. A., Palmer, P. I., Fraser, A., Reay, D. S., and Frankenberg, C.: Large-Scale Controls of Methanogenesis Inferred from Methane and Gravity Spaceborne Data, *Science*, 327, 322–325, doi:10.1126/science.1175176, 2010.
- Blyth, E., Clark, D. B., Ellis, R., Huntingford, C., Los, S., Pryor, M., Best, M., and Sitch, S.: A comprehensive  
980 set of benchmark tests for a land surface model of simultaneous fluxes of water and carbon at both the global and seasonal scale, *Geoscientific Model Development*, 4, 255–269, doi:10.5194/gmd-4-255-2011, 2011.
- Bousquet, P., Ciais, P., Miller, J. B., Dlugokencky, E. J., Hauglustaine, D. A., Prigent, C., Van der Werf, G. R., Peylin, P., Brunke, E.-G., Carouge, C., Langenfelds, R. L., Lathière, J., Papa, F., Ramonet, M., Schmidt, M., Steele, L. P., Tyler, S. C., and White, J.: Contribution of anthropogenic and natural sources to atmospheric  
985 methane variability., *Nature*, 443, 439–43, doi:10.1038/nature05132, 2006.
- Braakhekke, M. C., Beer, C., Hoosbeek, M. R., Reichstein, M., Kruijt, B., Schrumph, M., and Kabat, P.: SOMPROF: A vertically explicit soil organic matter model, *Ecological Modelling*, 222, 1712–1730, doi:10.1016/j.ecolmodel.2011.02.015, 2011.
- Brovkin, V., Ganopolski, A., and Svirezhev, Y.: A continuous climate-vegetation classification for use in  
990 climate-biosphere studies, *Ecological Modelling*, 101, 251–261, 1997.



- Brovkin, V., Bendtsen, J., Claussen, M., Ganopolski, A., Kubatzki, C., Petoukhov, V., and Andreev, A.: Carbon cycle, vegetation, and climate dynamics in the Holocene: Experiments with the CLIMBER-2 model, *Global Biogeochemical Cycles*, 16, 86–1–86–20, doi:10.1029/2001GB001662, 2002.
- 995 Brown, J., Ferrians, O., Heginbottom, J. A., and Melnikov, E.: Circum-Arctic Map of Permafrost and Ground-  
Ice Conditions, 2014.
- Campbell, G. S. and Norman, J. M.: The description and measurement of plant canopy structure, in: *Plant Canopies: Their Growth, Form and Function*, edited by Russel, G., Marshall, B., and Jarvis, P. G., pp. 1–19, Cambridge University Press, Cambridge, 1989.
- 1000 Chadburn, S., Burke, E., Essery, R., Boike, J., Langer, M., Heikenfeld, M., Cox, P., and Friedlingstein, P.: An improved representation of physical permafrost dynamics in the JULES land-surface model, *Geoscientific Model Development*, 8, 1493–1508, doi:10.5194/gmd-8-1493-2015, 2015.
- Clapp, R. B. and Hornberger, G. M.: Empirical equations for some soil hydraulic properties, *Water Resources Research*, 14, 601–604, doi:10.1029/WR014i004p00601, 1978.
- 1005 Clark, D. B., Mercado, L. M., Sitch, S., Jones, C. D., Gedney, N., Best, M. J., Pryor, M., Rooney, G. G., Essery, R. L. H., Blyth, E., Boucher, O., Harding, R. J., Huntingford, C., and Cox, P. M.: The Joint UK Land Environment Simulator (JULES), model description – Part 2: Carbon fluxes and vegetation dynamics, *Geoscientific Model Development*, 4, 701–722, doi:10.5194/gmd-4-701-2011, 2011.
- Claussen, M.: On coupling global biome models with climate models, *Clim.Res.*, 4, 203–221, doi:10.3354/cr004203, 1994.
- 1010 Claussen, M., Mysak, L., Weaver, A., Crucifix, M., Fichetef, T., Loutre, M. F., Weber, S., Alcamo, J., Alexeev, V., Berger, A., Calov, R., Ganopolski, A., Goosse, H., Lohmann, G., Lunkeit, F., Mokhov, I., Petoukhov, V., Stone, P., and Wang, Z.: Earth system models of intermediate complexity: Closing the gap in the spectrum of climate system models, *Climate Dynamics*, 18, 579–586, doi:10.1007/s00382-001-0200-1, 2002.
- 1015 Clymo, R. S.: The Limits to Peat Bog Growth, *Philosophical Transactions of the Royal Society B: Biological Sciences*, 303, 605–654, doi:10.1098/rstb.1984.0002, 1984.
- Collatz, G., Ball, J., Grivet, C., and Berry, J. A.: Physiological and environmental regulation of stomatal conductance, photosynthesis and transpiration: a model that includes a laminar boundary layer, *Agricultural and Forest Meteorology*, 54, 107–136, doi:10.1016/0168-1923(91)90002-8, 1991.
- 1020 Cosby, B. J., Hornberger, G. M., Clapp, R. B., and Ginn, T. R.: A Statistical Exploration of the Relationships of Soil Moisture Characteristics to the Physical Properties of Soils, *Water Resources Research*, 20, 682–690, doi:10.1029/WR020i006p00682, 1984.
- Cox, P. M.: Description of the " TRIFFID " Dynamic Global Vegetation Model, 2001.
- 1025 Cox, P. M., Betts, R. A., Bunton, C. B., Essery, R. L. H., Rowntree, P. R., and Smith, J.: The impact of new land surface physics on the GCM simulation of climate and climate sensitivity, *Climate Dynamics*, 15, 183–203, doi:10.1007/s003820050276, 1999.
- Dale, V. H., Joyce, L. A., McNulty, S., Neilson, R. P., Ayres, M. P., Flannigan, M. D., Hanson, P. H., Irland, L. C., Lugo, A. E., Peterson, C. J., Simberloff, D., Swanson, F. J., Stocks, B. J., and Wotton, M. B.: Climate change and forest disturbances, *BioScience*, 51, 723–734, doi:10.1641/0006-3568(2001)051[0723:CCAFD]2.0.CO;2, 2001.



- 1030 Dazlich, D. A. and Los, S. O.: ISLSCP II Monthly Snow-Free Albedo, 1982-1998, and Background Soil Reflectance., in: ISLSCP Initiative II Collection. Data set., edited by Hall, F. G., Collatz, G., Meeson, B., Los, S., Brown de Colstoun, E., and Landis, D., Available on-line [<http://daac.ornl.gov/>] from Oak Ridge National Laboratory Distributed Active Archive Center, Oak Ridge, Tennessee, U.S.A., doi:10.3334/ORNLDAAC/956, 2009.
- 1035 Dearing, J. W.: Efficient prediction of ground surface temperature and moisture, with inclusion of a layer of vegetation, *Journal of Geophysical Research*, 83, 1889, doi:10.1029/JC083iC04p01889, 1978.
- Dee, D. P., Uppala, S. M., Simmons, A. J., Berrisford, P., Poli, P., Kobayashi, S., Andrae, U., Balmaseda, M. A., Balsamo, G., Bauer, P., Bechtold, P., Beljaars, A. C. M., van de Berg, L., Bidlot, J., Bormann, N., Delsol, C., Dragani, R., Fuentes, M., Geer, A. J., Haimberger, L., Healy, S. B., Hersbach, H., Hólm, E. V., Isaksen, L., Kållberg, P., Köhler, M., Matricardi, M., McNally, A. P., Monge-Sanz, B. M., Morcrette, J.-J., Park, B.-K., Peubey, C., de Rosnay, P., Tavolato, C., Thépaut, J.-N., and Vitart, F.: The ERA-Interim reanalysis: configuration and performance of the data assimilation system, *Quarterly Journal of the Royal Meteorological Society*, 137, 553–597, doi:10.1002/qj.828, 2011.
- 1040 Dickinson, R., Henderson-Sellers, A., Kennedy, P., and Wilson, M.: Biosphere-Atmosphere Transfer Scheme ( BATS ) for the NCAR Community Climate Model, NCAR Technical Note NCAR/TN-275+STR, doi:10.5065/D6668B58, 1986.
- Dirmeyer, P. A., Gao, X., Zhao, M., Guo, Z., Oki, T., and Hanasaki, N.: GSWP-2: Multimodel Analysis and Implications for Our Perception of the Land Surface, *Bulletin of the American Meteorological Society*, 87, 1381–1397, doi:10.1175/BAMS-87-10-1381, 2006.
- 1050 Ekici, A., Beer, C., Hagemann, S., Boike, J., Langer, M., and Hauck, C.: Simulating high-latitude permafrost regions by the JSBACH terrestrial ecosystem model, *Geoscientific Model Development*, 7, 631–647, doi:10.5194/gmd-7-631-2014, 2014.
- FAO/IIASA/ISRIC/ISSCAS/JRC: Harmonized World Soil Database (version 1.2), 2012.
- Farouki, O. T.: Thermal properties of soils, Special Report 81–1. Cold Regions Research and Engineering Laboratory (CRREL), Hanover, NH., 1981.
- 1055 Farquhar, G. D., Caemmerer, S., and Berry, J. A.: A biochemical model of photosynthetic CO<sub>2</sub> assimilation in leaves of C<sub>3</sub> species, *Planta*, 149, 78–90, doi:10.1007/BF00386231.
- Fekete, B. M., Vörösmarty, C. J., and Grabs, W.: High-resolution fields of global runoff combining observed river discharge and simulated water balances, *Global Biogeochemical Cycles*, 16, 15 1—6, doi:10.1029/1999GB001254, 2002.
- 1060 Foley, J. A.: Net primary productivity in the terrestrial biosphere: The application of a global model, *Journal of Geophysical Research*, 99, 20 773, doi:10.1029/94JD01832, 1994.
- Foley, J. A., Prentice, I. C., Ramankutty, N., Levis, S., Pollard, D., Sitch, S., and Haxeltine, A.: An integrated biosphere model of land surface processes, terrestrial carbon balance, and vegetation dynamics, *Global Biogeochemical Cycles*, 10, 603–628, doi:10.1029/96GB02692, 1996.
- 1065 Friend, A. D., Stevens, A., Knox, R., and Cannell, M.: A process-based, terrestrial biosphere model of ecosystem dynamics (Hybrid v3.0), *Ecological Modelling*, 95, 249–287, doi:10.1016/S0304-3800(96)00034-8, 1997.



- Ganopolski, A., Petoukhov, V., Rahmstorf, S., Brovkin, V., Claussen, M., Eliseev, A., and Kubatzki, C.:  
1070 CLIMBER-2: a climate system model of intermediate complexity. Part II: model sensitivity, *Climate Dy-*  
*namics*, 17, 735–751, doi:10.1007/s003820000144, 2001.
- Gardner, A. S. and Sharp, M. J.: A review of snow and ice albedo and the development of a new  
physically based broadband albedo parameterization, *Journal of Geophysical Research*, 115, F01 009,  
doi:10.1029/2009JF001444, 2010.
- 1075 Garratt, J.: *The Atmospheric Boundary Layer*, Cambridge University Press, 1994.
- Gibbs, H. K.: Olson's Major World Ecosystem Complexes Ranked by Carbon in Live Veg-  
etation: An Updated Database Using the GLC2000 Land Cover Product (available at  
<http://cdiac.ornl.gov/epubs/ndp/ndp017/ndp017b.html>), doi:10.3334/CDIAC/lue.ndp017.2006, 2006.
- Gruber, S.: Derivation and analysis of a high-resolution estimate of global permafrost zonation, *Cryosphere*, 6,  
1080 221–233, doi:10.5194/tc-6-221-2012, 2012.
- Haxeltine, A. and Prentice, I. C.: A general model for the light-use efficiency of primary production, *Functional*  
*Ecology*, 10, 551–561, 1996a.
- Haxeltine, A. and Prentice, I. C.: BIOME3: An equilibrium terrestrial biosphere model based on ecophysiological  
constraints, resource availability, and competition among plant functional types, *Global Biogeochemical*  
1085 *Cycles*, 10, 693–709, doi:10.1029/96GB02344, 1996b.
- Henderson-Sellers, A.: Continental vegetation as a dynamic component of a global climate model: a preliminary  
assessment, *Climatic Change*, 23, 337–377, doi:10.1007/BF01091622, 1993.
- Houldcroft, C. J., Grey, W. M. F., Barnsley, M., Taylor, C. M., Los, S. O., and North, P. R. J.: New Vegetation  
Albedo Parameters and Global Fields of Soil Background Albedo Derived from MODIS for Use in a Climate  
1090 *Model*, *Journal of Hydrometeorology*, 10, 183–198, doi:10.1175/2008JHM1021.1, 2009.
- Hugelius, G., Bockheim, J. G., Camill, P., Elberling, B., Grosse, G., Harden, J. W., Johnson, K., Jorgenson, T.,  
Koven, C. D., Kuhry, P., Michaelson, G., Mishra, U., Palmtag, J., Ping, C.-L., O'Donnell, J., Schirrmeister,  
L., Schuur, E. A. G., Sheng, Y., Smith, L. C., Strauss, J., and Yu, Z.: A new data set for estimating organic  
carbon storage to 3 m depth in soils of the northern circumpolar permafrost region, *Earth System Science*  
1095 *Data*, 5, 393–402, doi:10.5194/essd-5-393-2013, 2013a.
- Hugelius, G., Tarnocai, C., Broll, G., Canadell, J. G., Kuhry, P., and Swanson, D. K.: The Northern Circumpolar  
Soil Carbon Database: spatially distributed datasets of soil coverage and soil carbon storage in the northern  
permafrost regions, *Earth System Science Data*, 5, 3–13, doi:10.5194/essd-5-3-2013, 2013b.
- Hugelius, G., Strauss, J., Zubrzycki, S., Harden, J. W., Schuur, E. A. G., Ping, C.-L., Schirrmeister, L., Grosse,  
1100 G., Michaelson, G. J., Koven, C. D., O'Donnell, J. A., Elberling, B., Mishra, U., Camill, P., Yu, Z., Palmtag,  
J., and Kuhry, P.: Estimated stocks of circumpolar permafrost carbon with quantified uncertainty ranges and  
identified data gaps, *Biogeosciences*, 11, 6573–6593, doi:10.5194/bg-11-6573-2014, 2014.
- Ito, A.: A historical meta-analysis of global terrestrial net primary productivity: are estimates converging?,  
*Global Change Biology*, 17, 3161–3175, doi:10.1111/j.1365-2486.2011.02450.x, 2011.
- 1105 Jarvis, P. G.: The Interpretation of the Variations in Leaf Water Potential and Stomatal Conductance Found in  
Canopies in the Field, *Philosophical Transactions of the Royal Society B: Biological Sciences*, 273, 593–610,  
doi:10.1098/rstb.1976.0035, 1976.



- Jin, M. and Liang, S.: An Improved Land Surface Emissivity Parameter for Land Surface Models Using Global Remote Sensing Observations, *Journal of Climate*, 19, 2867–2881, doi:10.1175/JCLI3720.1, 2006.
- 1110 Jordan, R.: A one-dimensional temperature model for a snow cover, 1991.
- Jung, M., Reichstein, M., and Bondeau, A.: Towards global empirical upscaling of FLUXNET eddy covariance observations: validation of a model tree ensemble approach using a biosphere model, *Biogeosciences Discussions*, 6, 5271–5304, doi:10.5194/bgd-6-5271-2009, 2009.
- Jung, M., Reichstein, M., Margolis, H. A., Cescatti, A., Richardson, A. D., Arain, M. A., Arneth, A., Bernhofer, C., Bonal, D., Chen, J., Gianelle, D., Gobron, N., Kiely, G., Kutsch, W., Lasslop, G., Law, B. E., Lindroth, A., Merbold, L., Montagnani, L., Moors, E. J., Papale, D., Sottocornola, M., Vaccari, F., and Williams, C.: Global patterns of land-atmosphere fluxes of carbon dioxide, latent heat, and sensible heat derived from eddy covariance, satellite, and meteorological observations, *Journal of Geophysical Research: Biogeosciences*, 116, 2–4, doi:10.1029/2010JG001566, 2011.
- 1115
- 1120 Kaplan, J. O., Prentice, I. C., and Buchmann, N.: The stable carbon isotope composition of the terrestrial biosphere: Modeling at scales from the leaf to the globe, *Global Biogeochemical Cycles*, 16, 8–1–8–11, doi:10.1029/2001GB001403, 2002.
- Kattge, J., Díaz, S., Lavorel, S., Prentice, I. C., Leadley, P., Bönsch, G., Garnier, E., Westoby, M., Reich, P. B., Wright, I. J., Cornelissen, J. H. C., Violle, C., Harrison, S. P., Van Bodegom, P. M., Reichstein, M., Enquist, B. J., Soudzilovskaia, N. A., Ackerly, D. D., Anand, M., Atkin, O., Bahn, M., Baker, T. R., Baldocchi, D., Bekker, R., Blanco, C. C., Blonder, B., Bond, W. J., Bradstock, R., Bunker, D. E., Casanoves, F., Cavender-Bares, J., Chambers, J. Q., Chapin, F. S., Chave, J., Coomes, D., Cornwell, W. K., Craine, J. M., Dobrin, B. H., Duarte, L., Durka, W., Elser, J., Esser, G., Estiarte, M., Fagan, W. F., Fang, J., Fernández-Méndez, F., Fidelis, A., Finegan, B., Flores, O., Ford, H., Frank, D., Freschet, G. T., Fyllas, N. M., Gallagher, R. V., Green, W. A., Gutierrez, A. G., Hickler, T., Higgins, S. I., Hodgson, J. G., Jalili, A., Jansen, S., Joly, C. A., Kerkhoff, A. J., Kirkup, D., Kitajima, K., Kleyer, M., Klotz, S., Knops, J. M. H., Kramer, K., Kühn, I., Kurokawa, H., Laughlin, D., Lee, T. D., Leishman, M., Lens, F., Lenz, T., Lewis, S. L., Lloyd, J., Llusià, J., Louault, F., Ma, S., Mahecha, M. D., Manning, P., Massad, T., Medlyn, B. E., Messier, J., Moles, A. T., Müller, S. C., Nadrowski, K., Naeem, S., Niinemets, Ü., Nöllert, S., Nüske, A., Ogaya, R., Oleksyn, J., Onipchenko, V. G., Onoda, Y., Ordoñez, J., Overbeck, G., Ozinga, W. A., Patiño, S., Paula, S., Pausas, J. G., Peñuelas, J., Phillips, O. L., Pillar, V., Poorter, H., Poorter, L., Poschlod, P., Prinzing, A., Proulx, R., Rammig, A., Reinsch, S., Reu, B., Sack, L., Salgado-Negret, B., Sardans, J., Shiodera, S., Shipley, B., Siefert, A., Sosinski, E., Soussana, J. F., Swaine, E., Swenson, N., Thompson, K., Thornton, P., Waldram, M., Weiher, E., White, M., White, S., Wright, S. J., Yguel, B., Zaehle, S., Zanne, A. E., and Wirth, C.: TRY - a global database of plant traits, *Global Change Biology*, 17, 2905–2935, doi:10.1111/j.1365-2486.2011.02451.x, 2011.
- 1130
- 1135
- 1140
- Keeling, C. D., Bacastow, R. B., Bainbridge, A. E., Ekdahl Jr., C. . A., Guenther, P. R., Waterman, L. S., and Chin, J. F. S.: Atmospheric carbon dioxide variations at Mauna Loa Observatory, Hawaii, *Tellus A*, 28, 538–551, doi:10.3402/tellusa.v28i6.11322, 1976.
- Khvorostyanov, D. V., Krinner, G., Ciais, P., Heimann, M., and Zimov, S. A.: Vulnerability of permafrost carbon to global warming. Part I: model description and role of heat generated by organic matter decomposition, *Tellus B*, 60, 250–264, doi:10.1111/j.1600-0889.2007.00333.x, 2008.
- 1145



- Kleinen, T., Brovkin, V., and Schuldt, R. J.: A dynamic model of wetland extent and peat accumulation: results for the Holocene, *Biogeosciences*, 9, 235–248, doi:10.5194/bg-9-235-2012, 2012.
- Kojima, K.: Densification of seasonal snow cover, 1967.
- 1150 Koven, C., Friedlingstein, P., Ciais, P., Khvorostyanov, D., Krinner, G., and Tarnocai, C.: On the formation of high-latitude soil carbon stocks: Effects of cryoturbation and insulation by organic matter in a land surface model, *Geophysical Research Letters*, 36, L21 501, doi:10.1029/2009GL040150, 2009.
- Koven, C. D., Riley, W. J., Subin, Z. M., Tang, J. Y., Torn, M. S., Collins, W. D., Bonan, G. B., Lawrence, D. M., and Swenson, S. C.: The effect of vertically resolved soil biogeochemistry and alternate soil C and N models on C dynamics of CLM4, *Biogeosciences*, 10, 7109–7131, doi:10.5194/bg-10-7109-2013, 2013.
- 1155 Krinner, G., Viovy, N., de Noblet-Ducoudré, N., Ogée, J., Polcher, J., Friedlingstein, P., Ciais, P., Sitch, S., and Prentice, I. C.: A dynamic global vegetation model for studies of the coupled atmosphere-biosphere system, *Global Biogeochemical Cycles*, 19, n/a–n/a, doi:10.1029/2003GB002199, 2005.
- Lawrence, D. M. and Slater, A. G.: Incorporating organic soil into a global climate model, *Climate Dynamics*, 1160 30, 145–160, doi:10.1007/s00382-007-0278-1, 2008.
- Lee, T. J. and Pielke, R. A.: Estimating the Soil Surface Specific Humidity, doi:10.1175/1520-0450(1992)031<0480:ETSSSH>2.0.CO;2, 1992.
- Letts, M. G., Roulet, N. T., Comer, N. T., Skarupa, M. R., and Verseghy, D. L.: Parametrization of peatland hydraulic properties for the Canadian land surface scheme, *Atmosphere-Ocean*, 38, 141–160, 1165 doi:10.1080/07055900.2000.9649643, 2000.
- Leuning, R.: A critical appraisal of a combined stomatal-photosynthesis model for C3 plants, *Plant, Cell and Environment*, 18, 339–355, doi:10.1111/j.1365-3040.1995.tb00370.x, 1995.
- Lin, Y.-S., Medlyn, B. E., Duursma, R. A., Prentice, I. C., Wang, H., Baig, S., Eamus, D., de Dios, V., Mitchell, P., Ellsworth, D. S., de Beeck, M. O., Wallin, G., Uddling, J., Tarvainen, L., Linderson, M.-L., Cernusak, 1170 L. A., Nippert, J. B., Oecheltree, T. W., Tissue, D. T., Martin-StPaul, N. K., Rogers, A., Warren, J. M., De Angelis, P., Hikosaka, K., Han, Q., Onoda, Y., Gimeno, T. E., Barton, C. V. M., Bennie, J., Bonal, D., Bosc, A., Löw, M., Macinins-Ng, C., Rey, A., Rowland, L., Setterfield, S. A., Tausz-Posch, S., Zaragoza-Castells, J., Broadmeadow, M. S. J., Drake, J. E., Freeman, M., Ghannoum, O., Hutley, L., Kelly, J. W., Kikuzawa, K., Kolari, P., Koyama, K., Limousin, J.-M., Meir, P., Lola da Costa, A. C., Mikkelsen, T. N., Salinas, N., 1175 Sun, W., and Wingate, L.: Optimal stomatal behaviour around the world, *Nature Climate Change*, pp. 1–14, doi:10.1038/nclimate2550, 2015.
- Liu, Y., Dorigo, W., Parinussa, R., de Jeu, R., Wagner, W., McCabe, M., Evans, J., and van Dijk, A.: Trend-preserving blending of passive and active microwave soil moisture retrievals, *Remote Sensing of Environment*, 123, 280–297, doi:10.1016/j.rse.2012.03.014, 2012.
- 1180 Lloyd, J. and Farquhar, G. D.:  $^{13}\text{C}$  discrimination during  $\text{CO}_2$  assimilation by the terrestrial biosphere, *Oecologia*, 99, 201–215, doi:10.1007/BF00627732, 1994.
- Lloyd, J. and Taylor, J. A.: On the temperature dependence of soil respiration, *Functional ecology*, 8, 315–323, doi:papers2://publication/uuid/EE45B025-598C-4D7C-A259-FA6366F27CAB, 1994.
- Luoju, K., Pulliainen, J., and Consortium, G.: Global Snow Monitoring for Climate Research: Snow Water 1185 Equivalent, <http://www.globsnow.info/swe/>, 2013.





- Mahfouf, J. F. and Noilhan, J.: Comparative Study of Various Formulations of Evaporations from Bare Soil Using In Situ Data, *Journal of Applied Meteorology*, 30, 1354–1365, doi:10.1175/1520-0450(1991)030<1354:CSOVFO>2.0.CO;2, 1991.
- 1190 Malmer, N. and Wallén, B.: Input rates, decay losses and accumulation rates of carbon in bogs during the last millennium: internal processes and environmental changes, *The Holocene*, 14, 111–117, doi:10.1191/0959683604hl693rp, 2004.
- Manabe, S.: Climate and the ocean circulation I. The atmosphere and the hydrology of the Earth's surface, *Monthly Weather Review*, 97, 739–774, doi:10.1175/1520-0493(1969)097<0739:CATOC>2.3.CO;2, 1969.
- 1195 Medlyn, B. E., Duursma, R. A., Eamus, D., Ellsworth, D. S., Prentice, I. C., Barton, C. V. M., Crous, K. Y., De Angelis, P., Freeman, M., and Wingate, L.: Reconciling the optimal and empirical approaches to modelling stomatal conductance, *Global Change Biology*, 17, 2134–2144, doi:10.1111/j.1365-2486.2010.02375.x, 2011.
- Melillo, J. M., McGuire, A. D., Kicklighter, D. W., Moore, B., Vorosmarty, C. J., and Schloss, A. L.: Global climate change and terrestrial net primary production, *Nature*, 363, 234–240, doi:10.1038/363234a0, 1993.
- 1200 Milly, P. C. D. and Shmakin, A. B.: Global Modeling of Land Water and Energy Balances. Part I: The Land Dynamics (LaD) Model, *Journal of Hydrometeorology*, 3, 283–299, doi:10.1175/1525-7541(2002)003<0283:GMOLWA>2.0.CO;2, 2002.
- 1205 Moody, E. G., King, M. D., Schaaf, C. B., Hall, D. K., and Platnick, S.: Northern Hemisphere five-year average (2000–2004) spectral albedos of surfaces in the presence of snow: Statistics computed from Terra MODIS land products, *Remote Sensing of Environment*, 111, 337–345, doi:10.1016/j.rse.2007.03.026, 2007.
- Mueller, B., Hirschi, M., Jimenez, C., Ciais, P., Dirmeyer, P. A., Dolman, A. J., Fisher, J. B., Jung, M., Ludwig, F., Maignan, F., Miralles, D. G., McCabe, M. F., Reichstein, M., Sheffield, J., Wang, K., Wood, E. F., Zhang, Y., and Seneviratne, S. I.: Benchmark products for land evapotranspiration: LandFlux-EVAL multi-data set synthesis, *Hydrology and Earth System Sciences*, 17, 3707–3720, doi:10.5194/hess-17-3707-2013, 2013.
- 1210 Neilson, R. P.: A Model for Predicting Continental-Scale Vegetation Distribution and Water Balance, *Ecological Applications*, 5, 362, doi:10.2307/1942028, 1995.
- Niu, G.-Y. and Yang, Z.-L.: Effects of Frozen Soil on Snowmelt Runoff and Soil Water Storage at a Continental Scale, *Journal of Hydrometeorology*, 7, 937–952, doi:10.1175/JHM538.1, 2006.
- 1215 Niu, G.-Y., Yang, Z.-L., Dickinson, R. E., and Gulden, L. E.: A simple TOPMODEL-based runoff parameterization (SIMTOP) for use in global climate models, *Journal of Geophysical Research*, 110, D21 106, doi:10.1029/2005JD006111, 2005.
- Oleson, K., Bonan, G., Levis, S., Thornton, P., Vertenstein, M., and Yang, Z.: Technical Description of the Community Land Model (CLM), NCAR Technical Note, 461, 1–174, doi:10.5065/D6N877R0, 2004.
- 1220 Oleson, K. W., Lawrence, D. M., Bonan, G. B., Drewniak, B., Huang, M., Charles, D., Levis, S., Li, F., Riley, W. J., Zachary, M., Swenson, S. C., Thornton, P. E., Bozbiyik, A., Fisher, R., Heald, C. L., Kluzek, E., Lamarque, F., Lawrence, P. J., Leung, L. R., Muszala, S., Ricciuto, D. M., Sacks, W., Sun, Y., Tang, J., and Yang, Z.-L.: Technical Description of version 4.5 of the Community Land Model (CLM) Coordinating, Tech. Rep. July, 2013.
- 1225 Otto, J., Raddatz, T., and Claussen, M.: Strength of forest-albedo feedback in mid-Holocene climate simulations, *Climate of the Past*, 7, 1027–1039, doi:10.5194/cp-7-1027-2011, 2011.





- Papa, F., Prigent, C., Aires, F., Jimenez, C., Rossow, W. B., and Matthews, E.: Interannual variability of surface water extent at the global scale, 1993–2004, *Journal of Geophysical Research*, 115, D12 111, doi:10.1029/2009JD012674, 2010.
- 1230 Petoukhov, V., Ganopolski, A., Brovkin, V., Claussen, M., Eliseev, A., Kubatzki, C., and Rahmstorf, S.: CLIMBER-2: a climate system model of intermediate complexity. Part I: model description and performance for present climate, *Climate Dynamics*, 16, 1–17, doi:10.1007/PL00007919, 2000.
- Pitman, A. J.: The evolution of, and revolution in, land surface schemes designed for climate models, *International Journal of Climatology*, 23, 479–510, doi:10.1002/joc.893, 2003.
- 1235 Pitman, A. J., Liang, Z. L., Cogley, J. G., and Henderson-Sellers, A.: Description of bare essentials of surface transfer for the Bureau of Meteorological Research Centre AGCM, Tech. rep., 1991.
- Porporato, A., D’Odorico, P., Laio, F., and Rodriguez-Iturbe, I.: Hydrologic controls on soil carbon and nitrogen cycles. I. Modeling scheme, *Advances in Water Resources*, 26, 45–58, doi:10.1016/S0309-1708(02)00094-5, 2003.
- 1240 Prentice, I., Farquhar, G., Fasham, M., Goulden, M., Heimann, M., Jaramillo, W., Kheshgi, H., Le Quééré, C., Scholes, R., Wallace, D., and Al., E.: The Carbon Cycle and Atmospheric Carbon Dioxide Content, in: *Climate Change 2001. The Science Basis. Contribution of Working Group I to the Third Assessment Report of the Intergovernmental Panel on Climate Change*, edited by Houghton, J., Ding, Y., and Al., E., Cambridge University Press, Cambridge, United Kingdom, 2001.
- 1245 Prentice, I. C., Cramer, W., Harrison, S. P., Leemans, R., Robert, A., Solomon, A. M., and Vallgatan, O.: A global biome model based on plant physiology and dominance, soil properties and climate, *Journal of Biogeography*, 19, 117–134, 1992.
- Priigent, C., Papa, F., Aires, F., Rossow, W. B., and Matthews, E.: Global inundation dynamics inferred from multiple satellite observations, 1993–2000, *Journal of Geophysical Research*, 112, D12 107, doi:10.1029/2006JD007847, 2007.
- 1250 R. S. Clymo, J. Turunen, K. T.: Carbon Accumulation in Peatland, *Oikos*, 81, 368–388, 1998.
- Raich, J. W., Rastetter, E. B., Melillo, J. M., Kicklighter, D. W., Steudler, P. A., Peterson, B. J., Grace, A. L., III, B. M., and Vorosmarty, C. J.: Potential Net Primary Productivity in South America: Application of a Global Model, *Ecological Applications*, 1, 399, doi:10.2307/1941899, 1991.
- 1255 Ramankutty, N. and Foley, J. A.: Estimating historical changes in global land cover: Croplands from 1700 to 1992, *Global Biogeochemical Cycles*, 13, 997–1027, doi:10.1029/1999GB900046, 1999.
- Reick, C. H., Raddatz, T., Brovkin, V., and Gayler, V.: Representation of natural and anthropogenic land cover change in MPI-ESM, *Journal of Advances in Modeling Earth Systems*, 5, n/a–n/a, doi:10.1002/jame.20022, 2013.
- 1260 Riche, F. and Schneebeli, M.: Thermal conductivity of snow measured by three independent methods and anisotropy considerations, *Cryosphere*, 7, 217–227, doi:10.5194/tc-7-217-2013, 2013.
- Rinke, A., Kuhry, P., Dethloff, K., and Rinke P. Kuhry, and K. Dethloff, A.: Importance of a soil organic layer for Arctic climate: A sensitivity study with an Arctic RCM, *Geophysical Research Letters*, 35, L13 709, doi:10.1029/2008GL034052, 2008.
- 1265 Robinson, A. and Perrette, M.: NCIO 1.0: a simple Fortran NetCDF interface, *Geoscientific Model Development*, 8, 1877–1883, doi:10.5194/gmd-8-1877-2015, 2015.



- Running, S. W. and Coughlan, J. C.: A general model of forest ecosystem processes for regional applications I. Hydrologic balance, canopy gas exchange and primary production processes, *Ecological Modelling*, 42, 125–154, doi:10.1016/0304-3800(88)90112-3, 1988.
- Running, S. W. and Gower, S. T.: FOREST-BGC, A general model of forest ecosystem processes for regional applications. II. Dynamic carbon allocation and nitrogen budgets., *Tree physiology*, 9, 147–160, doi:citeulike-article-id:2850231, 1991.
- 1270 Sato, H., Itoh, A., and Kohyama, T.: SEIB-DGVM: A new Dynamic Global Vegetation Model using a spatially explicit individual-based approach, *Ecological Modelling*, 200, 279–307, doi:10.1016/j.ecolmodel.2006.09.006, 2007.
- 1275 Schaaf, C. and Wang, Z.: MCD43C3 MODIS/Terra+Aqua BRDF/Albedo Albedo Daily L3 Global 0.05Deg CMG V006, doi:http://doi.org/10.5067/MODIS/MCD43C3.006, 2015.
- Schaphoff, S., Heyder, U., Ostberg, S., Gerten, D., Heinke, J., and Lucht, W.: Contribution of permafrost soils to the global carbon budget, *Environmental Research Letters*, 8, 014 026, doi:10.1088/1748-9326/8/1/014026, 2013.
- 1280 Schneider, U., Becker, A., Finger, P., Meyer-Christoffer, A., Ziese, M., and Rudolf, B.: GPCC's new land surface precipitation climatology based on quality-controlled in situ data and its role in quantifying the global water cycle, *Theoretical and Applied Climatology*, 115, 15–40, doi:10.1007/s00704-013-0860-x, 2014.
- Schuur, E. a. G., McGuire, a. D., Schädel, C., Grosse, G., Harden, J. W., Hayes, D. J., Hugelius, G., Koven, C. D., Kuhry, P., Lawrence, D. M., Natali, S. M., Olefeldt, D., Romanovsky, V. E., Schaefer, K., Turetsky, M. R., Treat, C. C., and Vonk, J. E.: Climate change and the permafrost carbon feedback, *Nature*, 520, 171–179, doi:10.1038/nature14338, 2015.
- 1285 Sellers, P. J., Mintz, Y., Sud, Y. C., and Dalcher, A.: A Simple Biosphere Model (SIB) for Use within General Circulation Models, *Journal of the Atmospheric Sciences*, 43, 505–531, doi:10.1175/1520-0469(1986)043<0505:ASBMFU>2.0.CO;2, 1986.
- 1290 Sellers, P. J., Dickinson, R. E., Randall, D. A., Betts, A. K., Hall, F. G., Berry, J. A., Collatz, G. J., Denning, A. S., Mooney, H. A., Nobre, C. A., Sato, N., Field, C. B., and Henderson-Sellers, A.: Modeling the Exchanges of Energy, Water, and Carbon Between Continents and the Atmosphere, *Science*, 275, 502–509, doi:10.1126/science.275.5299.502, 1997.
- Shangguan, W., Dai, Y., Duan, Q., Liu, B., and Yuan, H.: A global soil data set for earth system modeling, *Journal of Advances in Modeling Earth Systems*, 6, 249–263, doi:10.1002/2013MS000293, 2014.
- 1295 Sitch, S., Smith, B., Prentice, I. C., Arneth, A., Bondeau, A., Cramer, W., Kaplan, J. O., Levis, S., Lucht, W., Sykes, M. T., Thonicke, K., and Venevsky, S.: Evaluation of ecosystem dynamics, plant geography and terrestrial carbon cycling in the LPJ dynamic global vegetation model, *Global Change Biology*, 9, 161–185, doi:10.1046/j.1365-2486.2003.00569.x, 2003.
- 1300 Spahni, R., Joos, F., Stocker, B. D., Steinacher, M., and Yu, Z. C.: Transient simulations of the carbon and nitrogen dynamics in northern peatlands: from the Last Glacial Maximum to the 21st century, *Climate of the Past*, 9, 1287–1308, doi:10.5194/cp-9-1287-2013, 2013.
- Stocker, B. D., Spahni, R., and Joos, F.: DYPYTOP: a cost-efficient TOPMODEL implementation to simulate sub-grid spatio-temporal dynamics of global wetlands and peatlands, *Geoscientific Model Development*, 7, 3089–3110, doi:10.5194/gmd-7-3089-2014, 2014.
- 1305



- Takala, M., Luoju, K., Pulliainen, J., Derksen, C., Lemmetyinen, J., Kärnä, J. P., Koskinen, J., and Bojkov, B.: Estimating northern hemisphere snow water equivalent for climate research through assimilation of spaceborne radiometer data and ground-based measurements, *Remote Sensing of Environment*, 115, 3517–3529, doi:10.1016/j.rse.2011.08.014, 2011.
- 1310 Tarnocai, C., Canadell, J. G., Schuur, E. A. G., Kuhry, P., Mazhitova, G., and Zimov, S.: Soil organic carbon pools in the northern circumpolar permafrost region, *Global Biogeochemical Cycles*, 23, n/a–n/a, doi:10.1029/2008GB003327, 2009.
- Thonicke, K., Spessa, A., Prentice, I. C., Harrison, S. P., Dong, L., and Carmona-Moreno, C.: The influence of vegetation, fire spread and fire behaviour on biomass burning and trace gas emissions: Results from a process-based model, *Biogeosciences*, 7, 1991–2011, doi:10.5194/bg-7-1991-2010, 2010.
- 1315 Todd-Brown, K. E. O., Randerson, J. T., Post, W. M., Hoffman, F. M., Tarnocai, C., Schuur, E. A. G., and Allison, S. D.: Causes of variation in soil carbon simulations from CMIP5 Earth system models and comparison with observations, *Biogeosciences*, 10, 1717–1736, doi:10.5194/bg-10-1717-2013, 2013.
- Trenberth, K. E., Smith, L., Qian, T., Dai, A., and Fasullo, J.: Estimates of the Global Water Budget and Its Annual Cycle Using Observational and Model Data, *Journal of Hydrometeorology*, 8, 758–769, doi:10.1175/JHM600.1, 2007.
- 1320 Turunen, J., Tomppo, E., Tolonen, K., and Reinikainen, A.: Estimating carbon accumulation rates of undrained mires in Finland – application to boreal and subarctic regions, *The Holocene*, 12, 69–80, doi:10.1191/0959683602h1522rp, 2002.
- 1325 Uppala, S. M., Kallberg, P. W., Simmons, A. J., Andrae, U., Bechtold, V. D. C., Fiorino, M., Gibson, J. K., Haseler, J., Hernandez, A., Kelly, G. A., Li, X., Onogi, K., Saarinen, S., Sokka, N., Allan, R. P., Andersson, E., Arpe, K., Balmaseda, M. A., Beljaars, A. C. M., Berg, L. V. D., Bidlot, J., Bormann, N., Caires, S., Chevallier, F., Dethof, A., Dragosavac, M., Fisher, M., Fuentes, M., Hagemann, S., Hólm, E., Hoskins, B. J., Isaksen, I., Janssen, P. A. E. M., Jenne, R., McNally, A. P., Mahfouf, J.-F., Morcrette, J.-J., Rayner, N. A., Saunders, R. W., Simon, P., Sterl, A., Trenberth, K. E., Untch, A., Vasiljevic, D., Viterbo, P., and Woollen, J.: The ERA-40 re-analysis, *Quarterly Journal of the Royal Meteorological Society*, 131, 2961–3012, doi:10.1256/qj.04.176, 2005.
- 1330 Versegny, D. L., McFarlane, N. A., and Lazare, M.: Class—A Canadian land surface scheme for GCMS, II. Vegetation model and coupled runs, *International Journal of Climatology*, 13, 347–370, doi:10.1002/joc.3370130402, 1993.
- 1335 Wagner, W., Dorigo, W., de Jeu, R., Fernandez, D., Benveniste, J., Haas, E., and Ertl, M.: Fusion of Active and Passive Microwave Observations To Create an Essential Climate Variable Data Record on Soil Moisture, *ISPRS Annals of Photogrammetry, Remote Sensing and Spatial Information Sciences*, I-7, 315–321, doi:10.5194/isprsannals-I-7-315-2012, 2012.
- 1340 Walters, D. N., Williams, K. D., Boutle, I. A., Bushell, A. C., Edwards, J. M., Field, P. R., Lock, A. P., Morcrette, C. J., Stratton, R. A., Wilkinson, J. M., Willett, M. R., Bellouin, N., Bodas-Salcedo, A., Brooks, M. E., Copsey, D., Earnshaw, P. D., Hardiman, S. C., Harris, C. M., Levine, R. C., MacLachlan, C., Manners, J. C., Martin, G. M., Milton, S. F., Palmer, M. D., Roberts, M. J., Rodríguez, J. M., Tennant, W. J., and Vidale, P. L.: The Met Office Unified Model Global Atmosphere 4.0 and JULES Global Land 4.0 configurations, *Geoscientific Model Development*, 7, 361–386, doi:10.5194/gmd-7-361-2014, 2014.
- 1345



- Wania, R., Ross, I., and Prentice, I. C.: Integrating peatlands and permafrost into a dynamic global vegetation model: 2. Evaluation and sensitivity of vegetation and carbon cycle processes, *Global Biogeochemical Cycles*, 23, n/a–n/a, doi:10.1029/2008GB003413, 2009.
- 1350 Warren, S. G. and Wiscombe, W. J.: A Model for the Spectral Albedo of Snow. I: Pure Snow, *Journal of the Atmospheric Sciences*, 37, 2712–2733, doi:10.1175/1520-0469(1980)037%3C2712:AMFTSA%3E2.0.CO;2, 1980.
- Watanabe, K. and Mizoguchi, M.: Amount of unfrozen water in frozen porous media saturated with solution, *Cold Regions Science and Technology*, 34, 103–110, doi:http://dx.doi.org/10.1016/S0165-232X(01)00063-5, 2002.
- 1355 Weedon, G., Balsamo, G., Bellouin, N., Gomes, S., Best, M., and Viterbo, P.: Data methodology applied to ERA-Interim reanalysis data, *Water Resources Research*, 50, 7505–7514, doi:10.1002/2014WR015638.Received, 2014.
- Weedon, G. P., Gomes, S., Viterbo, P., Shuttleworth, W. J., Blyth, E., Österle, H., Adam, J. C., Bellouin, N., Boucher, O., and Best, M.: Creation of the WATCH Forcing Data and Its Use to Assess Global and Regional  
1360 Reference Crop Evaporation over Land during the Twentieth Century, *Journal of Hydrometeorology*, 12, 823–848, doi:10.1175/2011JHM1369.1, 2011.
- Willeit, M. and Ganopolski, A.: Coupled Northern Hemisphere permafrost-ice-sheet evolution over the last glacial cycle, *Climate of the Past*, 11, 1165–1180, doi:10.5194/cp-11-1165-2015, 2015.
- Willeit, M., Ganopolski, A., Dalmonech, D., Foley, A. M., and Feulner, G.: Time-scale and state dependence of  
1365 the carbon-cycle feedback to climate, *Climate Dynamics*, 42, 1699–1713, doi:10.1007/s00382-014-2102-z, 2014a.
- Willeit, M., Ganopolski, A., and Feulner, G.: Asymmetry and uncertainties in biogeophysical climate – vegetation feedback over a range of CO<sub>2</sub> forcings, *Biogeosciences*, 11, 17–32, doi:10.5194/bg-11-17-2014, 2014b.
- Williams, P. and Smith, M.: *The Frozen Earth: Fundamentals of Geocryology*, Cambridge University Press:  
1370 Cambridge, 1989.
- Woodward, F. I.: *Climate and plant distribution*, Cambridge University Press, 1987.
- Woodward, F. I., Lomas, M. R., and Betts, R. A.: Vegetation-climate feedbacks in a greenhouse world, *Philosophical Transactions of the Royal Society B: Biological Sciences*, 353, 29–39, doi:10.1098/rstb.1998.0188, 1998.
- 1375 Yen, Y.: Review of thermal properties of snow, ice and sea ice, 1981.
- Yu, Z., Loisel, J., Brosseau, D. P., Beilman, D. W., and Hunt, S. J.: Global peatland dynamics since the Last Glacial Maximum, *Geophysical Research Letters*, 37, n/a–n/a, doi:10.1029/2010GL043584, 2010.
- Zeng, X.: Global Vegetation Root Distribution for Land Modeling, *Journal of Hydrometeorology*, 2, 525–530, doi:10.1175/1525-7541(2001)002<0525:GVRDFL>2.0.CO;2, 2001.
- 1380 Zeng, X. and Wang, A.: Consistent Parameterization of Roughness Length and Displacement Height for Sparse and Dense Canopies in Land Models, *Journal of Hydrometeorology*, 8, 730–737, doi:10.1175/JHM607.1, 2007.
- Zeng, X., Barlage, M., Dickinson, R. E., Dai, Y., Wang, G., and Oleson, K.: Treatment of Undercanopy Turbulence in Land Models, *Journal of Climate*, 18, 5086–5094, doi:10.1175/JCLI3595.1, 2005.

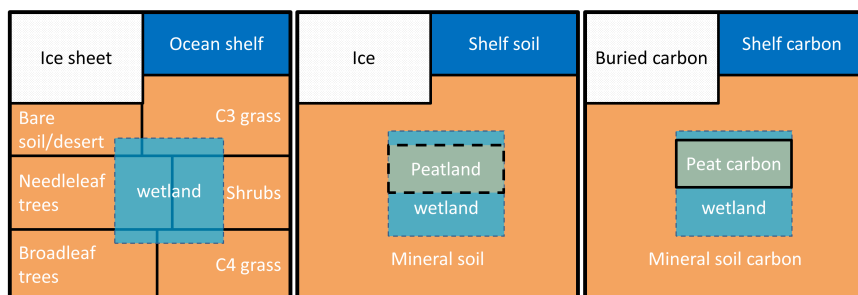


**Figure 1.** PALADYN surface types (left), 'soil' columns (middle) and soil carbon pools (right).

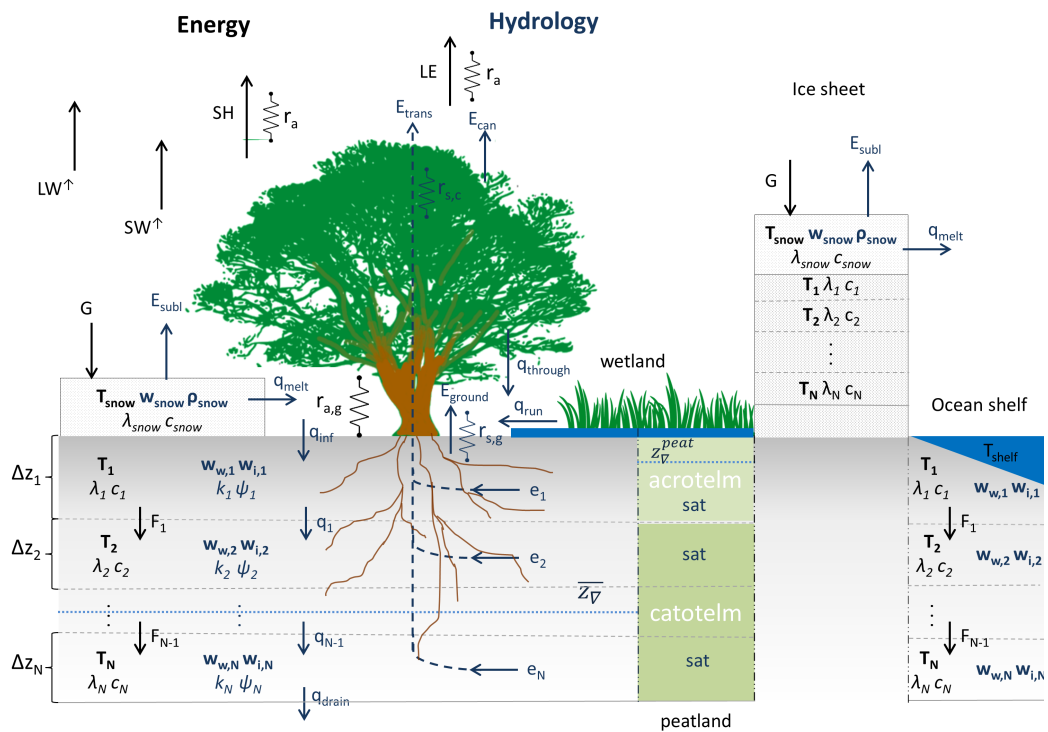


**Figure 2.** Illustration of the physical processes included in PALADYN. Energy fluxes and variables are indicated in black while water fluxes and hydrological variables are indicated in blue. Prognostic variables are in bold and fluxes are accompanied by arrows.

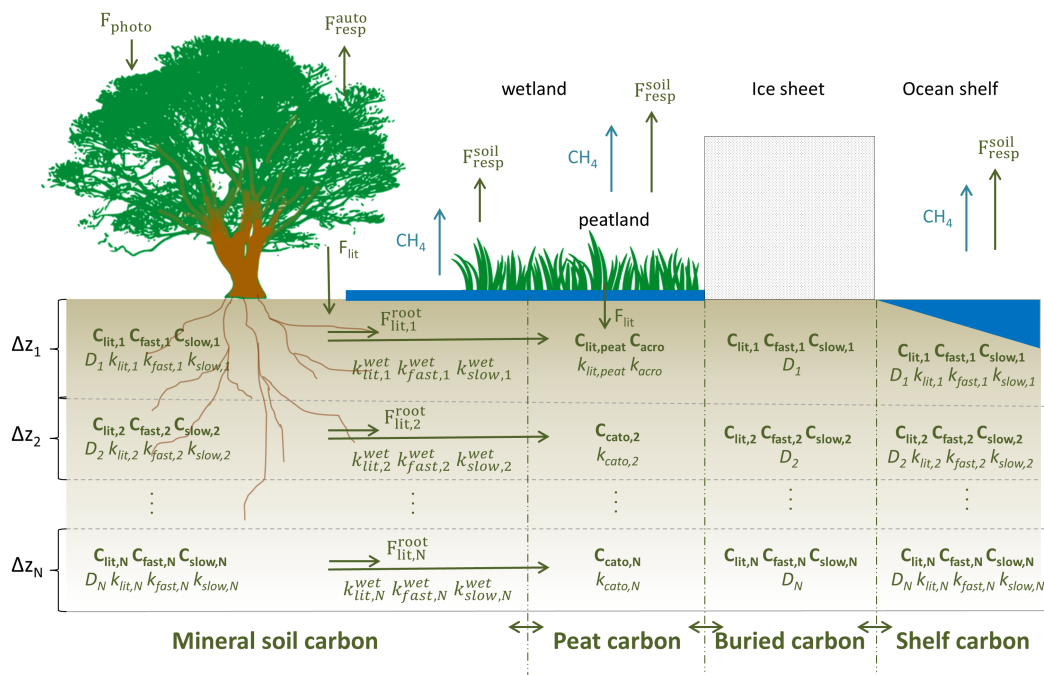


**Figure 3.** Illustration of the carbon cycle processes represented in PALADYN. Prognostic variables are in bold and fluxes are accompanied by arrows.

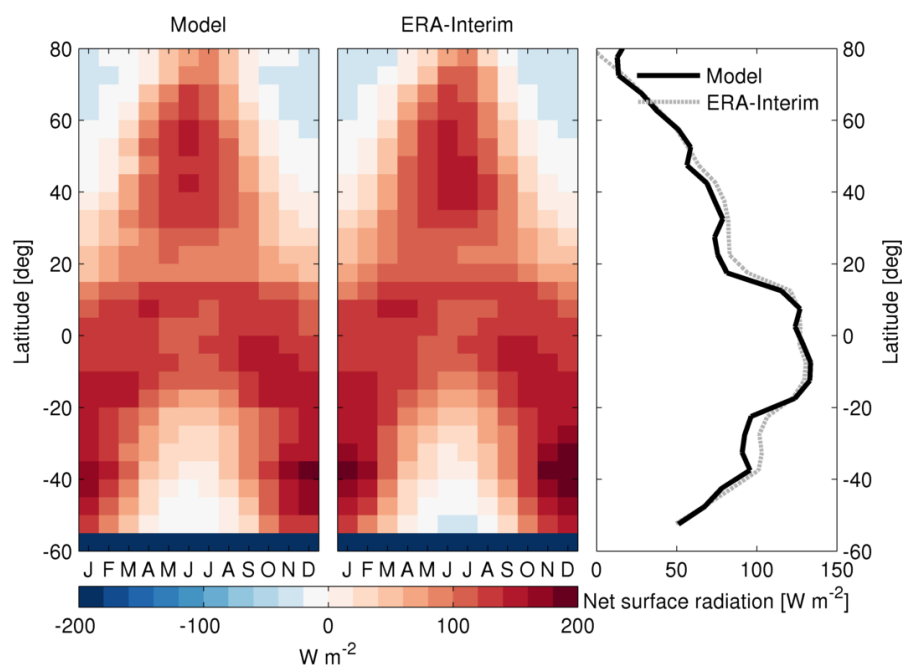


**Figure 4.** Seasonal variation of zonal mean net radiation at the surface modelled by PALADYN (a) and from ERA-Interim reanalysis (Dee et al., 2011) (b). (c) Modelled zonal annual mean net surface radiation compared to ERA-Interim reanalysis (Dee et al., 2011).

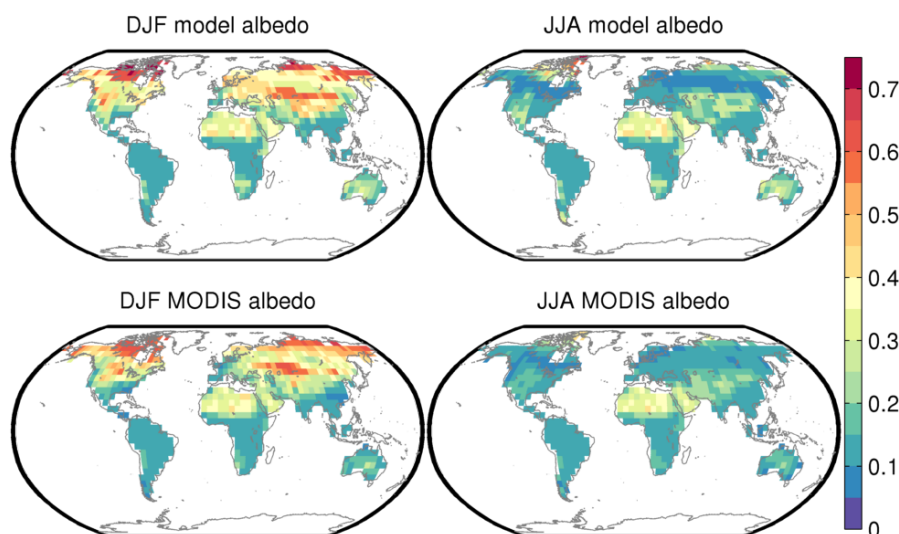


**Figure 5.** December-January-February (left) and June-July-August (right) surface albedo as modelled by PALADYN (top) and derived from MODIS data (Schaaf and Wang, 2015) (bottom). The displayed surface albedo is a weighted mean of visible and near infrared broadband albedo for diffuse radiation.



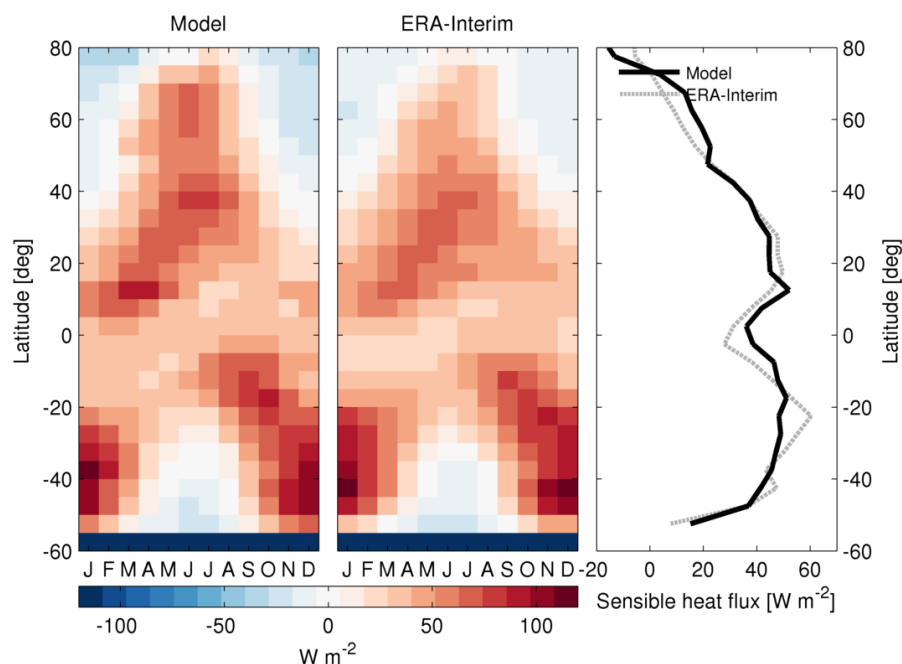


**Figure 6.** Seasonal variation of zonal mean sensible heat flux modelled by PALADYN (left) and from ERA-Interim reanalysis (Dee et al., 2011) (middle). (right) Modelled zonal annual mean sensible heat flux compared to ERA-Interim reanalysis (Dee et al., 2011).

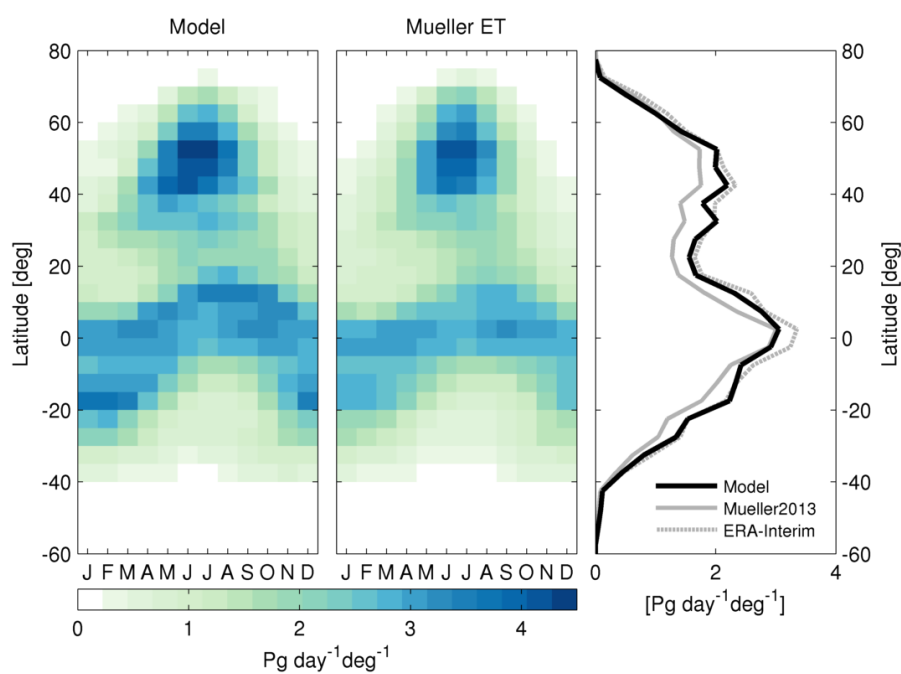


**Figure 7.** Seasonal variation of zonally integrated evapotranspiration modelled by PALADYN (left) and estimated by Mueller et al. (2013) (middle). (right) Modelled zonal annual mean evapotranspiration compared to observation-based estimates from Mueller et al. (2013) and ERA-Interim reanalysis (Dee et al., 2011).

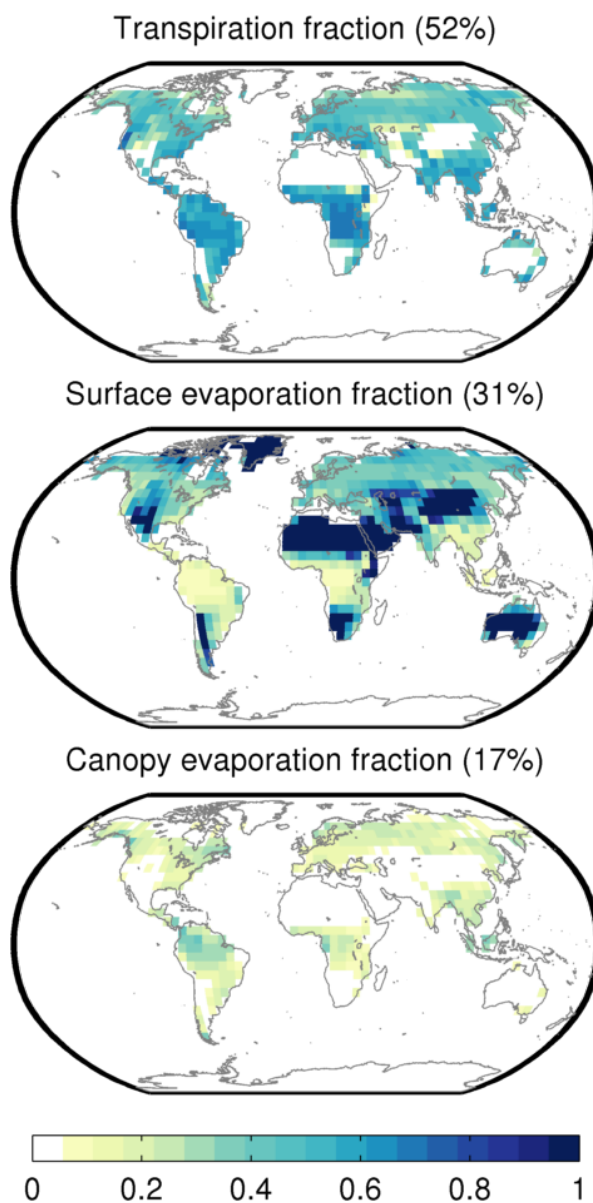


**Figure 8.** Partitioning of modelled total annual evapotranspiration between transpiration (top), surface evaporation (middle) and canopy evaporation (bottom). The global percentage of each component is shown above the corresponding plot.

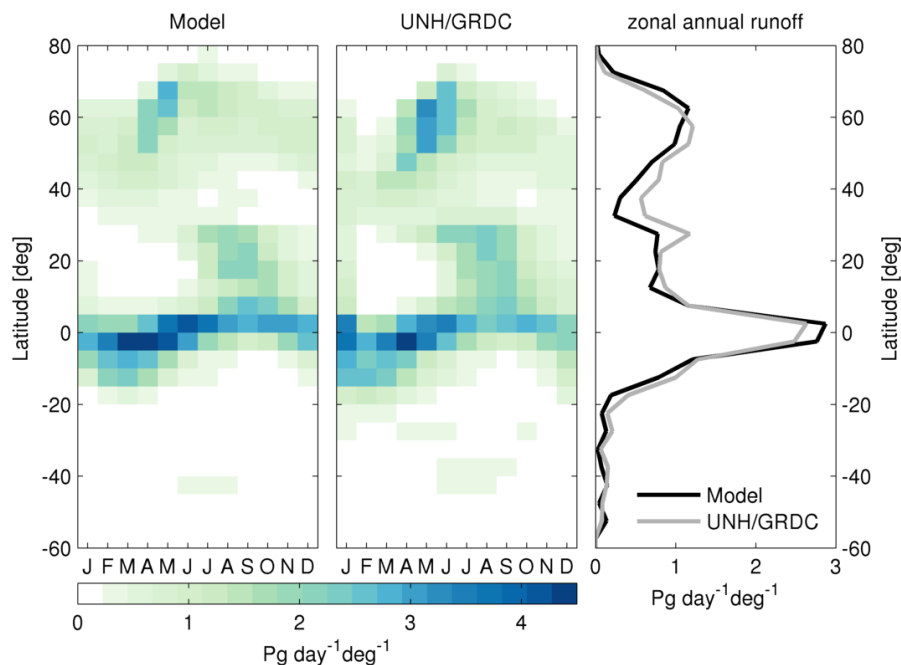


**Figure 9.** Seasonal variation of zonally integrated water runoff modelled by PALADYN (left) and observed by UNH/GRDC (Fekete et al., 2002) (middle). (right) Modelled zonal annual mean runoff compared to observation-based estimates from Fekete et al. (2002). Modelled and observed runoff is averaged over the time period 1979-2010.

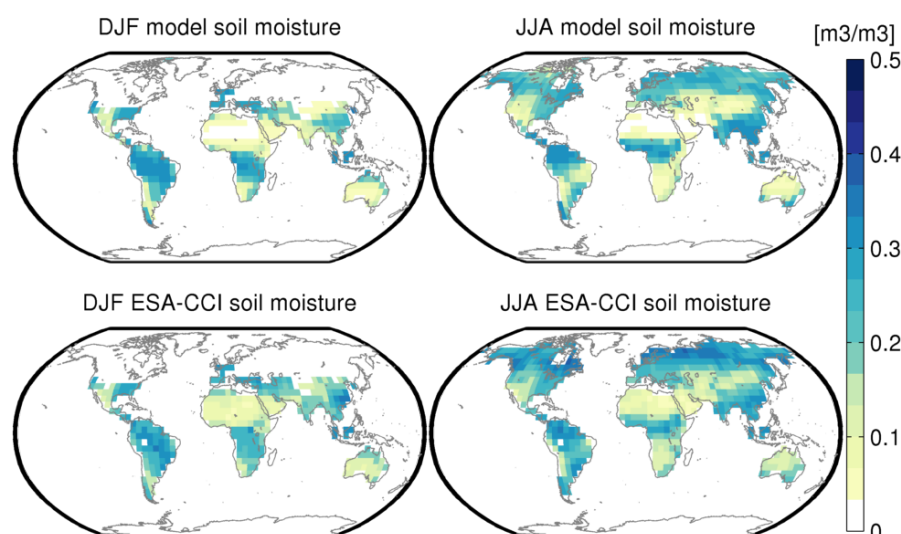


**Figure 10.** December-January-February (left) and June-July-August (right) soil moisture. The modelled soil moisture (top) is the volumetric soil moisture of the top soil layer (top 20 cm). The observed soil moisture is from ESA-CCI (Liu et al., 2012; Wagner et al., 2012) and represents the moisture content of the top few centimeters of soil. Snow covered regions are masked out.

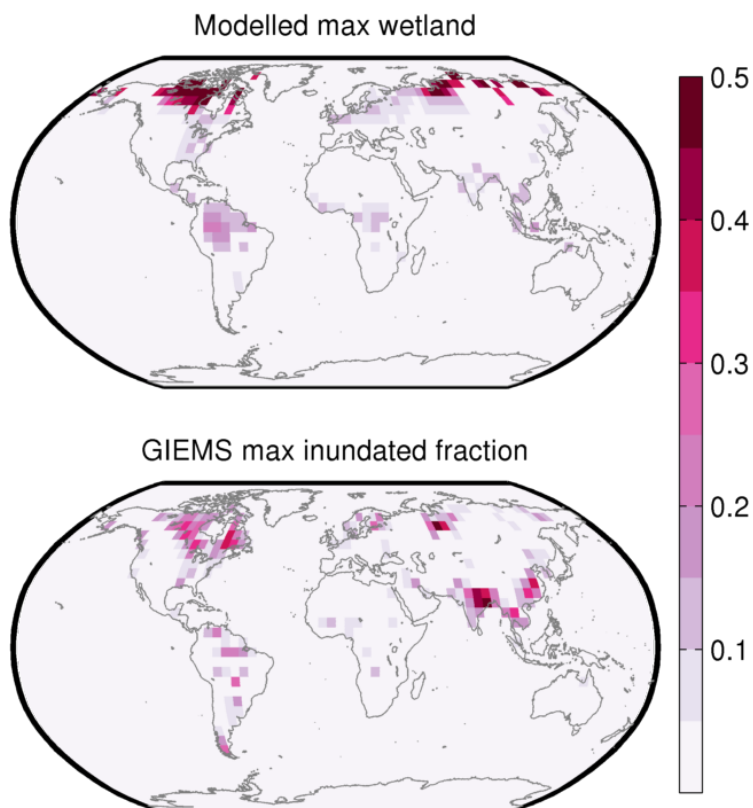


**Figure 11.** Monthly maximum wetland fraction over the time interval 1993-2007 as modelled by PALADYN (top) and inferred by GIEMS (Prigent et al., 2007; Papa et al., 2010) (bottom).

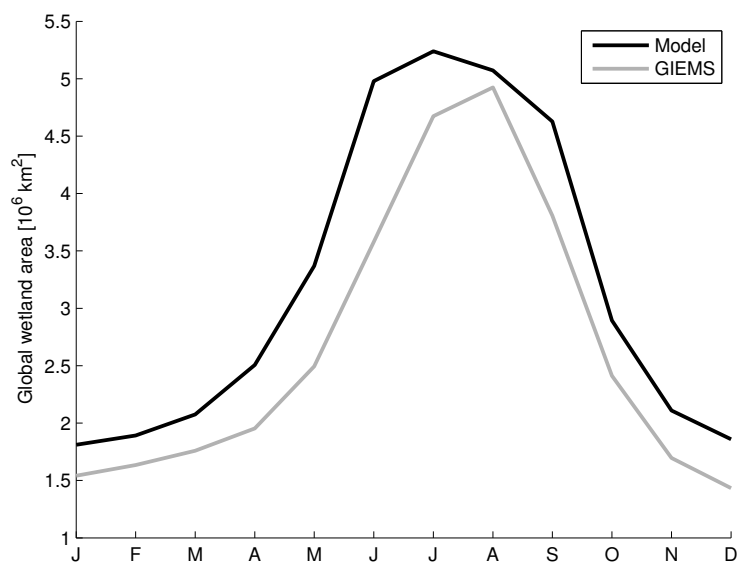


**Figure 12.** Mean seasonal global wetland extent over the time interval 1993-2007 as modelled by PALADYN and inferred by GIEMS (Prigent et al., 2007; Papa et al., 2010).

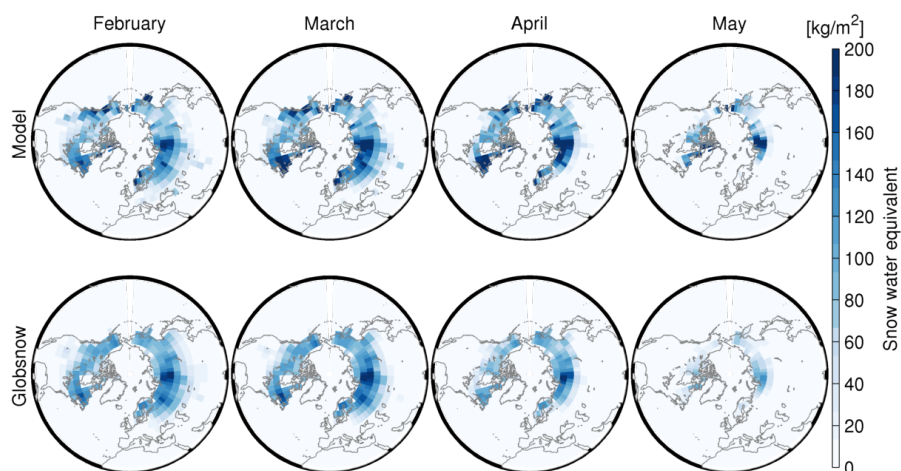


**Figure 13.** February to May snow water equivalent mean over the period 1980-2010 for PALADYN (top) compared to data from the GlobSnow project (Takala et al., 2011; Luojus et al., 2013) (bottom).

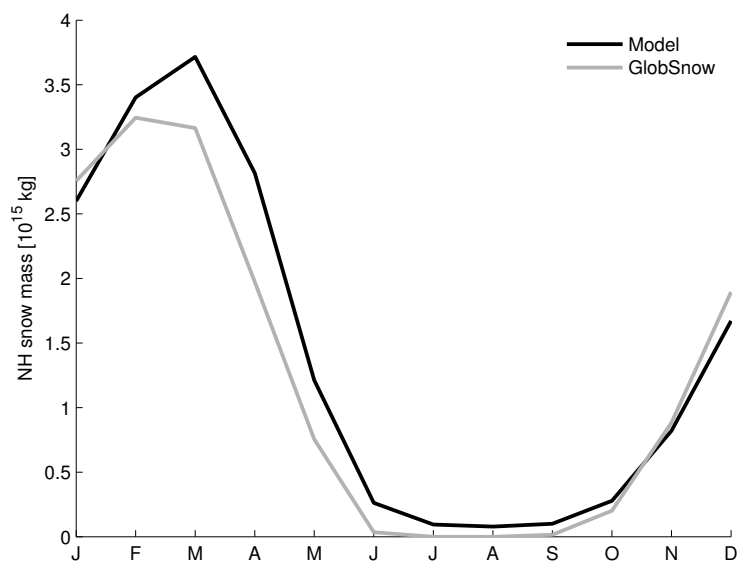


**Figure 14.** Mean 1980-2010 seasonal evolution of the total Northern Hemisphere snow mass compared to data from the GlobSnow project (Takala et al., 2011; Luojus et al., 2013).

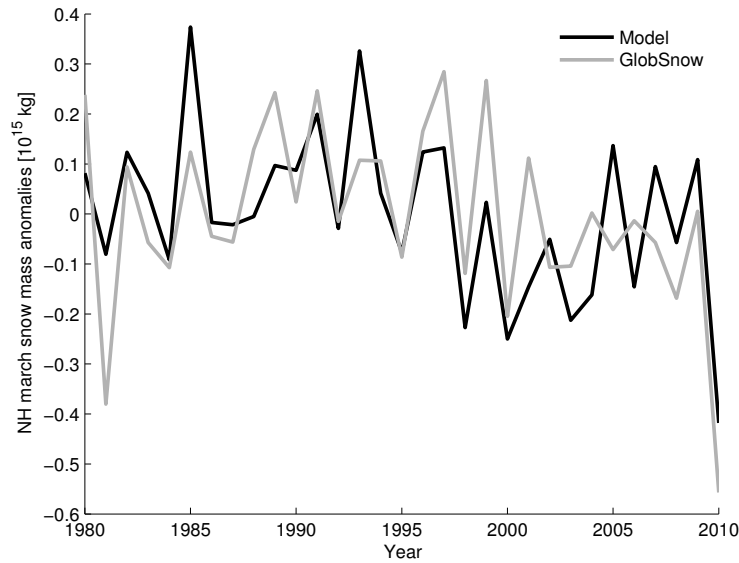


**Figure 15.** Northern Hemisphere March snow mass anomalies from 1980 to 2010 compared to data from the GlobSnow project (Takala et al., 2011; Luoju et al., 2013).

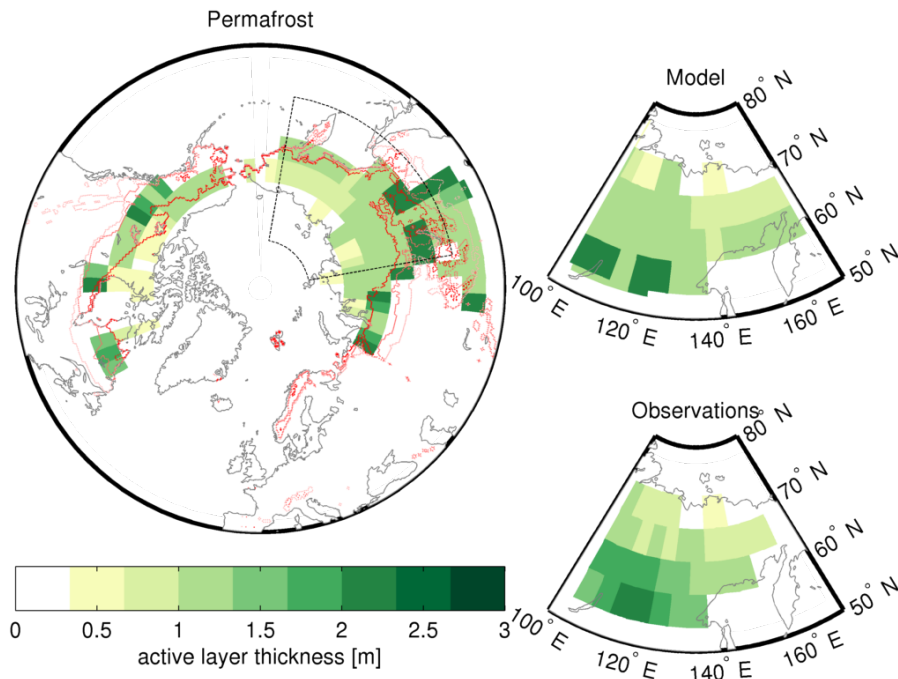


**Figure 16.** Left: modelled permafrost extent and active layer thickness compared to the observed extent of continuous, discontinuous and isolated permafrost (red lines, from dark red to light red) from (Brown et al., 2014). Right: comparison of modelled (top) and observed (bottom) active layer thickness over Yakutia. Active layer thickness data are from (Beer et al., 2013). The modelled active layer thickness is calculated as the mean over the period 1981-2010 in grid cells that are permafrost during the whole time period.

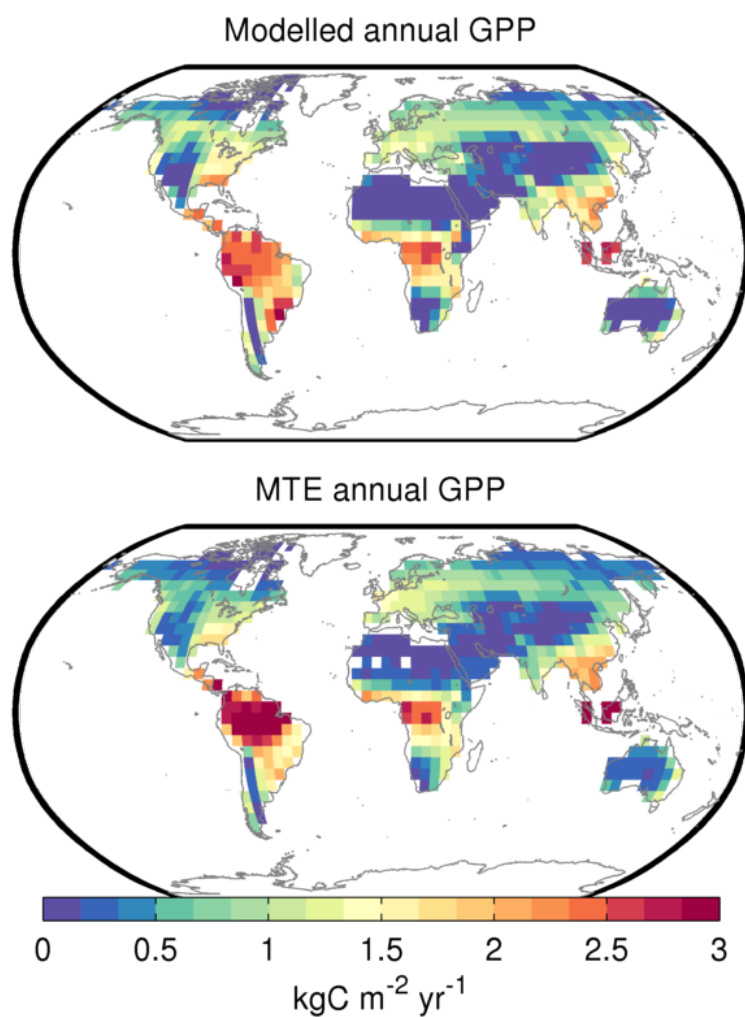


**Figure 17.** Mean annual gross primary production (GPP) over the time interval 1980-2010 as modelled by PALADYN (top) and estimated by the model tree ensemble approach (MTE) (Jung et al., 2009, 2011) (bottom).



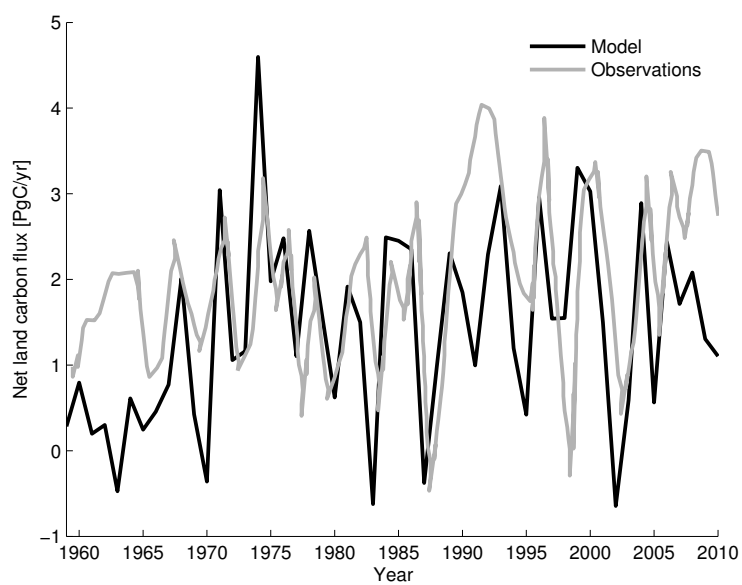


**Figure 18.** Net land carbon uptake for the historical simulation compared to observations from IPCC.

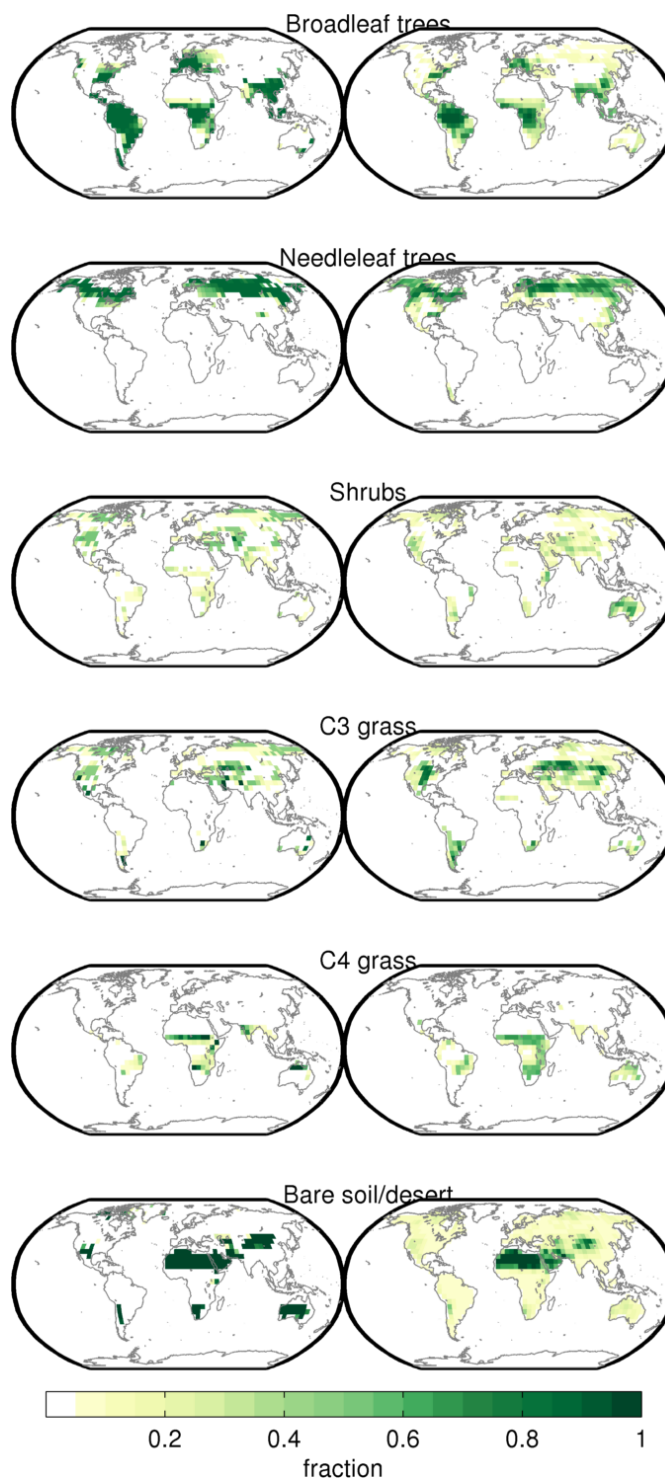


**Figure 19.** Comparison of modelled plant functional types fraction (left) with potential vegetation distribution adapted from Ramankutty and Foley (1999) as described in Appendix D (right).

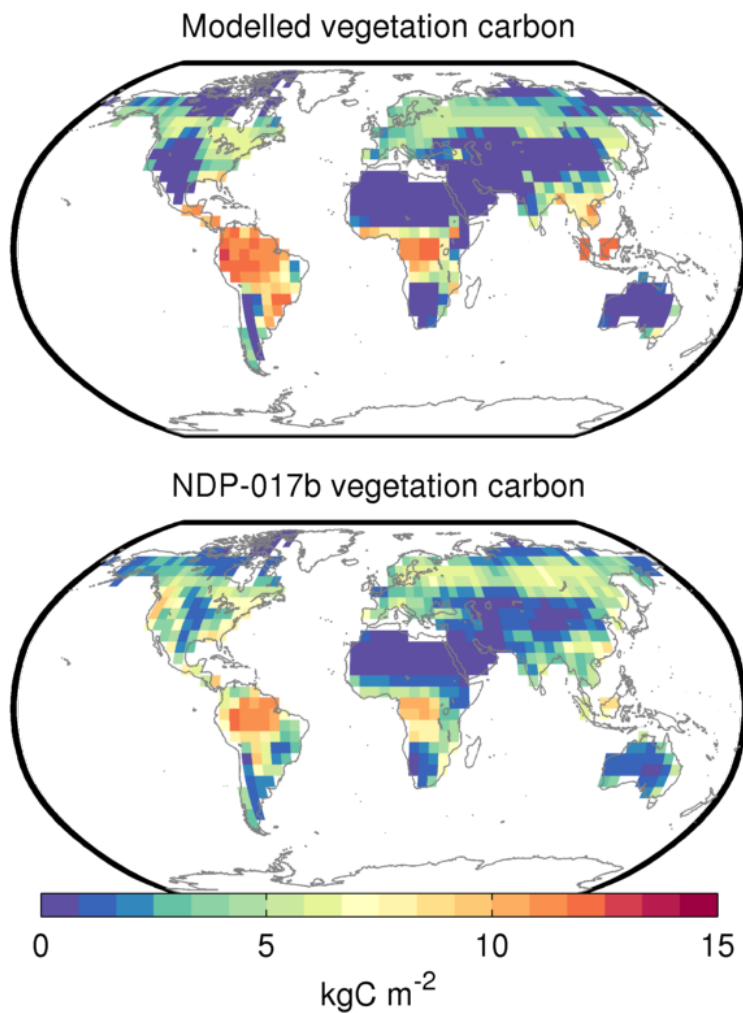


**Figure 20.** Comparison of modelled vegetation carbon content (top) with the observational estimates from the NDP-017b dataset (Gibbs, 2006) (bottom).

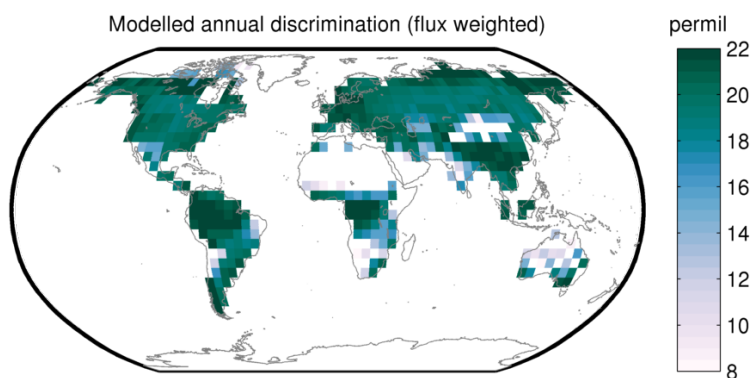


**Figure 21.** Modelled annual flux weighted discrimination during photosynthesis.

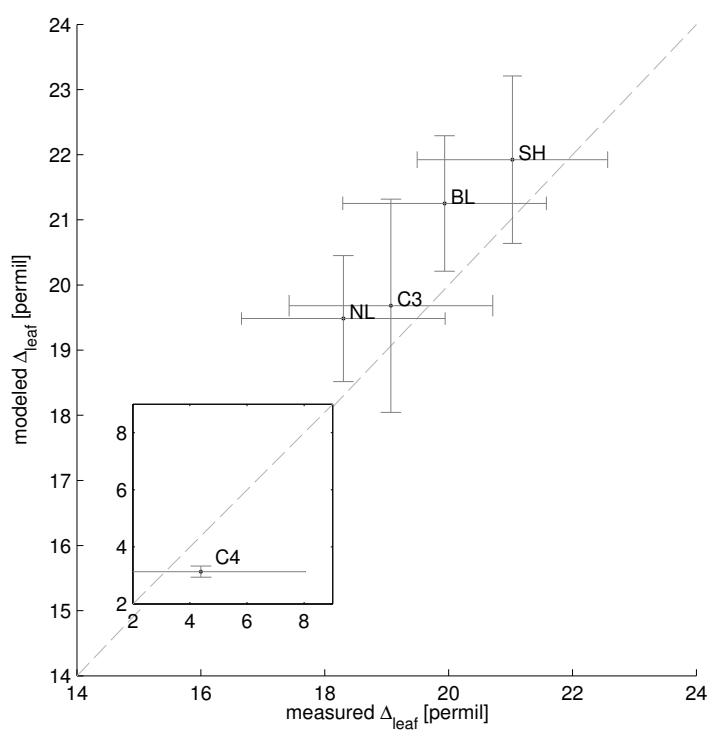


**Figure 22.** Comparison of modelled and observed discrimination during photosynthesis for different plant functional types. Observational data are from (Kaplan et al., 2002).

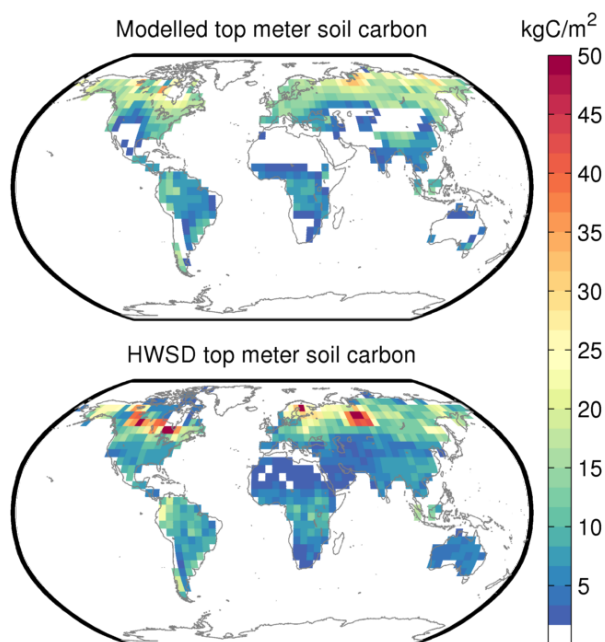


**Figure 23.** Top 1 m soil carbon as modelled by PALADYN (top) and derived from the Harmonized World Soil Database (FAO/IIASA/ISRIC/ISSCAS/JRC, 2012) (bottom).

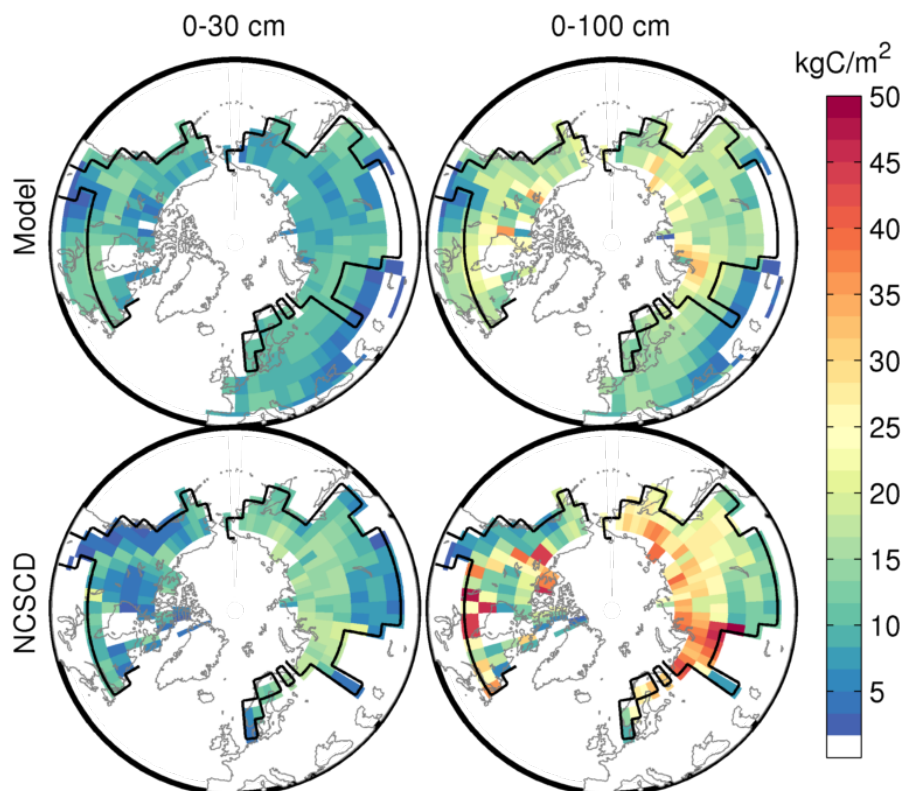


**Figure 24.** Comparison of modelled (top) soil carbon in Northern permafrost regions with estimates from the Northern Circumpolar Soil Carbon Database (NCSCD) (Hugelius et al., 2013b, a; Tarnocai et al., 2009) (bottom) for two depth ranges: (left) 0-30 cm and (right) 0-100 cm.

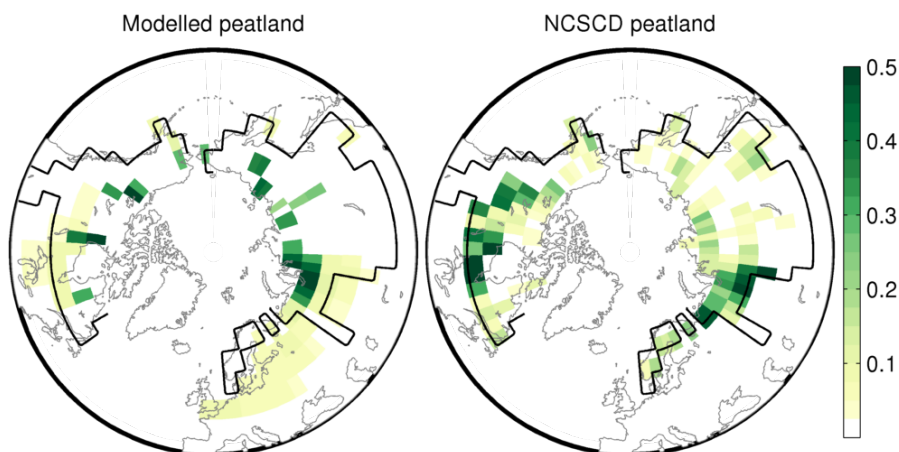


**Figure 25.** Peat fraction as modelled by PALADYN (left) compared to estimates from the Northern Circumpolar Soil Carbon Database (NCSCD) (Hugelius et al., 2013b, a; Tarnocai et al., 2009) (right). The permafrost area as defined in NCSCD is shown as black line. No data are available from the NCSCD dataset outside this area.

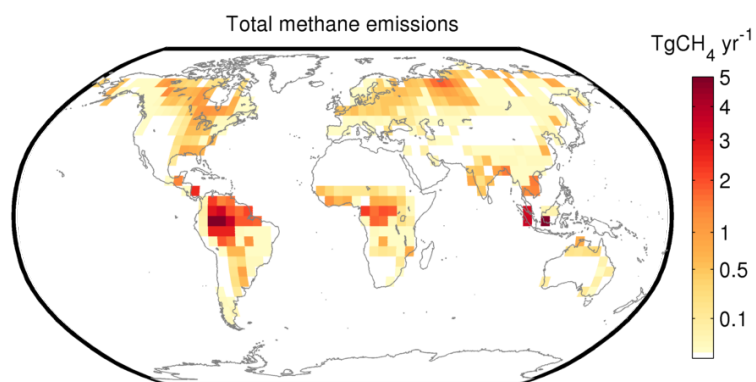


**Figure 26.** Modelled annual methane emissions.



Table 1: Symbol definitions

Symbol	Units	Definition
$\Delta$	‰	isotopic discrimination
$\Delta z_l$	m	thickness of soil layer $l$
$\Lambda$	$\text{kgC m}^{-2} \text{s}^{-1}$	litterfall rate
$\Lambda_{\text{bur}}$	$\text{kgC m}^{-2} \text{s}^{-1}$	vegetation carbon burial rate under ice sheets
$\Lambda_l$	$\text{kgC m}^{-2} \text{s}^{-1}$	leaf litterfall rate
$\Lambda_{\text{loc}}$	$\text{kgC m}^{-2} \text{s}^{-1}$	local litterfall rate
$\Lambda_{\text{peat}}$	$\text{kgC m}^{-2} \text{s}^{-1}$	litterfall rate over peatland
$\Lambda_{\text{shelf}}$	$\text{kgC m}^{-2} \text{s}^{-1}$	litterfall rate over ocean shelf
$\Lambda_{\text{veg}}$	$\text{kgC m}^{-2} \text{s}^{-1}$	litterfall rate over vegetated grid cell area
$\alpha$		surface albedo
$\alpha_a$		factor for <i>APAR</i>
$\alpha^{\text{dir}}$		albedo for direct radiation
$\alpha^{\text{dif}}$		albedo for diffuse radiation
$\alpha^{\text{vis}}$		visible broadband albedo
$\alpha^{\text{nir}}$		near infrared broadband albedo
$\alpha_{\text{can}}$		canopy albedo
$\alpha_g$		ground albedo
$\alpha_{\text{int}}^s$		snowfall interception factor
$\alpha_{\text{int}}^w$		rainfall interception factor
$\alpha_{\text{leaf}}$		leaf albedo
$\alpha_{\text{sn}}$		snow albedo
$\alpha_{\text{sn}}^{\text{can}}$		albedo of snow covered canopy
$\alpha_{\text{sn,fresh}}$		fresh snow albedo
$\alpha_{\text{snfree}}$		snowfree surface albedo
$\alpha_{\text{snfree}}^{\text{can}}$		albedo of snowfree canopy
$\alpha_{\text{soil}}$		snowfree soil albedo
$\beta_{\theta}$		soil moisture limitation factor for photosynthesis
$\beta_s$		surface evaporation factor
$\gamma_v$	$\text{s}^{-1}$	PFT disturbance rate
$\gamma_{v,\text{min}}$	$\text{s}^{-1}$	minimum PFT disturbance rate
$\gamma_l$	$\text{s}^{-1}$	leaf turnover rate
$\gamma_r$	$\text{s}^{-1}$	root turnover rate
$\gamma_s$	$\text{s}^{-1}$	stem turnover rate
$\epsilon$		longwave emissivity





$\eta$	Pa s	snow viscosity
$\eta_0$	Pa s	reference snow viscosity
$\theta$	$\text{m}^3 \text{m}^{-3}$	volumetric total soil moisture
$\theta_{\text{crit}}$	$\text{m}^3 \text{m}^{-3}$	critical soil moisture for fire
$\theta_{\text{fc}}$	$\text{m}^3 \text{m}^{-3}$	volumetric soil moisture at field capacity
$\theta_{\text{i}}$	$\text{m}^3 \text{m}^{-3}$	volumetric frozen soil moisture
$\theta_{\text{r}}$		shape parameter for photosynthesis
$\theta_{\text{sat}}$	$\text{m}^3 \text{m}^{-3}$	soil porosity
$\theta_{\text{w}}$	$\text{m}^3 \text{m}^{-3}$	volumetric liquid soil moisture
$\theta_{\text{wp}}$	$\text{m}^3 \text{m}^{-3}$	volumetric soil moisture at wilting point
$\kappa$		von Karman constant
$\lambda$	$\text{W m}^{-1} \text{K}^{-1}$	heat conductivity
$\lambda_{\text{NPP}}$		<i>NPP</i> partitioning factor
$\lambda_{\text{a}}$	$\text{W m}^{-1} \text{K}^{-1}$	heat conductivity of air
$\lambda_{\text{c}}$		ratio of intercellular to atmospheric $\text{CO}_2$
$\lambda_{\text{dry}}$	$\text{W m}^{-1} \text{K}^{-1}$	heat conductivity of dry soil
$\lambda_{\text{i}}$	$\text{W m}^{-1} \text{K}^{-1}$	heat conductivity of ice
$\lambda_{\text{s}}$	$\text{W m}^{-1} \text{K}^{-1}$	heat conductivity of soil
$\lambda_{\text{s},1}$	$\text{W m}^{-1} \text{K}^{-1}$	heat conductivity of top soil layer
$\lambda_{\text{sat}}$	$\text{W m}^{-1} \text{K}^{-1}$	heat conductivity of saturated soil
$\lambda_{\text{sn}}$	$\text{W m}^{-1} \text{K}^{-1}$	heat conductivity of snow
$\lambda_{\text{w}}$	$\text{W m}^{-1} \text{K}^{-1}$	heat conductivity of water
$\mu$	radians	solar zenith angle
$\nu$		PFT fractional area coverage
$\nu_{\text{seed}}$		PFT seed fraction
$\rho_{\text{a}}$	$\text{kg m}^{-3}$	air density
$\rho_{\text{i}}$	$\text{kg m}^{-3}$	density of ice
$\rho_{\text{sn}}$	$\text{kg m}^{-3}$	density of snow
$\rho_{\text{sn},\text{fresh}}$	$\text{kg m}^{-3}$	density of fresh snow
$\rho_{\text{sn},\text{min}}$	$\text{kg m}^{-3}$	minimum density of snow
$\rho_{\text{w}}$	$\text{kg m}^{-3}$	density of liquid water
$\sigma$	$\text{W m}^{-2} \text{K}^{-4}$	Stefan-Boltzmann constant
$\tau_{\text{fire}}$	s	fire return time scale
$\tau_{\text{s}}$	s	canopy snow removal time scale
$\tau_{\text{w}}$	s	canopy water removal time scale
$\phi$		phenology factor
$\psi$	m	soil matric potential



$\psi_{\text{sat}}$	m	saturated soil matric potential
$APAR$	$\text{mol m}^{-2} \text{ day}^{-1}$	absorbed photosynthetically active radiation
$A_g$	$\text{gC m}^{-2} \text{ day}^{-1}$	daily gross assimilation
$A_n$	$\text{gC m}^{-2} \text{ day}^{-1}$	daily net assimilation
$A_{\text{nd}}$	$\text{gC m}^{-2} \text{ day}^{-1}$	daytime net assimilation
$C_{\text{DN}}^m$		neutral drag coefficient for momentum
$C_{\text{DN}}^h$		neutral drag coefficient for heat and water
$C_{\text{D}}^m$		drag coefficient for momentum
$C_{\text{D}}^h$		drag coefficient for heat and water
$C_{\text{acro}}$	$\text{kgC m}^{-2}$	acrotelm carbon
$C_{\text{acro,crit}}$	$\text{kgC m}^{-2}$	critical acrotelm carbon for catotelm formation
$C_{\text{bare}}$		bare soil drag coefficient
$C_{\text{can}}$		below canopy drag coefficient
$C_{\text{cato}}$	$\text{kgC m}^{-3}$	catotelm carbon density
$C_{\text{dense}}$		dense canopy drag coefficient
$C_p$	$\text{J kg}^{-1} \text{ K}^{-1}$	specific heat capacity of air at constant pressure
$C_i$	$\text{J kg}^{-1} \text{ K}^{-1}$	specific heat capacity of ice
$C_{\text{lit}}$	$\text{kgC m}^{-3}$	litter carbon density
$C_{\text{lit,peat}}$	$\text{kgC m}^{-2}$	peat litter carbon
$C_{\text{fast}}$	$\text{kgC m}^{-3}$	fast soil carbon density
$C_{\text{peat}}$	$\text{kgC m}^{-2}$	peat carbon
$C_{\text{slow}}$	$\text{kgC m}^{-3}$	slow soil carbon density
$C_v$	$\text{kgC m}^{-2}$	vegetation carbon
$C_{v,\text{ag}}$	$\text{kgC m}^{-2}$	aboveground vegetation carbon
$C_{v,\text{high}}$	$\text{kgC m}^{-2}$	aboveground vegetation carbon parameter for fire
$C_{v,\text{l}}$	$\text{kgC m}^{-2}$	leaf carbon
$C_{v,\text{low}}$	$\text{kgC m}^{-2}$	aboveground vegetation carbon parameter for fire
$C_{v,\text{r}}$	$\text{kgC m}^{-2}$	root carbon
$C_{v,\text{s}}$	$\text{kgC m}^{-2}$	stem carbon
$C_w$	$\text{J kg}^{-1} \text{ K}^{-1}$	specific heat capacity of water
$D$	$\text{m}^2 \text{ s}^{-1}$	vertical soil carbon diffusivity
$D_{\text{bio}}$	$\text{m}^2 \text{ s}^{-1}$	bioturbation carbon diffusivity
$D_{\text{cryo}}$	$\text{m}^2 \text{ s}^{-1}$	cryoturbation carbon diffusivity
$E$	$\text{kg m}^{-2} \text{ s}^{-1}$	evapotranspiration
$E_{\text{can}}$	$\text{kg m}^{-2} \text{ s}^{-1}$	canopy evaporation and sublimation
$E_{\text{can}}^s$	$\text{kg m}^{-2} \text{ s}^{-1}$	canopy sublimation
$E_{\text{can}}^w$	$\text{kg m}^{-2} \text{ s}^{-1}$	canopy evaporation



$E_s$	$\text{kg m}^{-2} \text{s}^{-1}$	snow sublimation
$G$	$\text{W m}^{-2}$	ground heat flux
$H$	$\text{W m}^{-2}$	sensible heat flux
$I_{\text{can}}^s$	$\text{kg m}^{-2} \text{s}^{-1}$	canopy snow interception
$I_{\text{can}}^w$	$\text{kg m}^{-2} \text{s}^{-1}$	canopy rain interception
$J_C$	$\text{gC m}^{-2} \text{day}^{-1}$	Rubisco limited photosynthesis rate
$J_E$	$\text{gC m}^{-2} \text{day}^{-1}$	light limited photosynthesis rate
$K$		Kersten number
$L$	$\text{J kg}^{-1}$	latent heat of vaporisation
$L_{\text{ai}}$	$\text{m}^2 \text{m}^{-2}$	leaf area index
$L_{\text{ai,b}}$	$\text{m}^2 \text{m}^{-2}$	balanced leaf area index
$L_f$	$\text{J kg}^{-1}$	latent heat of fusion of water
$LW^\downarrow$	$\text{W m}^{-2}$	downward longwave radiation at the surface
$LW^\uparrow$	$\text{W m}^{-2}$	upward longwave radiation at the surface
$M_s$	$\text{kg m}^{-2} \text{s}^{-1}$	snowmelt
$NPP$	$\text{kgC m}^{-2} \text{s}^{-1}$	net primary production
$P_s$	$\text{kg m}^{-2} \text{s}^{-1}$	snowfall rate
$P_{s,g}$	$\text{kg m}^{-2} \text{s}^{-1}$	snowfall rate reaching the ground
$P_r$	$\text{kg m}^{-2} \text{s}^{-1}$	rainfall rate
$P_{r,g}$	$\text{kg m}^{-2} \text{s}^{-1}$	rainfall rate reaching the ground
$R_d$	$\text{gC m}^{-2} \text{day}^{-1}$	leaf respiration
$R_i$		bulk Richardson number
$R_w$	$\text{kg m}^{-2} \text{s}^{-1}$	surface water runoff
$SLA$	$\text{m}^2 \text{kgC}^{-1}$	specific leaf area
$S_{\text{ai}}$	$\text{m}^2 \text{m}^{-2}$	stem area index
$SW^\downarrow$	$\text{W m}^{-2}$	downward shortwave radiation at the surface
$T_0$	K	freezing temperature of water
$T_*$	K	skin temperature
$T_a$	K	air temperature at height $z_{\text{ref}}$
$T_{\text{cmon}}^{\text{max}}$	K	maximum coldest month temperature for establishment
$T_{\text{cmon}}^{\text{min}}$	K	minimum coldest month temperature for establishment
$T_{\text{cmon}}^{\text{phen}}$	K	coldest month temperature for phenology
$T_{\text{gdd}}^{\text{base}}$	K	base temperature for phenology
$T_{s,1}$	K	top soil layer or snow temperature
$T_s$	K	soil/snow temperature
$VPD$	kPa	vapor pressure deficit
$V_a$	$\text{m s}^{-1}$	wind speed at height $z_{\text{ref}}$



$V_m$	$\text{gC m}^{-2} \text{ day}^{-1}$	maximum daily rate of net photosynthesis
$a_C$		factor for leaf respiration
$a_{wl}$	$\text{kgC m}^{-2}$	allometric coefficient
$a_{ws}$		ratio of total to respiring stem carbon
$b$		Clapp and Hornberger parameter
$c$	$\text{J m}^{-3} \text{ K}^{-1}$	volumetric heat capacity
$c_1$	$\text{g mol}^{-1}$	factor for light limited assimilation
$c_2$		factor for Rubisco limited assimilation
$c_a$	$\text{mol mol}^{-1}$	atmospheric $\text{CO}_2$ mole fraction
$c_i$	$\text{mol mol}^{-1}$	intercellular $\text{CO}_2$ mole fraction
$c_{ij}$		PFT competition coefficients
$c_q$	$\text{mol J}^{-1}$	conversion factor for solar radiation
$c_s$	$\text{J m}^{-3} \text{ K}^{-1}$	volumetric heat capacity of dry soil
$c_{sn}$	$\text{J m}^{-3} \text{ K}^{-1}$	volumetric heat capacity of snow
$d$	m	zero plane displacement
$d_h$	hours	daylength
$d_{r,1}$	m	root distribution parameter
$d_{r,2}$	m	root distribution parameter
$e$	$\text{kg m}^{-2} \text{ s}^{-1}$	soil moisture removal by evapotranspiration
$f_{\nabla}$		parameter for computation of water table depth
$f_{\theta}$		soil moisture factor for soil carbon decomposition rate
$f_{\theta, \text{peat}}$		soil moisture factor for peat carbon decomposition rate
$f_{\theta, \text{sat}}$		soil moisture factor for soil carbon decomposition rate at saturation
$f_T$		temperature factor for soil carbon decomposition rate
$f_{\mu}$		solar zenith angle factor for snow albedo
$f_{\text{age}}$		snow age factor
$f_{\text{frz, crit}}$		critical fraction of frozen soil water for permafrost carbon
$f_{\text{ice}}$		fraction of grid cell covered by ice sheets
$f_{\text{inert}}$		frozen soil factor for soil carbon decomposition
$f_{\text{inun}}$		inundated grid cell fraction
$f_{\text{lit}}^{\text{resp}}$		fraction of decomposed litter carbon going to atmosphere
$f_{\text{lit} \rightarrow \text{fast}}$		fraction of decomposed litter transferred to fast carbon pool
$f_{\text{lit} \rightarrow \text{slow}}$		fraction of decomposed litter transferred to slow carbon pool
$f_{\text{org}}$		organic soil fraction
$f_{\text{oxic}}$		fraction of litter and acrotelm respiring in oxic conditions
$f_{\text{peat}}$		peatland fraction
$f_{\text{sat}}$		saturated grid cell fraction



$f_{\text{sat}}^{\text{max}}$		maximum saturated grid cell fraction
$f_{\text{shelf}}$		fraction of grid cell below sea level
$f_{\text{sn}}$		snow fraction
$f_{\text{sn}}^{\text{can}}$		canopy snow fraction
$f_{\text{sv}}$		sky view factor
$f_{\text{sv}}^{\text{dir}}$		direct beam sky view factor
$f_{\text{sv}}^{\text{dif}}$		diffuse radiation sky view factor
$f_{\text{veg} \rightarrow \text{bur}}$		fraction of vegetation carbon buried below ice sheets
$f_{\text{wet}}$		wetland fraction
$g$	$\text{m s}^{-2}$	gravitational acceleration
$gdd$	K	growing degree days above $T_{\text{gdd}}^{\text{base}}$
$gdd_{\text{crit}}$	K	critical growing degree days for phenology
$gdd_{\text{min}}$	K	minimum growing degree days for establishment
$g_1$		parameter in optimal stomatal conductance model
$g_{\text{can}}$	$\text{m s}^{-1}$	canopy conductance
$g_{\text{min}}$	$\text{m s}^{-1}$	minimum canopy conductance
$h_{\text{sn}}$	m	snow thickness
$h_{\text{soil}}$	m	depth of the soil column
$h_{\text{v}}$	m	vegetation height
$k$	$\text{kg m}^{-2} \text{s}^{-1}$	hydraulic soil conductivity
$k_{\text{acro}}$	$\text{s}^{-1}$	acrotelm carbon turnover rate
$k_{\text{acro} \rightarrow \text{cato}}$	$\text{s}^{-1}$	catotelm formation rate
$k_{\text{cato}}$	$\text{s}^{-1}$	catotelm carbon turnover rate
$k_{\text{ext}}$		extinction coefficient for radiation
$k_{\text{fast}}$	$\text{s}^{-1}$	fast carbon turnover rate
$k_{\text{fast},10}$	$\text{s}^{-1}$	fast soil carbon turnover rate at 10 °C
$k_{\text{inert}}$	$\text{s}^{-1}$	inert soil carbon turnover rate
$k_{\text{lit}}$	$\text{s}^{-1}$	litter carbon turnover rate
$k_{\text{lit},10}$	$\text{s}^{-1}$	litter carbon turnover rate at 10 °C
$k_{\text{lit,peat}}$	$\text{s}^{-1}$	peat litter carbon turnover rate
$k_{\text{sat}}$	$\text{kg m}^{-2} \text{s}^{-1}$	hydraulic soil conductivity at saturation
$k_{\text{slow}}$	$\text{s}^{-1}$	slow soil carbon turnover rate
$k_{\text{slow},10}$	$\text{s}^{-1}$	slow soil carbon turnover rate at 10 °C
$k_{\rho}$	$\text{m}^3 \text{kg}^{-1}$	factor for density dependence of snow viscosity
$k_{\text{T}}$	$\text{K}^{-1}$	factor for temperature dependence of snow viscosity
$n_{\text{al}}$		multiple of active layer thickness for cryoturbation
$p_{\text{a}}$	Pa	partial pressure of atmospheric CO <sub>2</sub>



$p_i$	Pa	partial pressure of intercellular CO <sub>2</sub>
$q$	kg m <sup>-2</sup> s <sup>-1</sup>	soil water flux
$q_a$	kg kg <sup>-1</sup>	air specific humidity at height $z_{\text{ref}}$
$q_{\text{drain}}$	kg m <sup>-2</sup> s <sup>-1</sup>	soil water drainage
$q_{\text{inf}}$	kg m <sup>-2</sup> s <sup>-1</sup>	soil water infiltration
$q_{\text{inf}}^{\text{max}}$	kg m <sup>-2</sup> s <sup>-1</sup>	maximum soil water infiltration
$q_{\text{sat}}$	kg kg <sup>-1</sup>	specific humidity at saturation
$r$		cumulative root fraction
$r_a$	s m <sup>-1</sup>	aerodynamic resistance
$r_{a,\text{can}}$	s m <sup>-1</sup>	below-canopy aerodynamic resistance
$r_s$	s m <sup>-1</sup>	surface resistance to water vapor flux
$u_*$	m s <sup>-1</sup>	friction velocity
$w_{\text{can}}^w$	kg m <sup>-2</sup>	canopy liquid water
$w_{\text{can}}^s$	kg m <sup>-2</sup>	canopy snow water equivalent
$w_i$	kg m <sup>-2</sup>	soil frozen water content
$w_{\text{sn}}$	kg m <sup>-2</sup>	snow water equivalent
$w_w$	kg m <sup>-2</sup>	soil liquid water content
$w_w^{\text{max}}$	kg m <sup>-2</sup>	maximum soil liquid water content
$z_0^b$	m	bare soil roughness length
$z_0^i$	m	ice roughness length
$z_0^{\text{sn}}$	m	snow roughness length
$z_0^{\text{snfree}}$	m	snow-free roughness length
$z_0^v$	m	vegetation roughness length
$z_0^w$	m	water roughness length
$z_{\nabla}$	m	grid cell mean water table depth
$z_{\nabla}^{\text{min}}$	m	minimum water table depth
$z_{\nabla}^{\text{peat}}$	m	peatland water table depth
$z_{\text{al}}$	m	active layer thickness
$z_{\text{acro}}$	m	acrotelm thickness
$z_m$	m	roughness length for momentum
$z_h$	m	roughness length for scalars
$z_{\text{ref}}$	m	reference height



**Table 2.** Surface model parameters.

$k_{\text{ext}} = 0.5$	extinction coefficient for radiation
$\alpha_{\text{sn,fresh}}^{\text{vis,dif}} = 0.95$	diffuse visible fresh snow albedo
$\alpha_{\text{sn,fresh}}^{\text{nir,dif}} = 0.65$	diffuse near infrared fresh snow albedo
$z_0^{\text{b}} = 0.005 \text{ m}$	bare soil roughness length
$z_0^{\text{i}} = 0.01 \text{ m}$	ice roughness length
$z_0^{\text{w}} = 0.001 \text{ m}$	water roughness length
$z_0^{\text{sn}} = 0.0024 \text{ m}$	snow roughness length
$C_{\text{bare}} = 0.05$	bare soil drag coefficient
$C_{\text{dense}} = 0.005$	dense canopy drag coefficient
$\alpha_{\text{int}}^{\text{w}} = 0.2$	canopy water interception parameter
$\alpha_{\text{int}}^{\text{s}} = 0.5$	canopy snow interception parameter
$\tau_{\text{w}} = 1 \text{ day}$	canopy water removal time scale
$\tau_{\text{s}} = 10 \text{ days}$	canopy snow removal time scale
$\rho_{\text{sn,min}} = 50 \text{ kg m}^{-3}$	minimum snow density
$\eta_0 = 9 \times 10^6 \text{ Pa s}$	reference snow viscosity
$k_{\text{T}} = 0.06 \text{ K}^{-1}$	temperature parameter for snow viscosity
$k_{\rho} = 0.02 \text{ m}^3 \text{ kg}^{-1}$	density parameter for snow viscosity
$f_{\nabla} = 1.6$	parameter for saturated grid cell fraction

**Table 3.** Soil model parameters.

$c_{\text{s}} = 2.3 \times 10^6 \text{ J m}^{-3} \text{ K}^{-1}$	volumetric heat capacity of soil
$\lambda_{\text{s}} = 5.0 \text{ W m}^{-1} \text{ K}^{-1}$	soil heat conductivity at saturation
$\lambda_{\text{dry}} = 0.2 \text{ W m}^{-1} \text{ K}^{-1}$	dry soil heat conductivity
$\theta_{\text{sat}} = 0.43 \text{ m}^3 \text{ m}^{-3}$	soil porosity
$\theta_{\text{fc}} = 0.25 \text{ m}^3 \text{ m}^{-3}$	volumetric soil moisture at field capacity
$\theta_{\text{wp}} = 0.14 \text{ m}^3 \text{ m}^{-3}$	volumetric soil moisture at wilting point
$\psi_{\text{sat}} = -0.2 \text{ m}$	soil matric potential at saturation
$k_{\text{sat}} = 520 \text{ kg m}^{-2} \text{ day}^{-1}$	soil hydraulic conductivity at saturation
$b = 6$	Clapp-Hornberger parameter



**Table 4.** Photosynthesis model parameters (Sitch et al., 2003).

$\theta_r$	0.7	co-limitation parameter
$\alpha_{\text{leaf}}$	0.17	leaf albedo in PAR range
$\alpha$	0.5	fraction of PAR assimilated at ecosystem level
$c_q$	$4.6 \times 10^{-6} \text{ mol J}^{-1}$	conversion factor for solar radiation at 550 nm
$a_{C3}$	0.015	leaf respiration as a fraction of Rubisco capacity in C3 plants
$a_{C4}$	0.02	leaf respiration as a fraction of Rubisco capacity in C4 plants
$\alpha_{C3}$	0.08	intrinsic quantum efficiency of $\text{CO}_2$ uptake in C3 plants
$\alpha_{C4}$	0.053	intrinsic quantum efficiency of $\text{CO}_2$ uptake in C4 plants
$[\text{O}_2]$	20.9 kPa	$\text{O}_2$ partial pressure
$C_{\text{mass}}$	12	atomic mass of carbon





**Table 5.** Plant functional type specific model parameters.

		Broadleaf tree	Needleleaf tree	C3 grass	C4 grass	Shrub
$d_{r,1}$	root distribution parameter (Oleson et al., 2013)	6.5	7.0	11.0	11.0	7.0
$d_{r,2}$	root distribution parameter (Oleson et al., 2013)	1.5	2.0	2.0	2.0	1.5
$\alpha_{snfree}^{can,vis,dir}$	snowfree visible canopy albedo for direct radiation (Houldcroft et al., 2009)	0.011	0.004	0.038	0.033	0.035
$\alpha_{snfree}^{can,vis,dif}$	snowfree visible canopy albedo for diffuse radiation (Houldcroft et al., 2009)	0.013	0.005	0.043	0.036	0.037
$\alpha_{snfree}^{can,nir,dir}$	snowfree near infrared canopy albedo for direct radiation (Houldcroft et al., 2009)	0.22	0.141	0.269	0.244	0.173
$\alpha_{snfree}^{can,nir,dif}$	snowfree near infrared canopy albedo for diffuse radiation (Houldcroft et al., 2009)	0.256	0.154	0.306	0.275	0.185
$\alpha_{sn}^{can,vis,dir/dif}$	snowfree visible canopy albedo (Moody et al., 2007)	0.44	0.31	0.70	0.70	0.55
$\alpha_{sn}^{can,nir,dir/dif}$	snowfree near infrared canopy albedo (Moody et al., 2007)	0.33	0.24	0.48	0.48	0.37
$T_{cmon}^{min} [^{\circ}C]$	minimum coldest month temperature for establishment (Sitch et al., 2003)	-17.0	-	-	15.5	-
$T_{cmon}^{max} [^{\circ}C]$	maximum coldest month temperature for establishment (Sitch et al., 2003)	-	-2.0	15.5	-	-
$gdd_{min} [^{\circ}C]$	minimum gdd for establishment (Sitch et al., 2003)	1200	350	0	0	0
$T_{cmon}^{phen} [^{\circ}C]$	coldest month temperature for phenology	5.0	-999	0.0	0.0	-999
$T_{base}^{gdd} [^{\circ}C]$	base temperature for gdd (Sitch et al., 2003)	5.0	2.0	2.0	5.0	2.0
$gdd_{crit} [^{\circ}C]$	gdd for full phenology (Sitch et al., 2003)	300	-	100	100	-
$g_{min} [mm s^{-1}]$	minimum canopy conductance (Sitch et al., 2003)	0.5	0.3	0.5	0.5	0.5
$g_1$	parameter in optimal stomatal conductance formulation (Lin et al., 2015)	4.0	2.3	3	1.6	4.0
$L_{ai}^{min} [m^2 m^{-2}]$	minimum leaf area index modified from Clark et al. (2011)	1.0	1.0	0.1	0.1	1.0
$L_{ai}^{max} [m^2 m^{-2}]$	maximum leaf area index modified from Clark et al. (2011)	9.0	7.0	4.0	4.0	3.0
$SLA [m^{-2} kgC^{-1}]$	specific leaf area (Kattge et al., 2011)	12.5	6	20	20	12.5
$\gamma_l [yr^{-1}]$	leaf turnover rate (Kattge et al., 2011)	0.5	0.3	1.0	1.0	0.5
$\gamma_r [yr^{-1}]$	root turnover rate	0.5	0.3	0.5	0.5	0.5
$\gamma_s [yr^{-1}]$	stem turnover rate modified from Clark et al. (2011)	0.005	0.005	0.2	0.2	0.1
$a_{wl} [kgC m^{-2}]$	allometric coefficient (Clark et al., 2011)	0.65	0.75	0.005	0.005	0.1
$a_{ws}$	ratio of total to respiring stem carbon (Cox, 2001)	10	10	1	1	5



**Table 6.** Dynamic vegetation model parameters.

$\nu_{\text{seed}} = 0.001$	vegetation seed fraction
$\gamma_{v,\text{min}} = 0.002 \text{ yr}^{-1}$	minimum vegetation disturbance rate
$\tau_{\text{fire}} = 10 \text{ yr}$	fire return time scale
$\theta_{\text{crit}} = 0.15 \text{ m}^3 \text{ m}^{-3}$	critical soil moisture for fire disturbance
$C_{v,\text{low}} = 0.2 \text{ kgC m}^{-2}$	minimum aboveground vegetation carbon for fire disturbance
$C_{v,\text{high}} = 1.0 \text{ kgC m}^{-2}$	maximum aboveground vegetation carbon for fire disturbance

**Table 7.** Soil carbon model parameters.

$f_{\text{lit}}^{\text{resp}} = 0.7$	fraction of decomposed litter carbon going to atmosphere (Sitch et al., 2003)
$f_{\text{lit} \rightarrow \text{fast}} = 0.985$	fraction of decomposed litter transferred to fast carbon pool (Sitch et al., 2003)
$f_{\text{lit} \rightarrow \text{slow}} = 0.015$	fraction of decomposed litter transferred to slow carbon pool (Sitch et al., 2003)
$D_{\text{bio}} = 1 \times 10^{-4} \text{ m}^2 \text{ year}^{-1}$	bioturbation rate (Braakhekke et al., 2011)
$D_{\text{cryo}} = 5 \times 10^{-4} \text{ m}^2 \text{ year}^{-1}$	cryoturbation rate (Koven et al., 2009, 2013)
$k_{\text{lit},10} = 2.86 \text{ yr}^{-1}$	litter carbon turnover rate at 10 °C (Sitch et al., 2003)
$k_{\text{fast},10} = 33.3 \text{ yr}^{-1}$	fast soil carbon turnover rate at 10 °C (Sitch et al., 2003)
$k_{\text{slow},10} = 1000 \text{ yr}^{-1}$	slow soil carbon turnover rate at 10 °C (Sitch et al., 2003)
$k_{\text{acro},10} = 30 \text{ yr}^{-1}$	acrotelm carbon turnover rate at 10 °C
$k_{\text{cato},10} = 1000 \text{ yr}^{-1}$	catotelm carbon turnover rate at 10 °C (Spahni et al., 2013)
$k_{\text{acro} \rightarrow \text{cato}} = 15 \times 10^{-3} \text{ yr}^{-1}$	catotelm formation rate (Wania et al., 2009; Kleinen et al., 2012)
$f_{\theta,\text{peat}} = 0.3$	soil moisture factor for peat carbon decomposition rate at saturation (Wania et al., 2009)
$\rho_{\text{acro}} = 20 \text{ kgC m}^{-3}$	acrotelm carbon density (Clymo, 1984; R. S. Clymo, 1998)
$\rho_{\text{cato}} = 50 \text{ kgC m}^{-3}$	catotelm carbon density (Turunen et al., 2002; Malmer and Wallén, 2004)
$\rho_{\text{soc,max}} = \rho_{\text{cato}}$	maximum carbon density of soil organic carbon
$C_{\text{acro,crit}} = 5 \text{ kgC m}^{-2}$	minimum acrotelm carbon content for catotelm formation (Wania et al., 2009)
$C_{\text{peat}}^{\text{crit}} = 50 \text{ kgC m}^{-2}$	minimum peat carbon content for peat survival (Stocker et al., 2014)
$\left. \frac{dC_{\text{peat}}}{dt} \right _{\text{crit}} = 10 \text{ kgC m}^{-2} \text{ yr}^{-1}$	minimum peat carbon uptake for peat survival (Stocker et al., 2014)
$f_{\text{CH}_4:\text{C}}^{\text{wet}} = 0.07$	fraction of carbon respired as methane from wetlands ( )
$f_{\text{CH}_4:\text{C}}^{\text{peat}} = 0.2$	fraction of carbon respired as methane from peatlands (Spahni et al., 2013)



**Table 8.** Global values of relevant model quantities over the time period 1981–2010 compared to observation based estimates.

	Model	Observation based estimates
evapotranspiration [ $\times 10^{15}$ kg yr <sup>-1</sup> ]	73	64–73 (Mueller et al., 2013; Trenberth et al., 2007)
runoff [kg yr <sup>-1</sup> ]	35	38–40 (Fekete et al., 2002; Baumgartner and Reichel, 1975)
permafrost area [mln km <sup>2</sup> ]	16.5	13–18 (Gruber, 2012)
GPP [PgC yr <sup>-1</sup> ]	126	115–131 (Beer et al., 2010)
NPP [PgC yr <sup>-1</sup> ]	65	42–70 (Ito, 2011)
vegetation carbon [PgC]	500	470–650 (Prentice et al., 2001)
top meter soil carbon [PgC]	1030	890–1660 (Todd-Brown et al., 2013)
soil carbon in permafrost area [PgC]	590	1100–1500 (Hugelius et al., 2014)
northern peat carbon [PgC]	520	470–620 (Yu et al., 2010)
maximum monthly wetland area [mln km <sup>2</sup> ]	5.7	5 (Prigent et al., 2007; Papa et al., 2010)
northern peatland area [mln km <sup>2</sup> ]	2.9	3.6–4 (Tarnocai et al., 2009; Yu et al., 2010)
total CH <sub>4</sub> emissions [TgCH <sub>4</sub> yr <sup>-1</sup> ]	175	115–215 (Bloom et al., 2010; Bousquet et al., 2006)
tropical CH <sub>4</sub> emissions [TgCH <sub>4</sub> yr <sup>-1</sup> ]	105	63–119 (Bloom et al., 2010; Bousquet et al., 2006)
extratropical CH <sub>4</sub> emissions [TgCH <sub>4</sub> yr <sup>-1</sup> ]	70	39–89 (Bloom et al., 2010; Bousquet et al., 2006)

**Table 9.** Climate forcing fields needed to run PALADYN in offline mode.

Surface air temperature
Surface air specific humidity
Downwelling shortwave radiation at the surface
Downwelling longwave radiation at the surface
Rainfall
Snowfall
Wind speed
Surface pressure